Summer 8-15-2018

Development and Application of Rotation and Curvature Correction to Wray-Agarwal Turbulence Model

Xiao Zhang
Washington University in St. Louis

Recommended Citation

Zhang, Xiao, "Development and Application of Rotation and Curvature Correction to Wray-Agarwal Turbulence Model" (2018). *McKelvey School of Engineering Theses & Dissertations*. 383.
https://openscholarship.wustl.edu/eng_etds/383

WASHINGTON UNIVERSITY IN ST. LOUIS

School of Engineering & Applied Sciences
Department of Mechanical Engineering & Material Science

Dissertation Examination Committee:
Ramesh Agarwal, Chair
Kenneth Jerina
Swami Karunamoorthy
David Peters
Palghat Ramachandran

Development and Application of Rotation and Curvature Correction to Wray-Agarwal Turbulence Model

by
Xiao Zhang

A dissertation presented to
The Graduate School
of Washington University in
partial fulfillment of the
requirements for the degree
of Doctor of Philosophy

August 2018
St. Louis, Missouri

Table of Contents

List of Figures

List of Tables

Nomenclature

C_p = pressure coefficient

C_f = skin friction coefficient

C_w = volume flow rate coefficient

c_{r1}, c_{r2}, c_{r3} = closure coefficients for RC correction

D = diameter

E_R = WA2017m model destruction term

E_{bb} = Baldwin-Barth destruction term

$E_{k\text{-}\omega}$ = old WA2017 model destruction term

ER = expansion ratio

F_{DES} = characteristic length scale ratio of DES model

f_μ = WA2017m model wall-damping function

f_{v1} = SA model wall-damping function

f_1 = blending function of Wray-Agarwal model

f_{r1} = RC correction function

k = turbulent kinetic energy

L_R = turbulent length scale of WA2018-EB model

L_{vk} = von Karman length-scale

l_{DES} = characteristic length scale of DES model

l_{LES} = characteristic length scale of LES model

l_{RANS} = characteristic length scale of RANS model

l_{ref} = reference length scale of WA2018EB model

M = Mach number

n = number of uncertain variables

n_p = oversampling ratio

N_S = UQ sample number

p = order of the response surface polynomial

Q = volume flow rate

R = WA2017m model variable; k/ω

Ri = Richardson number

R_i, R_o = inner and outer radius

Ro = rotation number

S = strain rate magnitude

S_{ij} = strain rate tensor

u_τ = friction velocity

U_{b0} = upstream bulk velocity

U_b = downstream bulk velocity

V_r = radial velocity

V_z = axial velocity

V_θ = tangential velocity

W_{ij} = vorticity tensor

Δ_x = grid spacing along x direction

Δ_y = grid spacing along y direction

Δ_z = grid spacing along z direction

Ω = vorticity magnitude

χ = undamped eddy-viscosity-to-laminar-viscosity ratio

ε = turbulent dissipation

ν_t = turbulent eddy viscosity

ρ = density

τ_w = wall shear stress

ω = specific turbulent dissipation rate

Acknowledgments

I would like to express my sincere gratitude to my academic advisor Dr. Ramesh K. Agarwal for his patient guidance, inspiring encouragement and continuous support. Without his help, my thesis has no chance to be accomplished. Besides the academic area, he is also an excellent mentor in my life. It is my great honor to be under his direction.

I was grateful to receive the efforts and time contributed from my committee members and the staff of the MEMS department during my time at Washington University.

I also want to thank all of my colleagues working in the Computational Fluid Dynamics Laboratory of the Department of Mechanical Engineering & Materials Science at Washington University in St. Louis, for creating a wonderful learning environment.

Last but not the least, I especially want to thank my family for caring and supporting me. They are always there for me no matter what.

The financial support for this work was provided by a MO NASA EPSCoR Grant. It is gratefully acknowledged.

Xiao Zhang

Washington University in St. Louis

August 2018

Dedicated to my grandparents.

Abstract of the Dissertation

Development and Application of Rotation and Curvature Correction to Wray-Agarwal Turbulence Model

by

Xiao Zhang

Doctor of Philosophy in Mechanical Engineering

Washington University in St. Louis, 2018

Research Advisor: Ramesh Agarwal

Computational Fluid Dynamics (CFD) is increasingly playing a significant role in the analysis and design of aircrafts, turbomachines, automobiles, and in many other industrial applications. In majority of the applications, the fluid flow is generally turbulent. The accurate prediction of turbulent flows to date remains a challenging problem in CFD. In almost all industrial applications, Reynolds-Averaged Navier-Stokes (RANS) equations in conjunction with a turbulence model are employed for simulation and prediction of turbulent flows. Currently the one-equation (namely the Spalart-Allmaras (SA) and Wray-Agarwal (WA) and two-equation (namely the k-ε and Shear Stress Transport k-ω) turbulence models remain the most widely used models in industry. However, improvements and new developments are needed to improve the accuracy of the turbulence models for wall bounded flows with separation in the presence of adverse pressure gradients, and for flows with rotation and curvature (RC) such as those encountered in turbomachinery, centrifugal pumps and the rotating machinery in other industrial devices. The goal of this research is to enable the eddy-viscosity type turbulence models to accurately account for the rotation and curvature effects. To date, there have been two approaches for inclusion of RC effects in turbulence models, which can be categorized as the "Modified Coefficients Approach" which parameterizes the model coefficients such that the growth rate of turbulent kinetic energy is either suppressed or enhanced depending upon the effect of system rotation and streamline curvature on the pressure gradient in the flow and the “Bifurcation Approach” which parameterizes the eddy-viscosity coefficient such that the equilibrium solution bifurcates from the main branch to decaying solution branches. In this research, the uncertainty quantification (UQ) is applied to examine the sensitivity of RC correction coefficients and the coefficients are modified based on the UQ analysis to improve the model’s behavior. Both these approaches are applied to the widely used turbulence models (SA, SST k-ω and WA) and they show some improvement in predictions of turbulent flow in all benchmark test cases considered, namely the flow in a 2D curved duct, flow in a 2D U-turn duct, fully developed turbulent flow in a 2D rotating channel, fully developed turbulent flow in a 2D rotating backward-facing step, flow in a rotating cavity, flow in a stationary and rotating serpentine channel, flow in a rotor-stator cavity and in a hydrocyclone as well as two wall-unbounded turbulent flow cases. All the simulations are conducted using the commercial software ANSYS Fluent and the open source CFD software OpenFOAM. The success of this research should enhance the ability of the RANS modeling for more accurate prediction of complex turbulent flows with rotation and curvature effects. In addition to the RANS modeling of RC effects, a new DES model incorporating the WA2017m-RC turbulence model (referred to as the WA2017m-RC-DES model) is developed and validated against experimental and DNS data. Further improvements are obtained with the DES model in some test cases.

Chapter 1: Introduction

1.1 Background

The Reynolds number (Re) is the single most important non-dimensional number in fluid dynamics. It is defined as the dimensionless ratio of the inertial forces to viscous forces. The Re allows us to characterize whether a flow is laminar or turbulent. Laminar flow is characterized by lower Re and higher diffusion over convection. Turbulent flow on the other hand is characterized by higher Re where inertial forces dominate considerably, resulting in largely chaotic flow. The flow may also undergo a transitioning phase whereby the flow exhibits neither completely laminar nor completely turbulent characteristics. The behavior of laminar flow is determined by a single length scale defined by the boundaries of the flow region. If one can accurately describe the boundaries of a laminar flow region, the flow behavior can be calculated precisely using the Navier-Stokes equation. Only for simple geometries and fully developed flows, it is possible to obtain the exact analytical solutions. Although the physics of turbulent flows is governed by the Navier-Stokes and continuity equations, turbulent flow has features that span many length and time scales. At present, even on the most powerful computers, it is difficult to capture all these scales by numerical simulations of governing equations for 3D turbulent flows past complex objects at high Reynolds numbers of industrial significance. Fig. 1.1 shows the transition from laminar to turbulent flow.

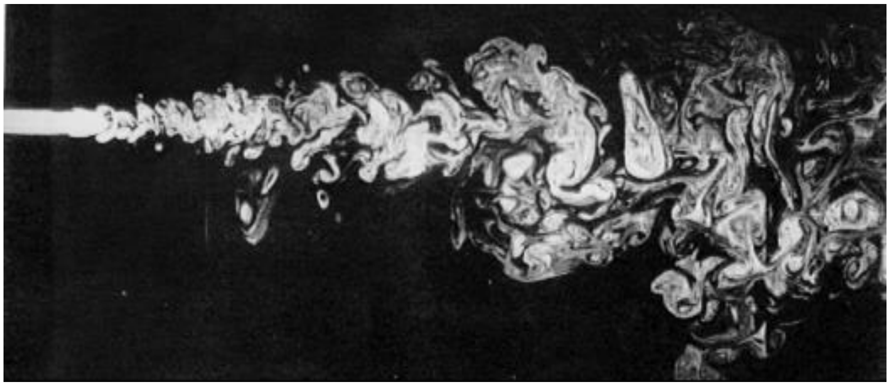

Figure 1.1 Free shear flow illustrating laminar, transition and turbulent phases [1].

1.2 Objectives

The original scalar eddy viscosity turbulence models are not capable of accounting for the system rotation and streamline curvature. One of the goal of this work is to apply the rotation and curvature corrections to the very promising one equation turbulence model based on the k-ω closure, known as the 'Wray-Agarwal (WA)' model. The uncertainty quantification (UQ) is the quantitative characterization and reduction of uncertainty in computational applications via running very large number of calculations to characterize the effects of minor differences in the systems. Another objective in this thesis, is to employ UQ to determine the modification direction of the closure coefficients in the RC correction. The final objective is to develop a new DES model using the WA2017m-RC RANS model with LES. In the literature, DES models have been developed based on the widely used one-equation Spalart-Allmaras (SA) model [2] and the two-equation SST *k-ω* model [3], and they are known to be more accurate than RANS models especially in the presence of flow separation.

1.3 Outline

Chapter 2: Turbulence Modeling: This chapter describes some general topics related to turbulence modeling. Main turbulence modeling methods including Direct Numerical Simulation (DNS), Large-Eddy Simulation (LES) and Reynolds-Averaged Naiver-Stokes (RANS) equations are described. Two widely linear used eddy viscosity turbulence models namely Spalart-Allmaras (SA) and SST *k*-*ω* are briefly introduced.

Chapter 3: Development of Wray-Agarwal (WA) Turbulence Model: This chapter discusses the history and evolution of the one equation Wray-Agarwal (WA) turbulence model. Its development from version WA2017m to WA2018 and finally to WA2018EB is described.

Chapter 4: Rotation and Curvature Correction: This chapter gives a brief introduction to the theory behind the two rotation and curvature correction approaches, the “Modified Coefficients Approach” and the “Bifurcation Approach”.

Chapter 5: Uncertainty Quantification: A brief introduction to uncertainty quantification (UQ) is given and how it is employed to improve the turbulence model coefficients is discussed in this chapter. Closure coefficients of the RC correction are modified based on the UQ analysis.

Chapter 6: Validation Cases: This chapter describes several benchmark test cases in two main categories: wall bounded flows and unbounded flows. The flows in the first category are flow in a 2D curved duct, flow in a 2D U-turn duct, fully developed turbulent flow in a 2D rotating channel, fully developed turbulent flow in a 2D rotating backward-facing step, flow in rotating cavity, flow in a stationary and rotating serpentine channel, flow in a rotor-stator cavity and in a hydrocyclone. The flows in the second category are a subsonic jet and a supersonic jet in cross flow.

Chapter 7: Detached Eddy Simulation (DES): This chapter describes a new DES model named WA2017m-RC-DES. It is validated against experiment and DNS data in some test cases as described in Chapter 6.

Chapter 8: Summary and Future work: This chapter provides a summary of the work accomplished in this thesis, including modeling and testing of the WA2017m-RC, WA2017m-RCM, WA2017m-Arolla, WA2018-RC, WA2018EB-RC and WA2017m-RC-DES models. And some potential future work is also discussed.

Chapter 2: Turbulence Modeling

2.1 Introduction

Direct Numerical Simulation (DNS) solves the full three-dimensional, time-dependent Navier-Stokes equations to obtain instantaneous flow field and then performs averaging to get the statistics. DNS is only feasible for very simple geometries at low Reynolds numbers. Large Eddy Simulation (LES) resolves only the large energy containing scales and models the effects of small scales. LES is possible at relatively higher Reynolds numbers for simple geometries but at a very high computational effort and cost. Reynolds-Averaged Navier-Stokes (RANS) equations are obtained by time-averaging the Navier-Stokes equations over a laboratory time scale which are discussed below.

2.2 Reynolds-Averaged Navier-Stokes Equations

Dating back to early 1900 since Osborne Reynolds, there have been three major approaches that have been developed to model and approximate mathematically the turbulent fluid behavior; these are known as RANS, LES and DNS. The oldest approach developed in early 1900 is based on time-averaging of the Navier-Stokes equations which results in the Reynolds-Averaged Navier-Stokes (RANS) equations. RANS averaging results in the so called “turbulent stresses” or “Reynolds Stresses” which are unknown and require modeling using empiricism. Thus, RANS equations are not closed; it is known as the “Closure Problem” in RANS equations. Closure of RANS equations requires empirical models for “Reynolds Stresses”; these models are called the “RANS Models.” The RANS models are generally developed by using the transport equations for turbulent quantities such as the turbulent kinetic energy, turbulent dissipation, a characteristic turbulent length scale etc. using experimental and other empirical information. The main objective of the turbulence models for the RANS equations is to compute the Reynolds (turbulent) stresses, which are modeled by the scalar eddy-viscosity models of Boussinesq type or directly by the transport equations for various components of Reynolds-stresses. The solutions of RANS equations with turbulence models to date remains the most widely used method in industry for solving the turbulent flows.

2.3 Eddy Viscosity Turbulence Models

In 1877 Boussinesq proposed relating the turbulence stresses to the mean flow to close the system of equations. According to the Boussinesq hypothesis the Reynolds stress terms are modeled as

$$\overline{u_i^{'}\ u_j^{'}} = -2\nu_t S_{ij} + \frac{2}{3}\delta_{ij}k \tag{1}$$

where ν_t is the turbulent kinematic eddy viscosity.

2.3.1 Spalart-Allmaras (SA) Model

The most commonly used one-equation eddy-viscosity turbulence model is the Spalart-Allmaras turbulence model. It was developed by Spalart and Allmaras [4] and was designed specifically for aerospace applications involving wall-bounded flows and has been shown to give good results for boundary layers subjected to adverse pressure gradients. The transport equation for an eddy-viscosity-like variable is given by

$$\frac{\partial\tilde{\nu}}{\partial t} + u_j\frac{\partial\tilde{\nu}}{\partial x_j} = c_{b1}(1-f_{t2})\tilde{S}\tilde{\nu} - \left[c_{w1}f_w - \frac{c_{b1}}{\kappa^2}f_{t2}\right]\left(\frac{\tilde{\nu}}{d}\right)^2 + \frac{1}{\sigma}\left[\frac{\partial}{\partial x_j}\left((\nu+\tilde{\nu})\frac{\partial\tilde{\nu}}{\partial x_j}\right) + c_{b2}\frac{\partial\tilde{\nu}}{\partial x_i}\frac{\partial\tilde{\nu}}{\partial x_i}\right] \tag{2}$$

The turbulent eddy viscosity is computed from

$$\nu_T = f_\mu R \tag{3}$$

The damping function f_{v1} is given by:

$$f_{v1} = \frac{\chi^3}{\chi^3 + \mathrm{c}_{v1}^3}, \qquad \chi = \frac{\tilde{\nu}}{\nu} \tag{4}$$

The additional definitions are given by the following equations:

$$\tilde{S} \equiv \Omega + \frac{\tilde{\nu}}{\kappa^2 d^2} f_{v2} \tag{5}$$

$$f_{v2} = 1 - \frac{\chi}{1 - \chi f_{v1}} \qquad f_w = g\left[\frac{1 + c^6{}_{w3}}{g^6 + c^6{}_{w3}}\right]^{1/6} \tag{6}$$

$$g = r + c_{w2}(r^6 - r) \tag{7}$$

$$r = min\left[\frac{\tilde{\nu}}{\tilde{S}\kappa^2 d^2}, 10\right] \tag{8}$$

$$f_{t2} = c_{t3} exp(-c_{t4}\chi^2) \tag{9}$$

$$\Omega = \sqrt{2W_{ij}W_{ij}} \quad W_{ij} = \frac{1}{2}\left(\frac{\partial u_i}{\partial x_j} - \frac{\partial u_j}{\partial x_i}\right) \tag{10}$$

The constants are

$$c_{b1} = 0.1355 \; \sigma = \frac{2}{3} c_{b2} = 0.622 \; \kappa = 0.41$$

$$c_{w2} = 0.3 \; c_{w3} = 2 \; c_{v1} = 7.1 \; c_{t3} = 1.2 \; c_{t4} = 0.5 \tag{11}$$

$$c_{w1} = \frac{c_{b1}}{\kappa^2} + \frac{1 + c_{b2}}{\sigma}$$

2.3.2 Shear-Stress-Transport *k-ω* Turbulence Model

Menter's Shear Stress Transport (SST) [5] turbulence model is also a widely used robust two-equation eddy-viscosity turbulence model. The model combines the features of *k-ω* turbulence model and *k-ε* turbulence model such that the *k-ω* model is used in the inner region of the boundary layer and switches to the *k-ε* model in the free shear flow region. The formulation of the SST model is based on information from many experiments and attempts to predict solutions to typical engineering problems. The two-equation model is given by the following equations:

$$\frac{\partial(\rho k)}{\partial t}+\frac{\partial(\rho u_i k)}{\partial x_j}=P-\beta^*\rho\omega k+\frac{\partial}{\partial x_j}\left[(\mu+\sigma_k\mu_t)\frac{\partial k}{\partial x_j}\right] \tag{12}$$

$$\frac{\partial(\rho\omega)}{\partial t}+\frac{\partial(\rho u_i\omega)}{\partial x_j}=\frac{\gamma}{\nu_t}P-\beta\rho\omega^2+\frac{\partial}{\partial x_j}\left[(\mu+\sigma_\omega\mu_t)\frac{\partial\omega}{\partial x_j}\right]+2(1-F_1)\frac{\rho\sigma_{\omega 2}}{\omega}\frac{\partial k}{\partial x_j}\frac{\partial\omega}{\partial x_j} \tag{13}$$

$$P=\tau_{ij}\frac{\partial u_i}{\partial x_j} \tag{14}$$

The turbulence eddy viscosity is computed from:

$$\nu_t=\frac{\rho a_1 k}{max(a_1\omega,\Omega F_2)} \tag{15}$$

Each of the constants is a blend of an inner (subscript 1) and outer (subscript 2) constant via

$$\phi=F_1\phi_1+(1-F_1)\phi_2 \tag{16}$$

Additional functions are defined as

$$F_1=tanh(arg_1^4) \tag{17}$$

$$arg_1=min\left[\max\left(\frac{\sqrt{k}}{\beta^*\omega d},\frac{500\nu}{d^2\omega}\right),\frac{4\rho\sigma_{\omega 2}k}{CD_{k\omega}d^2}\right] \tag{18}$$

$$CD_k=\max\left(2\rho\sigma_{\omega 2}\frac{1}{\omega}\frac{\partial k}{\partial x_j}\frac{\partial\omega}{\partial x_j},10^{-20}\right) \tag{19}$$

$$F_2=tanh(arg_2^2) \tag{20}$$

$$arg_2=\max\left(2\frac{\sqrt{k}}{\beta^*\omega d},\frac{500\nu}{d^2\omega}\right) \tag{21}$$

The constants are

$$\begin{gathered}\gamma_1=\frac{\beta_1}{\beta^*}-\frac{\sigma_{\omega 1}\kappa^2}{\sqrt{\beta^*}}\ \gamma_2=\frac{\beta_2}{\beta^*}-\frac{\sigma_{\omega 2}\kappa^2}{\sqrt{\beta^*}}\\ \sigma_{k1}=0.85\ \sigma_{\omega 1}=0.5\ \beta_1=0.075\\ \sigma_{k2}=1.0\ \sigma_{\omega 2}=0.856\ \beta_2=0.0828\ \beta^*=0.09\ \kappa=0.41\ a_1=0.31\end{gathered} \tag{22}$$

Chapter 3: Development History of Wray-Agarwal (WA) Turbulence Model

3.1 WA2017m

Wray-Agarwal (WA) model is a newly developed one-equation eddy-viscosity turbulence model derived from k-ω closure. In this model, a new variable R is introduced which is defined as k/ω. It has been applied to several canonical flows [6] and has shown improved accuracy over the SA model and competitiveness with the SST k-ω model. An important distinction between the WA model and previous one-equation models based on two equation k-ω models is the inclusion of the cross diffusion term in the ω-equation and a blending function which allows smooth switching between two destruction terms. The equations of the WA2017 turbulence model are given below.

$$\frac{\partial R}{\partial t} + u_j \frac{\partial R}{\partial x_j} = \frac{\partial}{\partial x_j}\left[(\sigma_R R + \nu)\frac{\partial R}{\partial x_j}\right] + C_1 RS + f_1 C_{2k\omega}\frac{R}{S}\frac{\partial R}{\partial x_j}\frac{\partial S}{\partial x_j} - (1 - f_1)C_{2k\varepsilon}R^2\left(\frac{\frac{\partial S}{\partial x_j}\frac{\partial S}{\partial x_j}}{S^2}\right) \tag{23}$$

$$f_1 = \min(tanh(arg_1^4), 0.9) \tag{24}$$

$$arg_1 = \frac{1 + 20\eta}{1 + \left(\frac{d\max\left(\sqrt{RS}, 1.5R\right)}{20\nu}\right)^2} \tag{25}$$

$$\eta = \frac{d\sqrt{RS}}{20\nu} \tag{26}$$

The eddy viscosity is calculated through the new variable R

$$\nu_t = f_\mu R \tag{27}$$

Again, to account for the wall blocking effect, the damping function f_μ is defined in the same form as in the SA model.

$$f_\mu = \frac{\chi^3}{\chi^3 + C_w^3}, \qquad \chi = \frac{R}{\nu} \tag{28}$$

While the $C_{2k\omega}$ term is active, Eq. (25) behaves as a one equation model based on the standard *k*-*ω* equations. The inclusion of the cross diffusion term in the derivation causes the additional $C_{2k\varepsilon}$ term to appear. This term corresponds to the destruction term of one equation models derived from standard *k*-*ε* closure. The presence of both terms allows the new model to behave either as a one equation *k*-*ω* or one equation *k*-*ε* model based on the switching function f_1. Being a one equation model, it is more computationally efficient than the multi-equation models. Even though the WA model appears promising, it also has limitations in accuracy for computing wall bounded separated flows.

The last term in Eq. (25) involves the inverse of the von Karman length-scale:

$$E_{k-\omega} = R^2 \left(\frac{1}{L_{VK}}\right) = R^2 \left(\frac{\frac{\partial S}{\partial x_j}\frac{\partial S}{\partial x_j}}{S^2}\right) \tag{29}$$

As has been pointed out previously in Ref. [7], $E_{k-\omega}$ can become singular whenever S goes to zero leading to an infinite destruction term. In order to prevent this from happening, the last destruction term is limited by a multiple of the Baldwin-Barth destruction term, E_{bb}:

$$E_R = C_m E_{bb} \tanh\left(\frac{E_{k-\omega}}{C_m E_{bb}}\right) \tag{30}$$

with a constant $C_m = 8.0$. E_{bb} is defined as:

$$E_{bb} = \frac{\partial R}{\partial x_j}\frac{\partial R}{\partial x_j} \tag{31}$$

Eq. (30) provides a smooth transition between the two formulations whenever $E_{k-\omega}$ goes to infinity. For majority of the flow region, $E_{k-\omega} \ll C_m E_{bb}$ and the original formulation is recovered. A less smooth transition could be achieved by $E_R = \min(E_{k-\omega}, C_m E_{bb})$. For all the test cases considered in this paper, these two methods for $E_{k-\omega}$ yield almost the same results. The constant C_m is calibrated by computing flow past a zero pressure gradient the flat plate and in a channel flow. There is major difference between the new WA2017m and the old WA2017 model. The final formulation of the WA2017m model becomes [8]:

$$\frac{\partial R}{\partial t} + u_j \frac{\partial R}{\partial x_j} = \frac{\partial}{\partial x_j}\left[(\sigma_R R + \nu)\frac{\partial R}{\partial x_j}\right] + C_1 RS + f_1 C_{2k\omega}\frac{R}{S}\frac{\partial R}{\partial x_j}\frac{\partial S}{\partial x_j} - (1 - f_1)C_{2k\varepsilon}E_R \tag{32}$$

$$E_R = C_m E_{bb} \tanh\left(\frac{E_{k-\omega}}{C_m E_{bb}}\right) \quad \text{or } \min\,(E_{k-\omega}, C_m E_{bb}) \tag{33}$$

The model constants are as follows:

$$\begin{gathered}
C_{1k\omega} = 0.0829 \quad C_{1k\varepsilon} = 0.1127 \\
C_1 = f_1(C_{1k\omega} - C_{1k\varepsilon}) + C_{1k\varepsilon} \\
\sigma_{k\omega} = 0.72 \quad \sigma_{k\varepsilon} = 1.0 \\
\sigma_R = f_1(\sigma_{k\omega} - \sigma_{k\varepsilon}) + \sigma_{k\varepsilon} \\
\kappa = 0.41 \\
C_{2k\omega} = \frac{C_{1k\omega}}{\kappa^2} + \sigma_{k\omega} \quad C_{2k\varepsilon} = \frac{C_{1k\varepsilon}}{\kappa^2} + \sigma_{k\varepsilon} \\
C_w = 8.54
\end{gathered} \tag{34}$$

3.2 Wall Distance Free WA2018 Model

In order to improve the generality and efficiency of the WA model, new formulation avoiding the use of wall–distance *d* is devised. Since the transport equation does not contain explicitly the distance to the wall *d*, it can be replaced without any rigorous modifications to the model equation. There is wall distance *d* in Eq. (25) which can create inaccuracies in flow past complex curved surfaces and moving boundaries. Therefore, a wall-distance free formulation WA model is developed and is designated as WA2018 which is described below. The transport equation of WA2018 is the same as WA2017m given in Eq. (32). The newly designed wall distance free blending function is

$$f_1 = tanh(arg_1^4) \tag{35}$$

$$arg_1 = \frac{\nu + R}{2}\frac{\eta^2}{C_\mu k\omega}$$

$$k = \frac{\nu_T S}{\sqrt{C_\mu}}, \omega = \frac{S}{\sqrt{C_\mu}}, \eta = S \max\left(1, \left|\frac{W}{S}\right|\right) \tag{36}$$

$$W = \sqrt{2W_{ij}W_{ij}}, W_{ij} = \frac{1}{2}\left(\frac{\partial u_i}{\partial x_j} - \frac{\partial u_j}{\partial x_i}\right)$$

Most of the coefficients and constants are the same as in WA2017m given in Eq. (34); the only constant changed is $C_{1k\varepsilon}$.

$$C_{1k\varepsilon} = 0.1284 \tag{37}$$

The WA2018 model was extensively validated by computing a number of benchmark flows listed on NASA TMR website [10]. Although WA2018 gives excellent results in a large number of benchmark test cases, it cannot compute accurately the log layer in the turbulent boundary layer compared to DNS data. This problem is addressed by including the elliptic blending/elliptic relaxation in the model as described in the next section.

3.3 WA2018EB Model

It has been shown by several investigators [11-14] that by including an elliptic relaxation model with a turbulence model, the anisotropic low Reynolds number near wall effects can be more accurately captured. The model equation for elliptic blending is generally expressed as

$$-{L_R}^2\nabla^2 P_R + P_R = -C_{3k\omega}R\frac{\partial^2 R}{\partial {x_j}^2} + RS \tag{38}$$

where P_R is a production term which couples Eq. (38) and a modified model Eq. (39) given below. In Eq. (38), the diffusion/destruction term $C_{3k\omega}R\frac{\partial^2 R}{\partial {x_j}^2}$ can be neglected in most cases without affecting the accuracy. The coupled WA model equations with elliptic blending take the form

$$\begin{gathered}\frac{\partial R}{\partial t} + u_j\frac{\partial R}{\partial x_j} = \frac{\partial}{\partial x_j}\left[(\sigma_R R + \nu)\frac{\partial R}{\partial x_j}\right] + RS(C_1 - 1) + P_R + f_1 C_{2k\omega}\frac{R}{S}\frac{\partial R}{\partial x_j}\frac{\partial S}{\partial x_j} - (1 - f_1)C_{2k\varepsilon}E_R \\ -{L_R}^2\nabla^2 P_R + P_R = RS\end{gathered} \tag{39}$$

It should be noted that the near-wall turbulence eddies follow the Kolmogorov scaling (i.e. the turbulence fluctuations depend on the laminar viscosity). Therefore, ν/S can be used for the viscous scaling serving as a lower bound on the turbulent length scale L_R. In Eq. (40), L_{ref} is the reference length scale.

$${L_R}^2 = \frac{\max(C_{3k\omega}R, C_l\nu)}{S + \frac{C_l\nu}{{L_{ref}}^2}} \tag{40}$$

The WA model given by Eq. (39) and Eq. (40) is designated as WA2018EB [9]. It is a wall distance free model; therefore f_1 function in this model is the same as that given in Eqs. (37) and (38). The values of the changed and new constants in WA2018EB model are listed below. It should be noted that some of these constants are different from Eq. (34) and Eq. (37), and there are two additional constants given in Eq. (41).

$$\begin{gathered} C_{1k\omega} = 0.2 \quad C_{1k\varepsilon} = 0.094 \\ C_{2k\omega} = 2.63 \quad C_{2k\varepsilon} = 1.24 \\ C_w = 5.97 \\ C_l = 4.0 + \sqrt{\chi} \\ C_{3k\omega} = 0.17 \end{gathered} \tag{41}$$

Chapter 4: Introduction to Rotation and Curvature Correction

4.1 Background

In many industrial applications, rotation and curvature effects are very important. For example, in a gas turbine engine, cool air taken form the middle stages of the compressor is circulated through the internal cooling passages inside the turbine blades to reduce temperature levels below the melting point of the blade material. These passages often have strongly curved surface where both rotation and curvature play an important role in prediction of the heat transfer. Similarly, in a circulation control airfoil, streamline curvature effects need to be considered to accurately calculate the lift coefficient. Some other applications include particle separation in a hydrocyclone, vortex evolution in tip clearance flow in a centrifugal pump etc.

RANS equations with scalar turbulence closure models are still the workhorse in the industrial design process and will remain so far at least next few decades. However, these closure models do not respond well to the imposed system rotation and streamline curvature. The modifications to the scalar eddy viscosity models to include the effects of rotation and curvature (RC) are called the rotation and curvature corrections, which can be categorized into two approaches, namely the "Modified Coefficient Approach" and the "Bifurcation Approach". A review of the methodology used in these approaches can be found in Durbin [15]. The modified coefficients approach dates back to 1980s. In 1997, Spalart and Shur [16] introduced a correction to the production term in a transport equation for eddy viscosity. They proposed a unified measure for rotation and curvature in terms of the material derivative of the strain rate tensor, making the model frame independent and Galilean invariant. In 2000, a more detailed assessment of Spalart-Shur correction approach was given by Shur et al. [17]. In 1999, Reif and Durbin [18] proposed a novel approach for including the rotational effects in scalar turbulence models. Bifurcation analysis of Second-Moment Closure (SMC) in rotating homogeneous shear flow forms the basis for this work. This model is formulated such that the equilibrium solution bifurcates from the main to the decaying solution branches. In 2013, Arolla [19] proposed a new and simpler form based on the work of Reif and Durbin [18].

4.2 Effect of Rotation and Curvature

First, we consider the effect of streamline curvature. The way to include the effect of streamline curvature in the turbulent flow is to alter the turbulent intensity. More specifically, the convex curvature reduces turbulent intensity while the concave curvature enhances turbulent intensity. The term “convex” refers to a boundary layer along a wall with the center of curvature inside the surface; e.g., the outside surface of a circular arc. The boundary layer velocity profile is such that it increases radially outward from the center of curvature. On the other hand the “concave” wall curves opposite to the center of curvature outside the surface; e.g., the inside surface of a bowl, and the boundary layer velocity increases towards the center of curvature. A sketch of both convex and concave walls are shown in Fig. 4.1. To characterize the effect of curvature on a shear flow, two types of rotations are considered. The first one is such that, as the flow passes over a curved wall, the direction of the velocity vector rotates. The second one is such that, the fluid elements within a shear flow also rotate: they rotate clockwise if $dU/dy > 0$. The streamline curvature effect on turbulence is determined by these two types of rotation: along a convex wall, the velocity vector rotates in the same direction as fluid elements; along a concave wall the rotations are in opposite directions. Co-rotation suppresses turbulence, and counter-rotation enhances it. Another way to analyze this problem is to compare it with flat plate, the flow over a convex wall can be regarded as “expanded” while over a concave wall as “shrunk”. The result of “expanded” and “shrunk” flow is the turbulent intensity being reduced and enhanced, respectively.

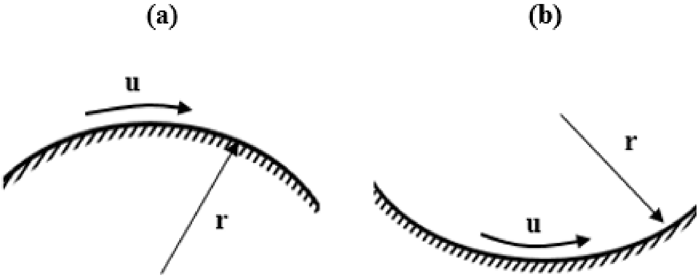

Figure 4.1 Sketch of (a) convex and (b) concave wall.

Secondly, we examine the effect of reference frame rotation. An analogy exists between system rotation and streamline curvature. If the frame rotation is in the same direction as the shear, turbulent intensity is reduced by rotation; if they are opposite turbulent intensity increases. Let us consider a flow configuration that a planar rotating channel with span-wise rotation shown in the Fig. 4.2. The direction of shear next to wall is opposite to each other; so the rotation will enhance the turbulence next to one wall and reduce it next to the other. Here, with a counter-clock wise rotation, the upper wall is on the suction side and the turbulence intensity is reduced on this side; it is categorized as stable side. On the other hand, the lower wall is on the pressure side and the turbulence intensity is enhanced; it is known as the unstable side. More fundamentally, the shear next to the upper wall rotates fluid elements in the counter-clock direction which is in the same direction as the frame rotation; while they are opposite on the lower wall. The surface shear stress increases on the unstable side; the shear stress decreases on the stable side.

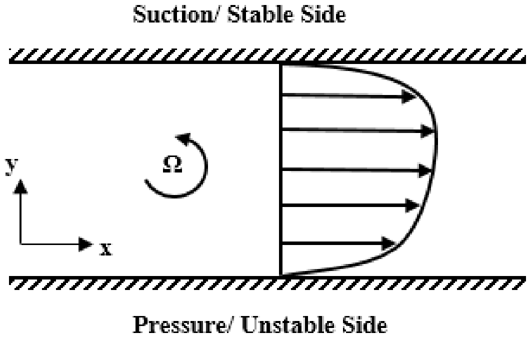

Figure 4.2 Flow in a planar rotating channel.

This effect cannot be captured by standard scalar eddy viscosity models: they are insensitive to rotation and predict the flow profiles that maintain symmetry about the channel centerline. In the following section, we discuss the inherent limitation of scalar eddy viscosity models that cause this problem.

4.3 Equilibria of the *k* and *ε* Equations

Equilibrium analysis provides insights into the properties of closure schemes, for example it shows how the model responds to imposed forcing. It is also the basis for a systematic derivation of nonlinear, algebraic constitutive formulas. The reason of choosing *k*-*ε* model is that the two transport variables — the turbulent kinetic energy *k* and turbulent dissipation *ε* directly reflect the turbulence level in the flow field. The transport equations for *k* and *ε* can be written as:

$$\frac{\partial k}{\partial t}+\frac{\partial\left(u_j k\right)}{\partial x_j}=\frac{\partial}{\partial x_j}\left[\frac{\nu_t}{\sigma_k}\frac{\partial k}{\partial x_j}\right]+2\nu_t S_{ij}S_{ij}-\varepsilon \tag{42}$$

$$\frac{\partial \varepsilon}{\partial t}+\frac{\partial\left(u_j \varepsilon\right)}{\partial x_j}=\frac{\partial}{\partial x_j}\left[\frac{\nu_t}{\sigma_\varepsilon}\frac{\partial \varepsilon}{\partial x_j}\right]+C_{1\varepsilon}\frac{\varepsilon}{k}2\nu_t S_{ij}S_{ij}-C_{2\varepsilon}\frac{\varepsilon^2}{k} \tag{43}$$

Consider the *k* – *ε* model in incompressible homogenous turbulent flow; the governing equations can be simplified to:

$$\frac{\partial k}{\partial t} = P - \varepsilon \tag{44}$$

$$\frac{\partial \epsilon}{\partial t} = \frac{C_{1\varepsilon}P - C_{2\varepsilon}\varepsilon}{T} \tag{45}$$

where $T = k/\varepsilon$ is the turbulent time-scale and $P = -\overline{u_i^{'}\ u_j^{'}}\ S_{ij}$ is the rate of energy production. Following Durbin [15], Eq. (44) and Eq. (45) can be combined into

$$\frac{\partial}{\partial t}\left(\frac{\varepsilon}{k}\right) = \left(\frac{\varepsilon}{k}\right)^2 \left[(C_{1\varepsilon} - 1)\frac{P}{\varepsilon} - (C_{2\varepsilon} - 1)\right] \tag{46}$$

Equation (44) is the evolution equation for the scalar (ε/k) and it has two equilibria ($t \to \infty$), obtained by setting $\frac{\partial}{\partial t}\left(\frac{\varepsilon}{k}\right) = 0$ on the left hand side, which are

$$\text{branch 1:}\quad \frac{P}{\varepsilon} = \frac{C_{2\varepsilon} - 1}{C_{1\varepsilon} - 1} \tag{47}$$

and

$$\text{branch 2:}\quad \frac{\varepsilon}{k} = 0 \tag{48}$$

Using the standard values of constant coefficients $C_{1\varepsilon}$ = 1.44 and $C_{2\varepsilon}$ = 1.92, P/ε is equal to 2.09 on branch 1. As for other version of $k - \varepsilon$ model (e.g. Chien [20]), the constant coefficients $C_{1\varepsilon}$ and $C_{2\varepsilon}$ are set to be 1.35 and 1.80 giving P/ε equals to 2.29. In general, $P/\varepsilon > 1$ and k grows with time according to Eq. (44). The equilibria is divided into two solutions, “healthy” (Eq. (47)) and “decaying” (Eq. (48)). On the healthy branch (Eq. (47)) turbulent energy grows exponentially in time. For the branch 1, we can re-write Eq. (44) and (45) as

$$\frac{\partial k}{\partial t} = (\alpha - 1)\varepsilon \tag{49}$$

$$\frac{\partial \varepsilon}{\partial t} = (\alpha - 1)\frac{\varepsilon^2}{k} \tag{50}$$

where $\alpha = P/\varepsilon = (C_{2\varepsilon} - 1)/(C_{1\varepsilon} - 1)$. Thus, the solutions of Eq. (49) and Eq. (50) have the form [15]:

$$\text{branch 1:}\ \ k = k_\infty e^{\lambda t},\ \ \varepsilon = \varepsilon_\infty e^{\lambda t} \tag{51}$$

The subscript ∞ represents the equilibrium value ($t \rightarrow \infty$), depending on the initial conditions. Substituting these solutions (Eq. (51)) into Eq. (49) or Eq. (50) gives

$$\lambda = (\alpha - 1)\left(\frac{\varepsilon}{k}\right)_\infty = \frac{C_{2\varepsilon} - C_{1\varepsilon}}{C_{1\varepsilon} - 1}\left(\frac{\varepsilon}{k}\right)_\infty \tag{52}$$

All the linear eddy viscosity turbulence models are based on Boussinesq assumption. Thus, the linear constitutive relationship Eq. (53) can be used.

$$\overline{u_i^{'}\ u_j^{'}} = -2\nu_t S_{ij} + \frac{2}{3}\delta_{ij} k \tag{53}$$

With Eq. (53), the rate of energy production becomes

$$P = 2\nu_t |S|^2 \tag{54}$$

where $|S|$ is the magnitude of the strain rate. The eddy viscosity for k – ε model is $\nu_t = C_\mu k^2/\varepsilon$, thus

$$\frac{P}{\varepsilon} = 2C_\mu |S|^2 \left(\frac{k}{\varepsilon}\right)^2 \tag{55}$$

Substituting it into Eq. (47) yields the equilibrium value

$$\left(\frac{\varepsilon}{k|S|}\right)_{\infty} = \sqrt{2C_{\mu}}\sqrt{\frac{C_{1\varepsilon}-1}{C_{2\varepsilon}-1}} \tag{56}$$

Then the exponential growth rate λ in Eq. (52) becomes

$$\lambda = \frac{C_{2\varepsilon}-C_{1\varepsilon}}{\sqrt{(C_{1\varepsilon}-1)(C_{2\varepsilon}-1)}}\sqrt{2C_{\mu}|S|^{2}} \tag{57}$$

It is always positive by applying the standard coefficient constants, which matches with the observation for the healthy branch. For the second branch, the solution has the power law form [15]:

$$\text{branch 2:}\;\; k = A_{\infty}t^{m}, \quad \epsilon = B_{\infty}t^{m-1} \tag{58}$$

In this case, $\varepsilon/k \propto 1/t \to 0$ as $t \to \infty$. Again substituting these solutions into Eq. (44) and Eq. (45) gives

$$\frac{\partial k}{\partial t} = P - \epsilon = A_{\infty}mt^{m-1} \tag{59}$$

$$\frac{\partial \varepsilon}{\partial t} = \frac{C_{1\varepsilon}P - C_{2\varepsilon}\varepsilon}{T} = B_{\infty}(m-1)t^{m-2} \tag{60}$$

where $T = k/\varepsilon = (A_{\infty}/B_{\infty})t$. Solving for *m*, we obtain:

$$m = \frac{\frac{P}{\varepsilon}-1}{(C_{2\varepsilon}-1)-\frac{P}{\varepsilon}(C_{1\varepsilon}-1)} \tag{61}$$

If $P/\varepsilon < 1$, the exponent *m* has negative value and turbulent energy decays, which is also indicated in Eq. (44). After examining the two branches of solutions, it can be concluded that within the scalar eddy viscosity assumption, the rotation is not able to stabilize or destabilize the solution since the rotation does not appear in the equations of the *k*-*ε* model. In the next two sections, we introduce two approaches, "Modified Coefficients Approach" and "Bifurcation Approach" that are designed to overcome this deficiency.

4.4 Modified Coefficients Approach

It has been proposed in the literature that the coefficients of the *k*-*ε* model should be given a parametric dependence on the rotation number

$$Ro \equiv -2\Omega^F/(\partial \mathrm{U}/\, \partial \mathrm{y}) \tag{62}$$

so that the turbulent kinetic energy decays in the stabilization region and grows in the destabilization region. According to Eq. (52), the exponential growth rate λ is a function of $C_{1\varepsilon}$ and $C_{2\varepsilon}$ which are constants in the standard *k*-*ε* model. The basic idea of "Modified Coefficients Approach" is to make either $C_{1\varepsilon}$ or $C_{2\varepsilon}$ or both functions of rotation and strain rate so that growth rate λ becomes negative in stable regions.

An early proposal to model rotational stabilization was [21]

$$C_{2\varepsilon} = C_{2\varepsilon}^{0}(1 - C_{sc}Br) \tag{63}$$

The Bradshaw number *Br* is defined as:

$$Br \equiv Ro(Ro + 1) \tag{64}$$

The critical Bradshaw number Br_{crit} is defined when $P/\epsilon = 1$, which is found from $C_{1\varepsilon} = C_{2\varepsilon}$, according to Eq. (47).

$$C_{1\varepsilon} = C_{2\varepsilon} = C_{2\varepsilon}^{0}(1 - C_{sc}Br_{\text{crit}})$$

$$Br_{\text{crit}} = \frac{C_{2\varepsilon}^{0} - C_{1\varepsilon}}{C_{2\varepsilon}^{0}C_{sc}} \tag{65}$$

If $Br > Br_{\text{crit}}$, which corresponds to $C_{1\varepsilon} > C_{2\varepsilon}$ from Eq. (52), the exponential growth rate λ becomes negative. With the standard k-ε model coefficients $C_{1\varepsilon} = 1.44$, $C_{2\varepsilon}^{0} = 1.92$ and $C_{sc} = 2.5$, Br_{crit} is equal to 0.1; substituting into Eq. (64) we obtain $Ro > 0.0916$ or $Ro < -1.091$. This is the range in which the rotation stabilizes turbulence.

Another example of the “Modified Coefficients Approach” is the work by Spalart and Shur [16]. Before their work, proposals were made based on the streamline curvature, but streamlines are not Galilean invariant, since they are referred to axes aligned with the velocity. For this reason, efforts to literally represent streamline curvature have been replaced by a method that unifies rotation and curvature via the rate of rotation of the principal axes of the strain rate tensor (Spalart and Shur [16]).

The strain rate tensor is symmetric, so it can be expressed as [15]

$$\mathbf{S} = \sum_{\alpha=1}^{3} \lambda_{\alpha}\, \mathbf{e}^{\alpha}\mathbf{e}^{\alpha} \tag{66}$$

where the $\boldsymbol{e}$’s are unit eigenvectors and λ’s are eigenvalues. Unit vectors can only be changed by rotation.

$$\frac{D\mathbf{e}^{\alpha}}{Dt} = \boldsymbol{\Omega}^{S}_{\alpha\beta}\mathbf{e}^{\beta} \tag{67}$$

The rotation rate tensor $\boldsymbol{\Omega}^{S}_{\alpha\beta}$ can be computed from the mean velocity field. During a computation, the eigenvector of the strain rate tensor must be evaluated at each time step and at every grid point. Then their substantial derivative (*D/Dt*) can be computed. This process usually takes high computational cost. On the grounds of computational efficiency, Spalart and Shur [16] proposed to replace the eigenvector by the full rate of strain tensor and introduced the Spalart-Shur tensor:

$$\mathbf{W}^{\mathrm{ss}} \equiv \frac{\mathbf{S}\cdot(D\mathbf{S}/Dt) - (D\mathbf{S}/Dt)\cdot\mathbf{S}}{2|\mathbf{S}|^{2}} \tag{68}$$

Wallin and Johansson [22] derived the connection of the Spalart-Shur tensor to rotation of the principal axes in three dimensions. If rotation vectors are introduced via $\omega^{\mathrm{SS}}_{i} = \frac{1}{2}\varepsilon_{ijk}W^{\mathrm{SS}}_{jk}$ for the Spalart-Shur tensor and $\Omega^{\mathrm{S}}_{ij} = \varepsilon_{ijk}\omega^{\mathrm{S}}_{k}$ for the rotation of eigenvector, then the exact relation between the Spalart-Shur tensor and the rotation rate of the principal axes is

$$\omega^{\mathrm{SS}}_{i} = \omega^{\mathrm{S}}_{i} - \frac{3S^{2}_{ij}}{2|\mathbf{S}|^{2}}\omega^{\mathrm{S}}_{j} \tag{69}$$

Notice that, in two dimensions, ω^{S} is in the x_3 direction, so that $\boldsymbol{\Omega}^{\mathrm{S}} = \mathbf{W}^{\mathrm{ss}}$. This surrogate for curvature and rotation represents a unification of rotation and curvature, because in a rotating reference frame, $\boldsymbol{\Omega}^{\mathrm{S}}$ includes the system rotation tensor. In this way, any model that was designed for system rotation is devised into a model for both rotation and streamline curvature by replacing coordinate frame rotation $\boldsymbol{\Omega}^{\mathrm{F}}$ by rotation of the principal axes of the strain rate $\boldsymbol{\Omega}^{\mathrm{S}}$ [23].

For example, the absolute rotation tensor is defined as

$$\mathbf{\Omega}^{\mathrm{A}} = \mathbf{\Omega} + \mathbf{\Omega}^{\mathrm{F}} \tag{70}$$

where $\mathbf{\Omega}$ is the vorticity tensor relative to a rotating frame. Alternatively, the $\mathbf{\Omega}^{\mathrm{A}}$ is redefined as

$$\mathbf{\Omega}^{\mathrm{A}} = \mathbf{\Omega} + \mathbf{\Omega}^{\mathrm{S}} \tag{71}$$

Another example is from Reynolds stress models, the frame rotation enters via

$$\mathbf{\Omega}^{*} = \mathbf{\Omega} + C_r \mathbf{\Omega}^{\mathrm{F}} \tag{72}$$

where C_r is a model coefficient constant [22, 24]. Again, the unification of rotation and curvature is invoked by supplanting $\mathbf{\Omega}^{\mathrm{F}}$ with $\mathbf{\Omega}^{\mathrm{S}}$ to obtain

$$\mathbf{\Omega}^{*} = \mathbf{\Omega} + C_r \mathbf{\Omega}^{\mathrm{S}} \tag{73}$$

The Spalart-Shur rotation and curvature correction [16] was based on the Spalart-Shur tensor (Eq. (68)), and they devised a function of the parameter

$$\tilde{r} = \frac{|\mathbf{S}|^2 \mathbf{\Omega} : \mathbf{W}^{ss}}{(|\mathbf{S}|^2 + |\mathbf{\Omega}|^2)^2} \tag{74}$$

This ad hoc function was added into an eddy viscosity transport equation in order to enhance or reduce production, depending on the sign of this inner product. In homogeneous turbulence the transport equation contains only a production term, so this approach is inescapable. It is like altering the growth exponent λ. More details of the Spalart-Shur rotation and curvature correction are given in the section 4.6.

4.5 Bifurcation Approach

The idea behind the "Modified Coefficients Approach" is to parameterize the coefficient $C_{2\varepsilon}$ in the Bradshaw number *Br* so that the rotation increases the kinetic energy and dissipation rate for $P/\varepsilon > 1$. But in general, $C_{2\epsilon}$ remains a constant value. The equilibrium analysis of the second moment closure models shows that there are two types of equilibrium solutions (Speziale and M. G. Mhuiris [25]): one is $(\varepsilon/Sk)_\infty$ = 0 which exists for all dimensionless parameter Ω/S and another is $(\varepsilon/Sk)_\infty$ > 0 which exists only for a small intermediate range of Ω/S. The zero equilibrium solution is associated predominantly with stable flow wherein k and ε undergo a power law time decay; the nonzero equilibrium solution is associated with unstable flow wherein k and ε undergo an exponential time growth. In this fashion, the second order closure models are able to account for both the shear instability – with its exponential time growth of disturbance kinetic energy – and the stabilizing (or destabilizing) effect of rotations on shear flow [26]. In other words, the branch 1 (Eq. (47)) ceases to exist and switches to branch 2 (Eq. (48)) when rotation rate is above one limit, or below another, which corresponds approximately to Ro > 0 or Ro < -1. The term "bifurcation" is used to describe this behavior; "Bifurcation Approach" is to introduce this characteristic behavior into scalar eddy-viscosity models by making C_μ depend on the rate of strain and rotation [18]. In particular, let

$$S_{ij} = \frac{1}{2}\left(\frac{\partial u_i}{\partial x_j} + \frac{\partial u_j}{\partial x_i}\right)$$

$$\Omega_{ij}^{*} = \Omega_{ij}^{\mathrm{rel}} + C_r \varepsilon_{ijk} \omega_k^{\mathrm{F}} = \Omega_{ij}^{\mathrm{rel}} + C_r \Omega_{ij}^{\mathrm{F}} \tag{75}$$

C_r depends on the constants of the closure model. In the SSG pressure-strain model by Spezial and Gtaski [26], C_r = 2.25 is adopted. The dimensionless parameters are defined as:

$$\eta_1 = S_{ij} S_{ij} (k/\varepsilon)^2 = |\mathbf{S}k/\varepsilon|^2 \tag{76}$$

$$\eta_2 = \Omega^*_{ij}\Omega^*_{ij}(k/\varepsilon)^2 = |\mathbf{\Omega}^* k/\varepsilon|^2$$

Eq. (55) becomes

$$\frac{P}{\varepsilon} = 2C_\mu \eta_1 \tag{77}$$

The eddy viscosity formula can be made of a function of η_1 and η_2/η_1, such that $C_\mu = F_\mu(\eta_1, \eta_2/\eta_1)$. The argument η_2/η_1 (= Ω/S) is a generalization of the rotation parameter. Then on branch 1, the Eq. (47) becomes

$$\frac{C_{2\varepsilon} - C_{1\varepsilon}}{C_{1\varepsilon} - 1} = 2\eta_1 F_\mu \tag{78}$$

The left hand side in Eq. (78) is a constant, therefore it defines a curve $\eta_1 =$ function (η_2/η_1). There are several constrains of the function [18]: 1) the model should bifurcate only between two possible stable solutions $(P/\varepsilon)_\infty = (C_{2\varepsilon} - C_{1\varepsilon})/(C_{1\varepsilon} - 1)$ and $(\varepsilon/Sk)_\infty = 0$; 2) the bifurcation diagram should have a maximum value of ε/Sk close to Ω/S = 0.5, according to the Rapid Distortion Theory (Sahli et al. [27]) restabilization, $P/\varepsilon < 1$, should occur near to Ω/S = 0 and Ω/S = 1 in homogeneous shear flow.

Following the bifurcation diagram of SSG model [26] in rotating parallel shear flow, where the trivial solution $(\varepsilon/Sk)_\infty = 0$ occurs at $\Re = 1 + C_r Ro = \pm 1.39$, Reif and Durbin [18] developed the modified eddy viscosity coefficient, and it is in the form

$$C^*_\mu = C_\mu F_1 F_2 \tag{79}$$

where F_1 and F_2 are introduced to separately determine the model behavior for $|\Re| > 1$ and $|\Re| < 1$, repectively. Among many possible forms, they chose the following relations

$$F_1 = \frac{1}{1 + \alpha_1\sqrt{\eta_2}\sqrt{|\eta_3| - \eta_3}}$$

$$F_2 = \frac{1 + \alpha_2|\eta_3| + \alpha_2\eta_3}{1 + \alpha_4|\eta_3|}$$

$$\eta_3 \equiv \eta_1 - \eta_2 \tag{80}$$

The final form of the model can be written as

$$C_\mu^* = C_\mu \frac{1 + \alpha_2|\eta_3| + \alpha_2\eta_3}{1 + \alpha_4|\eta_3|}\left(\sqrt{\frac{1 + \alpha_5\eta_1}{1 + \alpha_5\eta_2}} + \alpha_1\sqrt{\eta_2}\sqrt{|\eta_3| - \eta_3}\right)^{-1} \tag{81}$$

The model coefficients are given by

$$\alpha_1 = 0.055, \alpha_2 = 0.5, \alpha_3 = 0.25, \alpha_4 = 0.2, \alpha_5 = 0.025 \tag{82}$$

The bifurcation diagram is shown in the Fig. 4.3. It is compared to the SSG model. Their model bifurcates to the trivial solution $(\varepsilon/Sk)_\infty = 0$ very close to the SSG model at $\mathfrak{R} = \pm 1.39$. Those coefficients in Eq. (82) are further modified to address the wall-bounded, non-equilibrium flows [18].

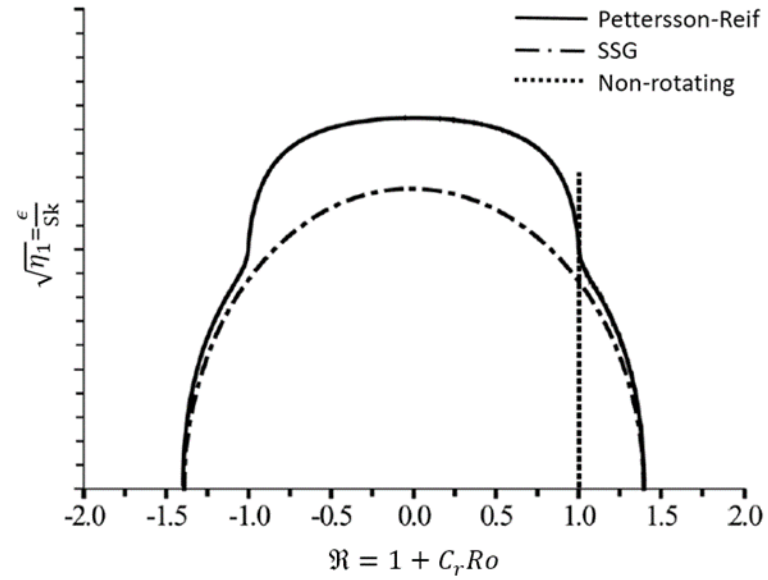

Figure 4.3 Bifurcation diagram [15].

In the following sections, we introduce two correction methods from "Modified Coefficients Approach" and one from "Bifurcation Approach."

4.6 Spalart-Shur RC Correction

As described by Shur et al. [17], to account for the effects of rotation and curvature in an eddy viscosity turbulence model, the Spalart-Shur correction has been extensively used in the literature which is described by empirical function given in Eq. (83). This function multiplies the production term in the SA eddy viscosity transport equation and multiplies the production terms of both *k* and *ω* equation in the SST *k*-*ω* model. In WA model, the source term $(C_1 RS)$ is multiplied by this function.

$$f_{r1}(r^*, \tilde{r}) = (1 + c_{r1}) \left[\frac{2r^*}{1 + r^*}\right] [1 - c_{r3} \tan^{-1}(c_{r2}\tilde{r})] - c_{r1} \tag{83}$$

where r^* and $\tilde{r}$ are non-dimensional quantities given by the equations:

$$r^* = \frac{S}{\omega}, \qquad \tilde{r} = \frac{2\omega_{ij} S_{jk}}{D^4} \left[\frac{\mathrm{D}S_{ij}}{\mathrm{D}t} + (\varepsilon_{imn} S_{jn} + \varepsilon_{jmn} S_{in}) \grave{\Omega}_m\right] \tag{84}$$

$$S_{ij} = \frac{1}{2}\left(\frac{\partial u_i}{\partial x_j} + \frac{\partial u_j}{\partial x_i}\right), \qquad \omega_{ij} = \frac{1}{2}\left[\left(\frac{\partial u_i}{\partial x_j} - \frac{\partial u_j}{\partial x_i}\right) + 2\varepsilon_{mji}\grave{\Omega}_m\right] \tag{85}$$

$$S^2 = 2S_{ij}S_{ij}, \qquad \omega^2 = 2\omega_{ij}\omega_{ij} \tag{86}$$

$$D^2 = S^2 + \omega^2 \tag{87}$$

The derivative $\mathrm{D}S_{ij}/\mathrm{D}t$ in Eq. (84) is the Lagrangian derivative of the strain tensor. All derivatives are defined with respect to the reference frame with a rotation rate $\grave{\Omega}_m$. For the finite volume method based CFD codes, it is more convenient to represent this derivative using an Eulerian formulation. The recommended values of the three constants in Eq. (83) are c_{r1} = 1.0, c_{r2} = 12.0, and c_{r3} = 1.0 [4]. The procedure for implementing Eq. (83) is given in Ref. [17] and was used in the OpenFOAM implementation for the results reported in this thesis. In rest of the thesis, the Spalart-Shur correction will be simply denoted by the letters “RC”.

4.7 Zhang-Yang Correction

The appearance of the term $\mathrm{D}S_{ij}/\mathrm{D}t$ in Eq. (84) increases the programming complexity and computational cost, especially for transient simulations. To address this problem, the Richardson number Ri given by Eq. (88) in the form described by Hellsten [28] has been used by Zhang and Yang [29] to develop the rotation & curvature correction for eddy viscosity turbulence models.

$$Ri = \frac{\omega}{S}\left(\frac{\omega}{S} - 1\right) \tag{88}$$

Richardson number given by Eq. (88) is a measure of the mean-flow deformation, thus it can reflect the effects of rotation and curvature. Therefore the rotation and curvature factor $\tilde{r}$ used in Eq. (84) can be replaced by

$$\tilde{r} = \frac{\omega}{S}(\frac{\omega}{S} - 1) \tag{89}$$

In Eq. (89), $\tilde{r}$ is the equation of a parabola with the global minimum value of -0.25 when S/ω is equal to 0.5. Now, a modified rotation-curvature correction abbreviated as RCM can be obtained by employing the Richardson number as a correction factor to account for the effects of rotation and curvature. In general, Zhang and Yang [29] rotation and curvature correction is numerically more stable, converges faster and is easier to implement than the Spalart-Shur correction. After some trial and error, the three model constants in Eq. (83) were calibrated as c_{r1} = 1.0, c_{r2} = 2.0, and c_{r3} = 0.6 for the WA2017m-RCM model.

4.8 Arolla Correction

Arolla's correction [19] was developed for SST *k*-*ω* model. Similar to the method by Reif and Durbin [18], to mimic the bifurcation behavior of RSMs, Arolla [19] introduced a correction to the eddy viscosity coefficient as $\nu_t = C_\mu^* k/\omega$, where

$$A = C_\mu \left(\alpha_1(|\eta_3| - \eta_3) + \sqrt{1 - min(\alpha_2\eta_3, 0.99)}\right)^{-1} \tag{90}$$

$$C_\mu^* = min(2.5, A) \tag{91}$$

$$\eta_1 = S_{ij}S_{ij}T^2;\ \ \eta_2 = \Omega_{ij}^{mod}\Omega_{ij}^{mod}T^2;\ \ \eta_3 = \eta_1 - \eta_2 \tag{92}$$

$$T = max(T_1, T_3)\,;\ T_1 = \frac{1}{\beta^*\omega};\ T_2 =\ 6\sqrt{\frac{\nu}{\beta^*k\omega}}; T_3 = (T_1^n T_2)^{1/n+1}; n = 1.625 \tag{93}$$

Based on the bifurcation diagram of RSMs, the constant coefficients $\alpha_1 = 0.04645$ and $\alpha_2 = 0.25$ are selected. The invariants used in the models are defined in Eq. (92).

Chapter 5: Uncertainty Quantification

Uncertainty Quantification (UQ) can be used to assess the effect of variations in the turbulence model coefficients on the computed results. UQ is the process of determining the effect of input uncertainties on the response metrics of interest. These input uncertainties may be characterized as either aleatory uncertainties which are irreducible variabilities inherent in nature, or epistemic uncertainties which are reducible uncertainties resulting from a lack of knowledge (which is the case with turbulence models).

In the previous literature, Schaefer et al. [30] and Stephanopoulos et al. [31] have applied the Non-Intrusive Polynomial Chaos (NIPC) to quantify the uncertainty in closure coefficients of commonly used RANS turbulence models. It is of interest to investigate the uncertainty in the coefficients of rotation and curvature corrections in a turbulence model. In this study, we select WA2017m along with Spalart-Shur RC correction and use NIPC to assess the uncertainty in the three coefficients in the RC correction. DAKOTA is used to compute the Sobol indices which represent the sensitivity of each coefficient to some physical quantity of interest. The strategy of NIPC is to create a surrogate model via Least-Squares approach by using the CFD output obtained at a number of Latin Hypercube sample points for the propagation of uncertainty. There are three parameters which determine the number of samples required to generate the response surface: the number of uncertain variables n, the order of the response surface polynomial p, and the oversampling ratio n_p. The total number of samples N_S is then given by Eq. (94). A summary of the computational parameter used in UQ analyses of WA2017m with RC is given in Table 5.1.

$$N_s = n_p \left[\frac{(n+p)!}{n!\,p!} \right] \tag{94}$$

Table 5.1 Computational parameters used in UQ analysis of WA2017m-RC.

Turbulence model	n	p	n_p	N_s
WA2017m-RC	3	2	2	20

For UQ analysis, flow in a U-turn duct is selected as the benchmark case. The computational details for this case are provided in the next section. The Sobol indices of three RC model coefficients in WA2017m-RC model described above are plotted along the inner and outer wall with respect to coefficient of pressure C_p and coefficient of skin-friction C_f. The value of Sobol indices change dramatically near the U-turn section of the duct as shown in Fig. 5.1. Model coefficient c_{r2} in WA2017m-RC model dominates both in the calculation of pressure coefficient C_p and skin friction coefficient C_f, which indicates that modification of c_{r2} should be considered in improving the model's predictions.

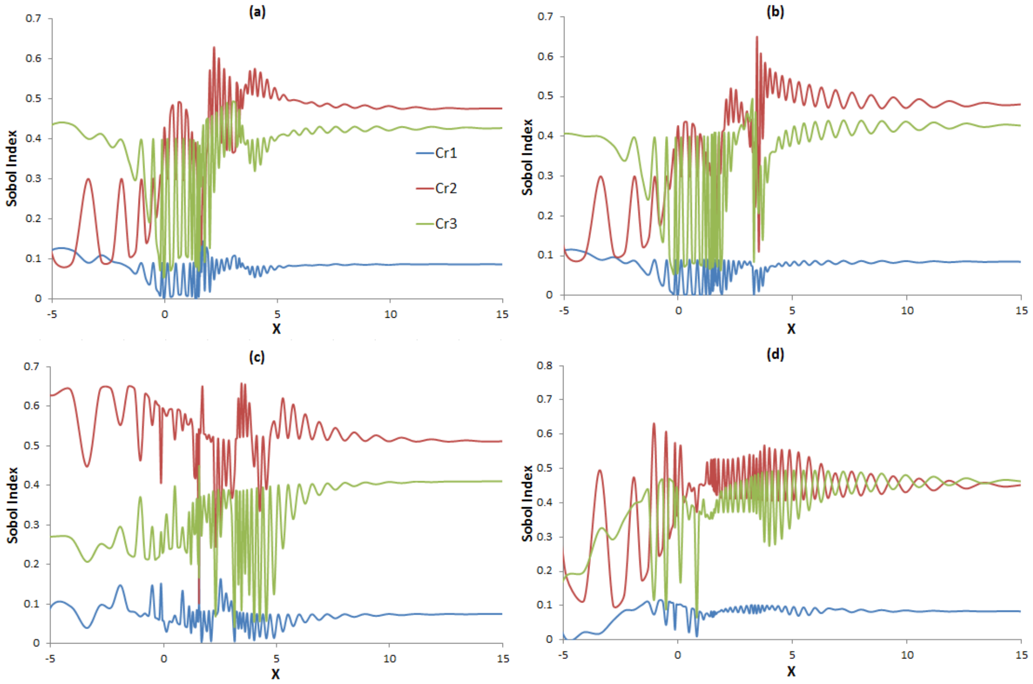

Figure 5.1 Sobol indices of WA2017m-RC model coefficients with respect to (a) C_p along the inner wall, (b) C_p along the outer wall, (c) C_f along the inner wall and (d) C_f along the outer wall.

Therefore, first the closure coefficient c_{r2} was modified since it is most dominant among the three coefficients in contributing to uncertainty. It was fixed at $c_{r2} = 0.5$ and the closure coefficient c_{r3} was modified since it is the second most important contributor to uncertainty. Changes in the closure coefficient c_{r1} appeared to contribute little to the uncertainty in the predictions. Figure 5.2 shows the results of trial and error process used in tuning the coefficients and Table 5.2 gives the optimal combination of the closure coefficients. As can be seen, the modified RC coefficients in WA2017m-RC (red line) are giving much better predictions for C_p and C_f than the original WA2017m-RC model (blue line). The three RC closure coefficients for original and modified WA2017m-RC models are summarized in Table 5.2.

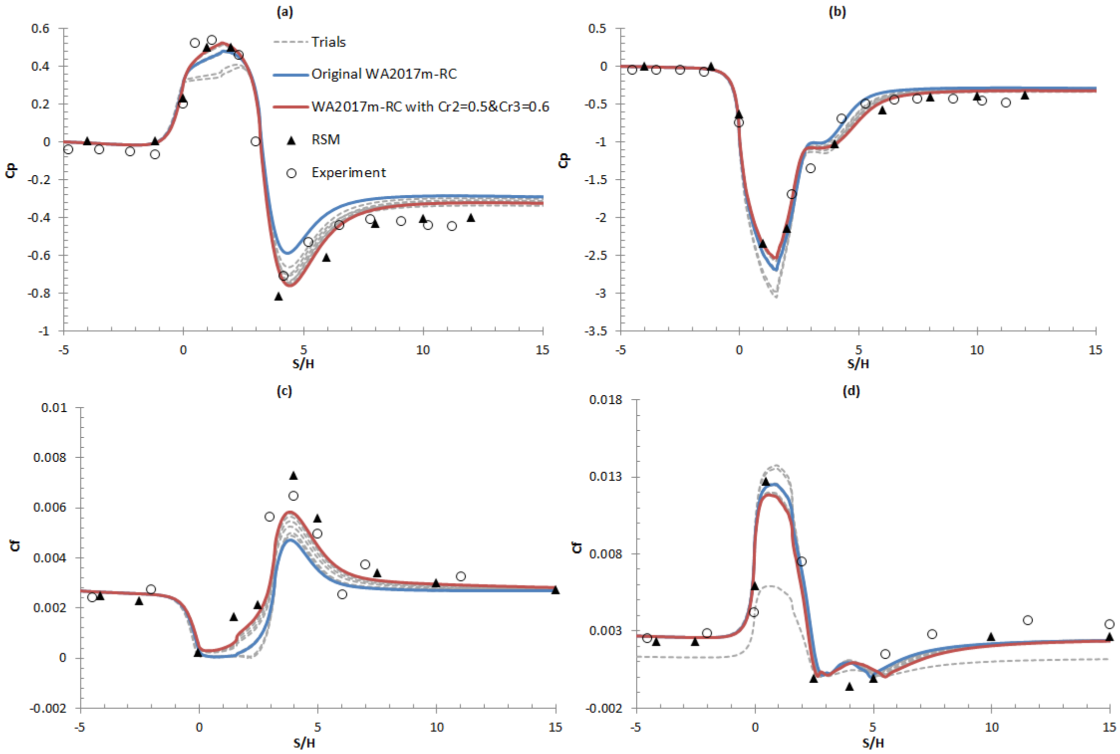

Figure 5.2 Results for (a) C_p along the outer wall, (b) C_p along the inner wall, (c) C_f along the outer wall and (d) C_f along the outer wall using the trial and error process for values of coefficients c_{r1}, c_{r2} and c_{r3}.

Table 5.2 Closure coefficients for original and modified WA2017m-RC model.

Turbulence model coefficient	c_{r1}	c_{r2}	c_{r3}
Original WA2017m-RC	1.0	12.0	1.0
Modified WA2017m-RC	1.0	0.5	0.6

In the following section, WA2017m-RC model with the modified values of RC coefficients c_{r1}, c_{r2} and c_{r3} is applied in simulations and from now on it will be referred to as the WA2017m-RC model. As mentioned before, there is little difference in results obtained using the hyperbolic tangent function or the minimum function for the destruction term E_R in Eq. (33); thus all the results in Chapter 6 are based on the hyperbolic tangent function for E_R.

Chapter 6: Validation Cases

6.1 Wall Bounded Flow

6.1.1 2D Curved Duct

This flow is considered to assess the capability of three turbulence models with rotation and curvature correction to capture the effects of curvature on the turbulent boundary layer. This flow is computed at flow conditions corresponding to the experiment of Smits et al. [32]. The experiment measured the flow through a constant area square duct of height 0.127 m with a rapid 30^o bend. The aspect ratio of the experimental duct was 6:1; therefore this case is modeled as a 2D curved duct in this thesis. The experiment showed the presence of Gortler vortices which cannot be predicted by the 2D simulation. For this reason, comparison of the 2D CFD and 3D experimental results should be considered with caution keeping in mind the limitations of the 2D simulation; nevertheless a comparison of results using various models can still be useful.

The Reynolds number of the flow is $Re = 2.1 \times 10^6$ based on the inlet flow velocity and a reference length of one meter. The computational grid was taken from the NASA Turbulence Modeling Resource [33] website. Computations were performed with OpenFOAM using an incompressible steady-state solver with second order discretization scheme. The standard versions of the SA and SST k-ω models have already been implemented in OpenFOAM and have been validated for the case of subsonic flow past a flat plate from the NASA Turbulence Modeling Resource (TMR) website. The computational grid with every other node is shown in Fig. 6.1 (a) and the coordinate system is shown in Fig. 6.1 (b).

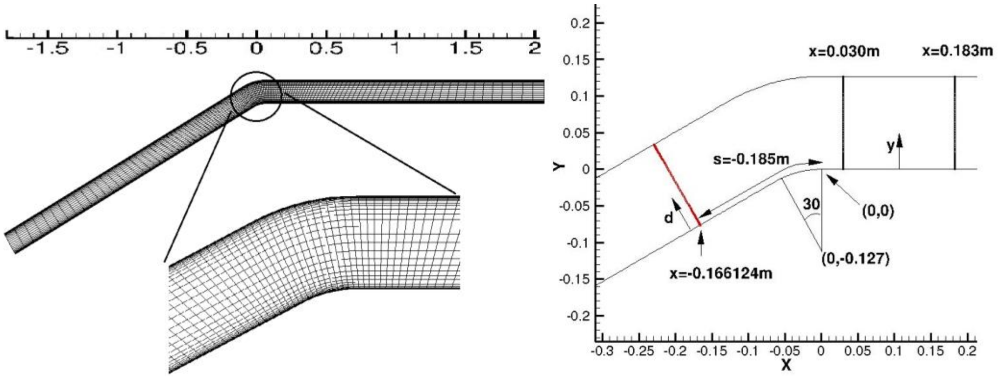

(a) **(b)**

Figure 6.1 (a) Computational grid and (b) coordinate system for the curved duct from Ref. [33].

Figure 6.2 shows the calculated and experimental values of the pressure coefficient C_p along the convex wall of the duct. It can be noted that there is no discernible difference in the results obtained from different turbulence models; all are in excellent agreement with the experimental data. The addition of the RC and RCM correction has little effect on the pressure coefficient. Comparisons of the calculated and experimental skin friction coefficients C_f are shown in Fig. 6.3. The positive effect of RC correction is clearly demonstrated in this figure. The results of the SA-RC and SST-RC are in excellent agreement with FUN3D results from the NASA TMR [33], verifying their correct implementation in OpenFOAM. An improvement in the accuracy of SA and SST k-ω model is obtained with the addition of the RC correction. WA2017m model also performs quite well; the RCM correction to WA2017m model provides slight improvement. WA2017m-Arolla and WA2018-RC are not as good as original WA2017m model. While WA2018EB-RC does fairly well in capturing the minimum and downstream value of C_f. Three best results from each models (SA, SST and WA) are plotted in the same graph as shown at the bottom right in Fig. 6.3.

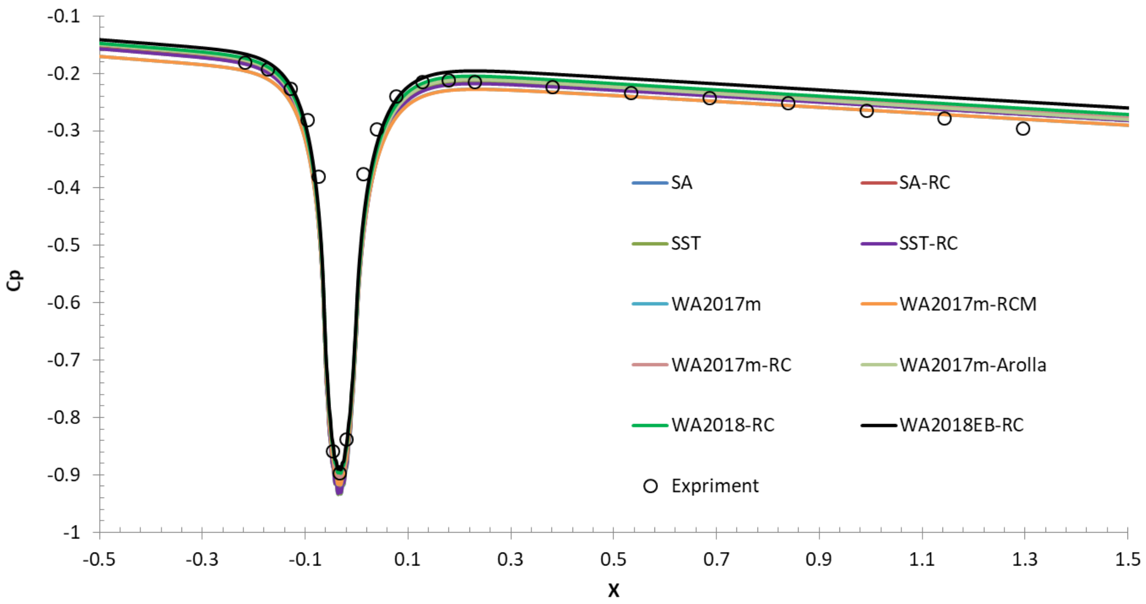

Figure 6.2 Comparison of pressure coefficient along the convex wall of the curved duct.

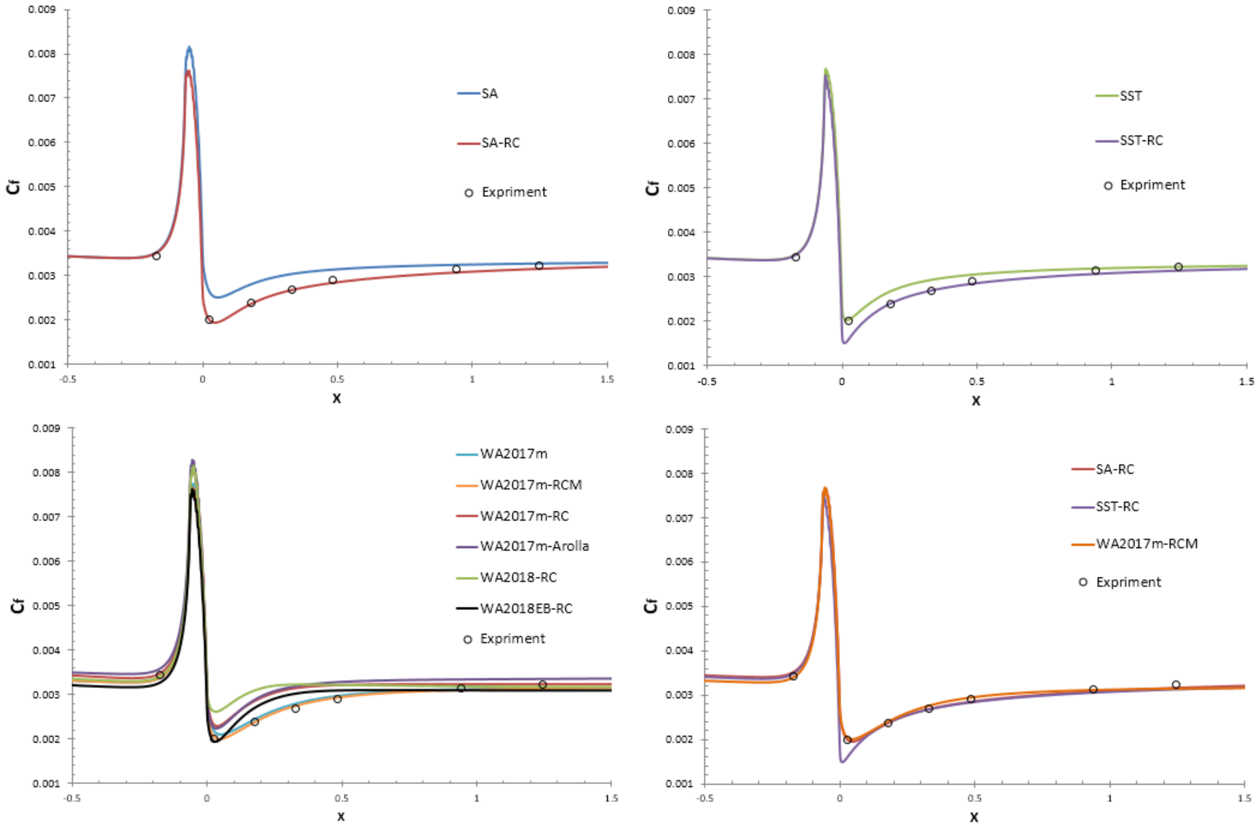

Figure 6.3 Comparison of skin friction coefficient along the convex wall of the curved duct.

6.1.2 2D U-turn Duct

To understand and validate the effect of RC correction methods on the turbulence models, the flow through a U-duct was computed and the results were compared with the experimental data and full Reynold Stress Model (RSM) results. Strong streamline curvature as well as the formation of a separation bubble make this case very challenging for linear eddy-viscosity turbulence models. The flow conditions correspond to the experiment of Monson et al. [34]. The Reynolds number of the flow is $Re = 10^6$ based on the mean flow velocity and channel height. The solution was obtained on a 204×100 grid which is shown in Fig. 6.4. For clarity only every second grid point is shown in Fig. 6.4. The simulation was conducted in OpenFOAM using the second order accurate SIMPLE algorithm. The results of computations are presented in Figs. 6.5-6.9.

Figure 6.4 Two-dimensional grid (204×100) inside the U duct.

Figure 6.5 shows the comparison of simulations using various models with the experimental data and the Reynolds Stress Model (RSM) results [35] for pressure coefficient on the outer wall of the duct. It can be seen that before S/H~3, there is no clear distinction among the results from various models. After S/H~3, the positive effect of the Spalart-Shur RC correction is clearly evident. Both the SA-RC and SST-RC more accurately predict the pressure coefficient along the outer wall than the standard models without curvature correction. However, the results from WA2017m-RC (blue line) and WA2018EB-RC (back line) are the most accurate among all the models considered in this study. They are not only successful in capturing the minimum value of C_p but are also fairly accurate in calculating C_p in the reattached region. While the SST-RC model accurately estimates the C_p downstream of the duct at cross section θ = π (at the end of the turn), it completely misses the minimum value of C_p. Compared to SA-RC and WA2017m-RC, WA2017m-RC performs slightly better than SA-RC both in the separation region and in the downstream region. WA2017m-RC and WA2018EB-RC do not perform very accurately in the downstream region like any other models except SST-RC.

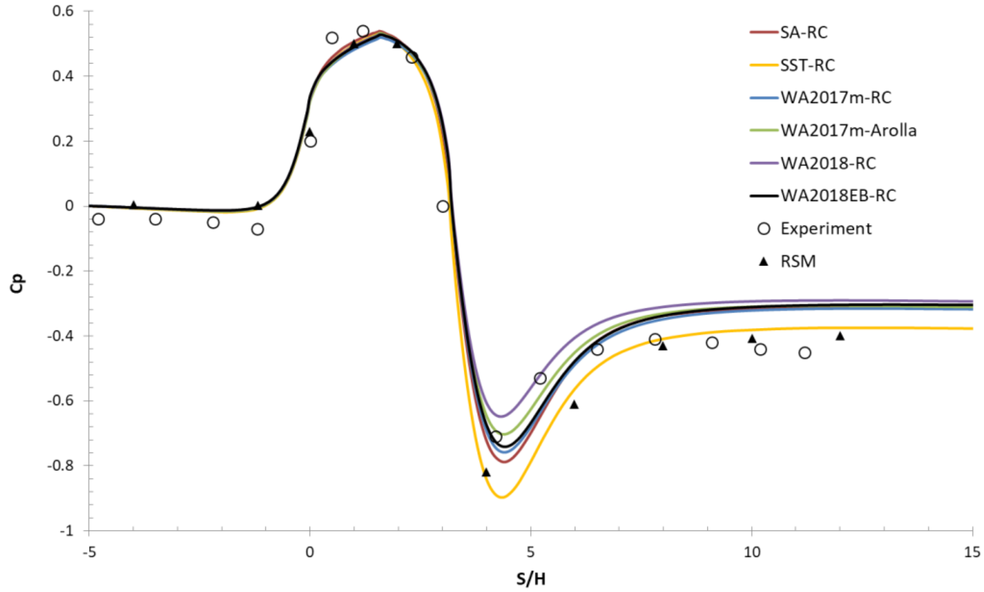

Figure 6.5 Surface pressure coefficient C_p along the outer boundary of the U-duct.

Figure 6.6 shows the surface pressure coefficient C_p along the inner wall of the U-duct. From this figure, it is difficult to distinguish among the simulations from all the models. However, it is clear that both RC and Arolla corrections have positive effect on the accuracy of simulations. All the models calculate the almost same minimum value of C_p, but there are only two experimental data locations available along the U-turn section. By comparing with the RSM results, both RC and Arolla corrections give reasonable predictions. In the reattached flow region, WA2017m-Arolla and WA2018EB-RC are slightly better than other models.

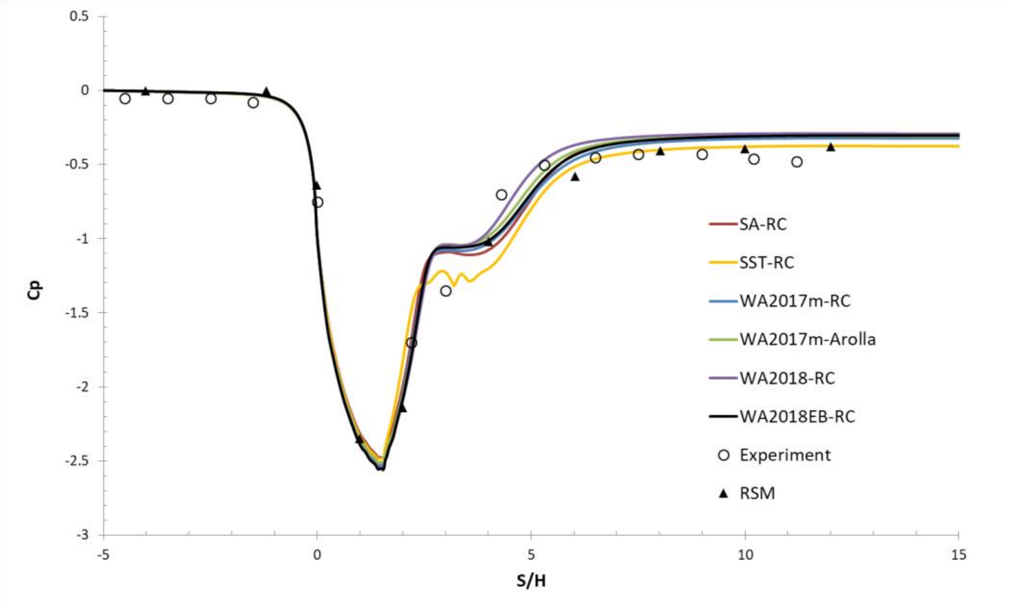

Figure 6.6 Surface pressure coefficient C_p along the inner boundary of the U-duct.

Figures 6.7 and 6.8 show the skin friction coefficient C_f along the outer and inner walls of the U-duct respectively. In Fig. 6.7, the WA2018-RC and WA2018EB-RC models underestimate the C_f in the upstream region before $\theta = 0$ (beginning of the U-turn of the duct), which affect the U-turn section and downstream value. In general, none of the turbulence models employed in this study accurately capture all the features in this case. As for the minimum value of C_f after $\theta = \pi$ (the end of U-turn), WA2018-RC and WA2018EB-RC are the only two models that predict the accurate value, but they completely miss the peak value of C_f. SST-RC model gives accurate prediction in the upstream and downstream region and also along the U-turn section, while it is way off the minimum value of C_f. SA-RC, WA2017m-RC and WA2017m-Arolla models underestimate the maximum value of C_f. WA2017m-RC and SST-RC appear to be the two best models that capture the overall trend of the C_f with respect to the experimental data and RSM results.

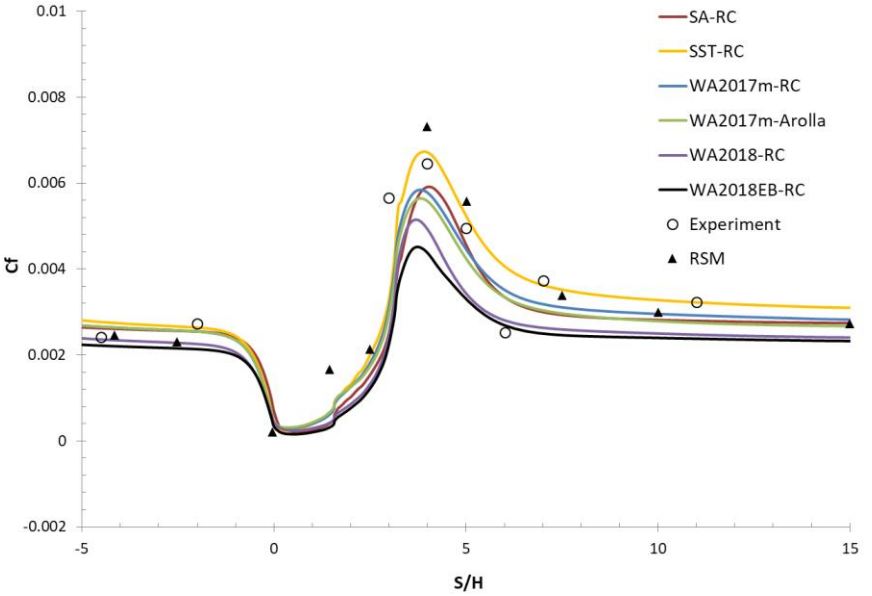

Figure 6.7 Skin friction coefficient C_f along the outer boundary of the U-duct.

In Fig. 6.8, WA2018-RC and WA2018EB-RC models again underestimate the C_f in the upstream region before θ = 0 (beginning of the U-turn of the duct). There is only one experimental data point between S/H=0 and S/H=5, therefore it is difficult to make an assessment of how these models perform along the U-turn section of the duct. Nevertheless, comparing the results among the models themselves, WA2018-RC predicts larger maximum value of C_f than other models, which is close to the RSM result. All the models fail to predict the downstream C_f after S/H~6 compared to the experimental data, but the results of WA2017m-RC and WA2017m-Arolla are close enough to the RSM results.

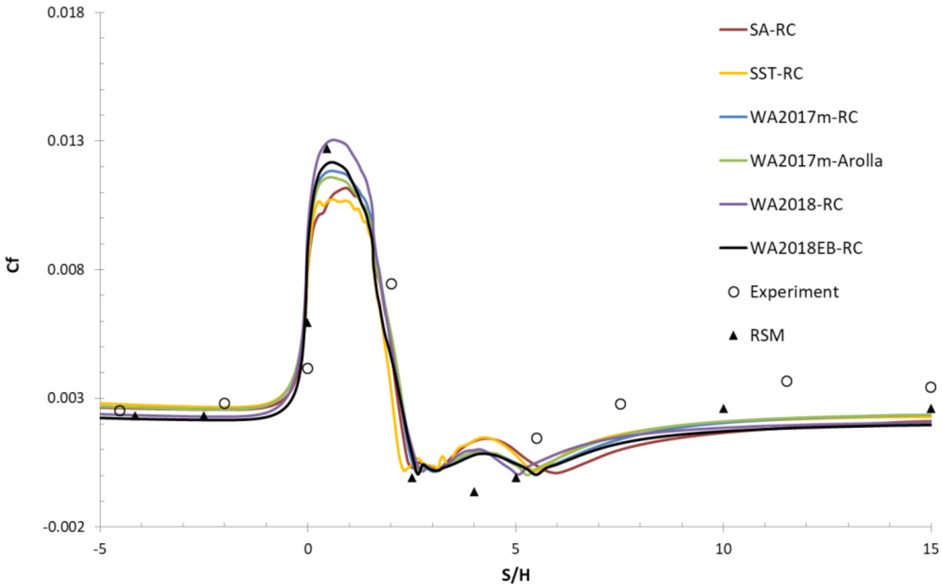

Figure 6.8 Skin friction coefficient C_f along the inner boundary of the U-duct.

As expected, all the solution trends described above for the pressure and skin friction distributions are also found in the velocity profiles shown in Fig. 6.9. At sections θ = 0 and θ = π/2 of the U-turn of the duct, the results obtained from all the models have slight differences but overall are in reasonable agreement with the experimental data. After flow separation at θ = π section, the results deviate significantly from each other, and none of the models accurately determines the velocity profile. From the bottom right plot in Fig. 6.9, where the flow is at θ = π+2, it can be seen that all models overestimate the length of the recirculation region and predict a very slow recovery after reattachment.

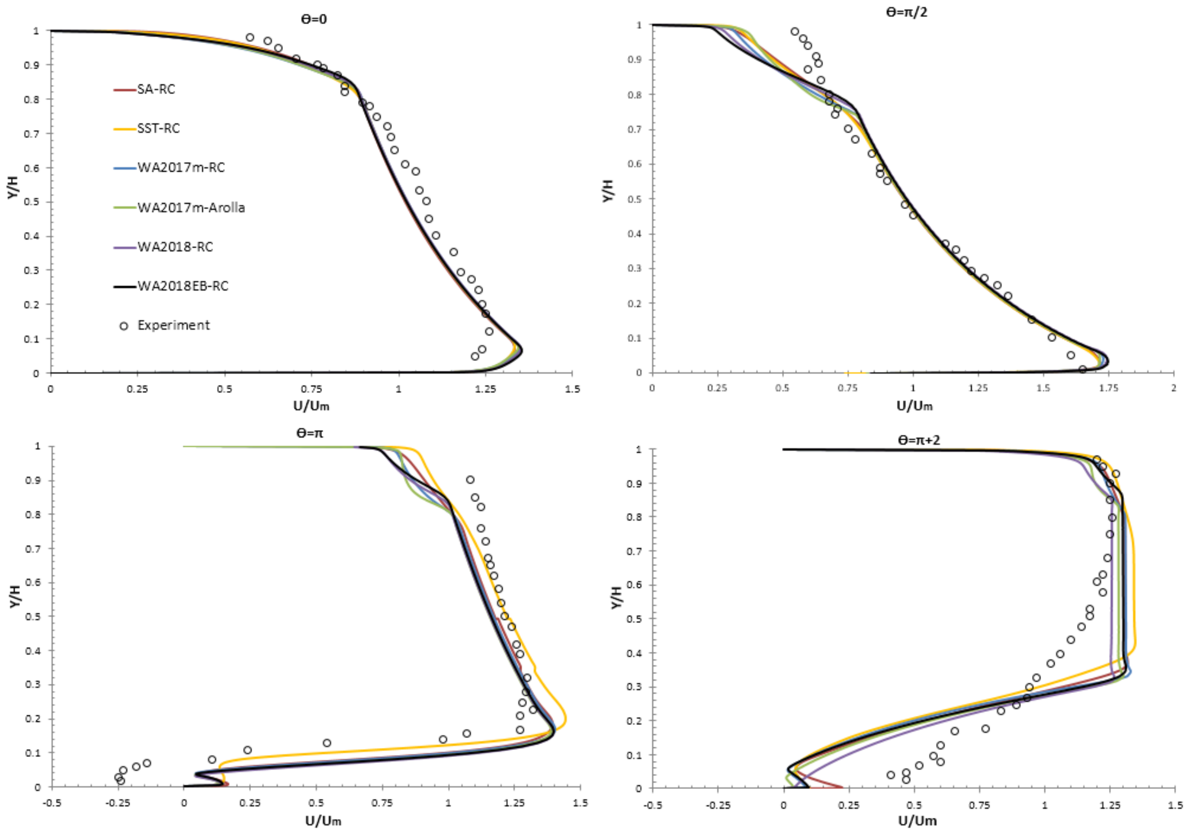

Figure 6.9 Velocity profiles at different sections of the U-duct.

6.1.3 2D Rotating Channel

A rotating body/system experiences Coriolis and centrifugal forces in a fixed inertial frame. These forces affect the turbulence in the system. Depending upon the magnitude and orientation of the rotation vector; turbulence can be enhanced or suppressed.

The most frequently used test case for assessing the accuracy of a turbulence model in a rotating frame is the 2D fully developed flow in a planar channel rotating about an axis perpendicular to the flow vectors as shown in Fig. 6.10. This configuration has been studied experimentally by Halleen and Johnston [36] and Johnson et al. [37], and numerically employing DNS by Kristoffersen and Andersson [38] and by Lamballais et al. [39]. In current study, SRFSimpleFoam solver in OpenFOAM is used to perform the simulation. Let u_R be the relative flow velocity. The governing equations for incompressible turbulent flow are

$$\nabla \cdot u_R = 0 \tag{95}$$

$$\nabla \cdot (u_R u_R) + 2\Omega \times u_R + \Omega \times (\Omega \times r) = -\nabla p + \nabla \cdot (\upsilon_{eff}(\nabla u_R + (\nabla u_R)^T)) \tag{96}$$

In Eq. (96), the second term on the left hand side represents the Coriolis force while the third term represents the centrifugal force. For the computations, Eq. (96) is rearranged such that the centrifugal force term is absorbed in the pressure term. Consider fully developed channel flow, $u_R = (U(y), 0,0)$ which is subjected to a constant angular velocity $\Omega = (0,0,\Omega)$ about the z-axis as shown in Fig. 6.10. Simulation results are compared with the DNS data of Kristoffersen and Andersson [38] at $Re_\tau \equiv hu_\tau/\nu = 194$ for four different rotation numbers $Ro \equiv 2h\Omega/U_m = 0, 0.1, 0.2,$ and 0.5. The friction velocity $u_\tau \equiv \sqrt{\tau_w/\rho}$ is calculated for the non-rotating channel to make sure that Re_τ is equal to 194. The grid size is 4 × 200 which is sufficient to ensure a grid independent numerical solution.

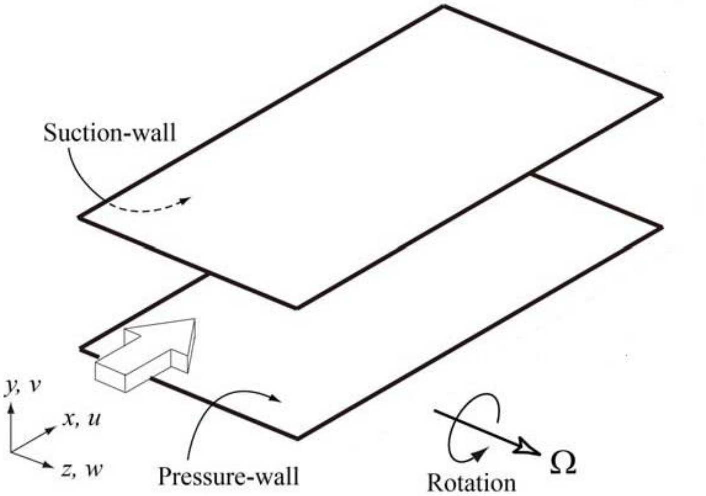

Figure 6.10 Rotating channel and coordinate system.

For this case, WA2017m-RCM model fails to accurately predict the velocity distribution across the width of the channel due to limitation of the RCM correction for rotating flows. Therefore for this case, we employ the RC correction to different versions of WA models and also use the SA-

RC, SST-RC and WA2017m-Arolla models to perform the simulation. The mean velocity distribution scaled by $1/U_m$ in Fig. 6.11 shows the characteristic asymmetry caused by the rotation. The predictions from all models are in close agreement with the DNS data for all *Ro* and are capable of reproducing the almost irrotational core region in which $dU/dy \sim 2\Omega$. SA-RC and WA2017m-RC models almost predict the same profile at low *Ro*, but at high *Ro* (e.g. *Ro* = 0.5), WA2017m-RC results match the DNS data best among the three models and also WA2018-RC model is very close to WA2017m-RC. At low *Ro* (e.g. *Ro* = 0.1, 0.2) WA2018EB-RC is accurate on the suction side while not very accurate on the pressure side. WA2017m-Arolla is fairly accurate on the pressure side for all the three rotation numbers.

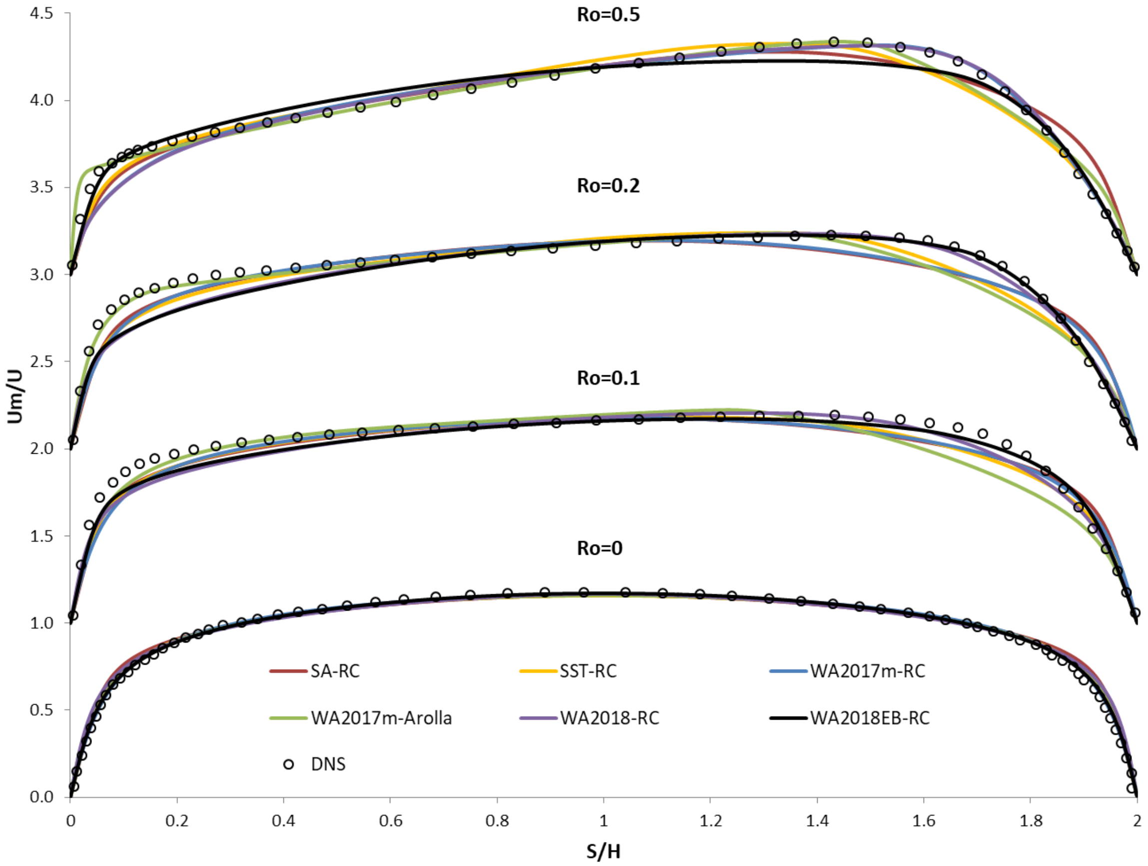

Figure 6.11 Velocity distribution in the channel at different rotation numbers.

6.1.4 2D Stationary and Rotating Backward-facing Step

The backward-facing step configuration is rotated about a span-wise axis such that the sudden expansion of the channel is on the pressure side. The upstream flow is fully developed and is subjected to orthogonal mode rotation, which results in detaching the separation bubble from the step corner and eventually reattaching it further downstream as illustrated in Fig.6.12. Flow separation also occurs at the upper wall when the Ro increases. If the rotation is in the direction of the mean shear, the turbulent mixing is enhanced and the size of the recirculation bubble decreases. If the rotation is anti-parallel to the direction of mean shear, the turbulent mixing is suppressed and the size of the recirculation bubble increases. We use the recent DNS data from Barri and Andersson [40] at $Re = U_b(H-h)/\nu = 5600$ to assess the rotation and curvature correction to this complex flow configuration. The expansion ratio is $ER = H/(H-h) = 2$ with h being the step height and H being the downstream height of the channel. Following the DNS setup, the span-wise rotation is imposed such that the turbulence over the stepped wall is enhanced and over the opposite wall is suppressed.

The definition of rotation number is $Ro = \Omega(H-h)/U_{b0}$ where U_{b0} is the bulk velocity upstream of the step in the stationary case. However, the local rotation number in the downstream part of the channel is 4 times greater than upstream because the bulk velocity U_b, downstream of the step is related to that upstream by $U_{b0}(H-h)/H$. Hence, the effect of rotation is much stronger downstream of the step.

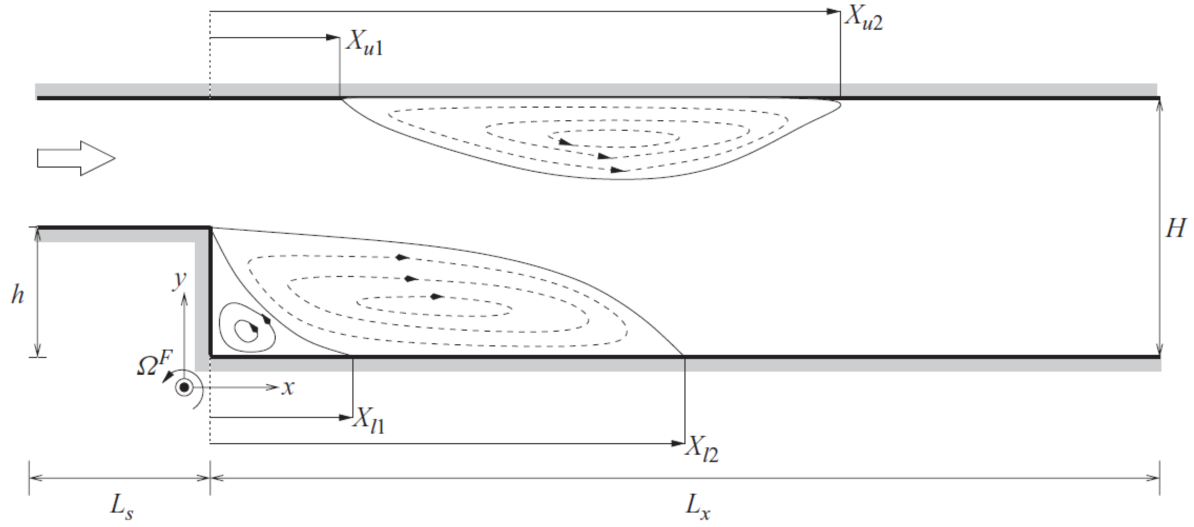

Figure 6.12 Schematic of the span-wise rotating backward-facing step from Ref. [40].

In a backward-facing step, the free-shear layer emanating from the step undergoes geometry induced separation. When subjected to rotation, the turbulence on this wall is amplified. Due to enhanced turbulence levels, higher momentum fluid away from the wall is transported towards the wall. This shortens the reattachment length. For the purpose of validation, we ran the stationary case with a very long upstream channel (36H) which allows the flow to be fully developed. Rotating cases were run at two different *Ro* = 0.05 and *Ro* = 0.2; in these cases rather than having the long upstream channel, we directly injected the fully developed velocity profile upstream from DNS data.

For this case, we employ the RC correction to SST and various WA models also along with WA2017m-Arolla to perform the simulation. Fig. 6.13 presents the mean velocity profile at *x/h* = 0, 1, 2, 4, 7 and 24 for *Ro* = 0, 0.05 and 0.2.

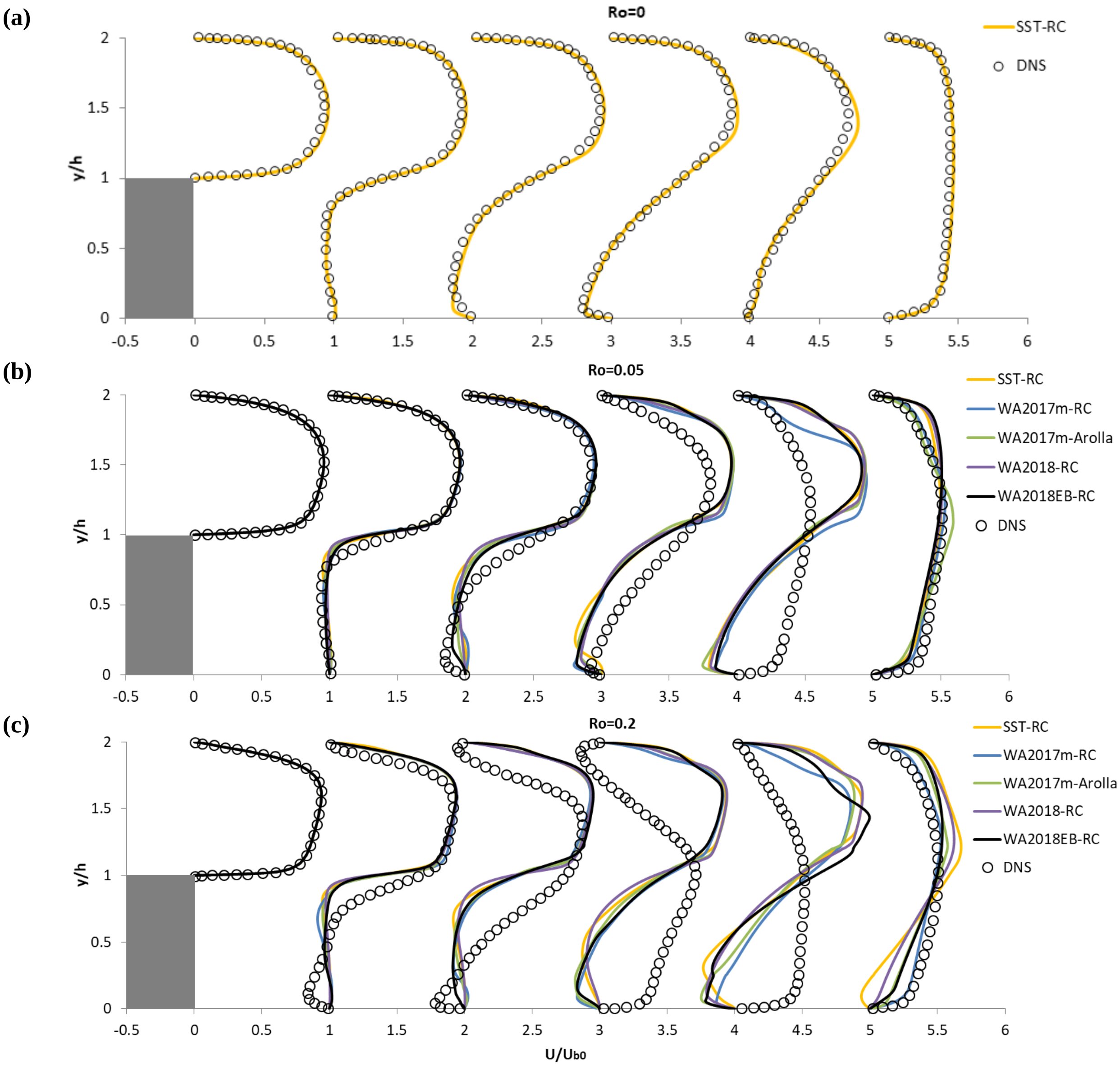

Figure 6.13 Comparison of mean velocity profile at (a) *Ro* = 0, (b) *Ro* = 0.05, and (c) *Ro* = 0.2 at multiple locations x/h = 0, 1, 2, 4, 7 and 24 on backward facing step.

The stationary result without rotation in Fig. 6.13 (a) matches with the DNS data quite well and predicts the accurate reattachment length. The results from different models hardly differ from each other; therefore for clarity only the result from SST-RC is given. However, the situation changes after imposing the rotation. All the models completely fail in computing the reattachment location and predict a very slow recovery. At moderately high rotation number (*Ro* = 0.2) in Fig. 6.13 (c), DNS data shows a separation bubble on the upper wall, opposite to the step, which is due to the stabilizing effect of rotation on that wall. The turbulence is suppressed on this surface and hence the flow is susceptible to separation. None of the models successfully capture this feature.

In general, all the models completely fail to capture the accurate velocity profile and over predict the reattachment location.

6.1.5 Rotating Cavity

The flow inside a rotating cavity is of basic interest in fluid mechanics; it is a common feature in rotating machinery and in particular in gas turbine engine compressor and turbine rotor assemblies. This configuration is also well suited for meteorological studies of the Earth's lower atmosphere. In case of a radial outflow, the mean secondary flow in the cavity can be characterized by a rotating inviscid core and two disk boundary layers. The flow structure may be highly complex with the coexistence of laminar and turbulent flow regions and/or the presence of three-dimensional vortical structures embedded in a turbulent flow regime. For several decades, the problem has been addressed by many authors with different approaches and for different applications. The case of radial outflow was investigated by Breiter and Pohlhausen in 1962 to study the performance of parallel disk pumps [41]. From a brief literature review, this arrangement is very challenging for turbulence modeling. The main objectives of this study are the calculations of turbulent flow fields of a rotating cavity with radial outflow, and radial and axial inflow.

Radial Inflow

The cavity sketched in Fig. 6.14 is formed by two smooth parallel disks of outer radius R_o = 190 mm and inner radius R_i = 19 mm separated by an axial gap h = 50.73 mm. All walls rotate at the same rotation rate Ω. A volume flow rate Q of air is supplied radially to the cavity through the entire disk gap h. The mean flow is mainly governed by four flow control parameters: the aspect ratio of the cavity L, its radius ratio s, the rotational Reynolds number Re based on the outer radius of the rotating disk R_o and the volume flow rate coefficient C_w, where ν is the fluid kinematic viscosity.

$$L = \frac{R_o - R_i}{h} = 3.37 \qquad s = \frac{R_i}{R_o} = 0.1 \tag{97}$$

$$Re = \frac{\Omega R_o^2}{\nu} = 10^5 \qquad C_w = \frac{Q}{\nu R_o} \tag{98}$$

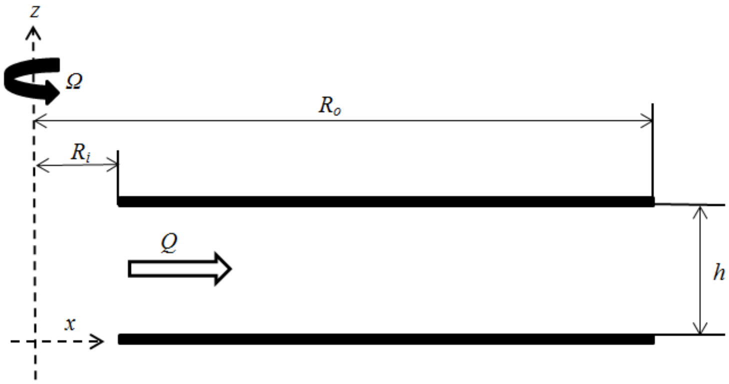

Figure 6.14 Sketch of rotating cavity with radial outflow and radial inflow.

Computations are performed using the RC correction applied to SA, SST, and various WA models and WA2017m-Arolla. For all models, a 160 × 100 mesh in the (r, z) frame provides a grid independent solution for the configuration corresponding to the experiments of Owen and Pincombe [42]. The computational domain is axisymmetric about the z-axis. The same initial and boundary conditions are imposed for all models. At the boundaries, all the variables are set to zero at the walls except for the tangential velocity, which is set to Ωr on the rotating walls. At the inlet, an averaged radial velocity is imposed with a given low level of turbulence (3%). The mean tangential velocity is also fixed to the disk speed. At the outlet, the pressure is set to a constant value. The following dimensionless quantities are defined: the radial position $r^* = (r - R_i)/(R_o - R_i)$ and axial position $z^* = z/h$.

The axial profile of the dimensionless tangential $V_\theta^* = V_\theta/(\Omega r)$ and $V_r/\ V_{rm}$ velocity profiles are displayed in Fig. 6.15 and 6.16 respectively at $r^* = 0.556$; $V_{rm}(= Q/(2\pi R_i h))$ is the mean radial velocity injected at the inlet. The predictions of the turbulence models are compared with the experimental measurements of Owen and Pincombe [42] and also with the RSM results from Poncet [43]. The flow is symmetrical about the mid-cavity plane $z^* = 0.5$. Fluid entering the cavity at $r^* = 0$ is progressively entrained from the source region into the entraining boundary layers along the rotating wall. For the tangential velocity, all the three models' calculation results are in reasonably good agreement with the experimental data and RSM result. Among these, WA2017m-RC model result matches with the experimental data and RSM result very closely especially in the mid-plane region. There are no available measurements very close to the disks but by comparing the computations with the RSM result, it is clearly shown that all three models fail to predict the thickness of the boundary layer for the V_r profiles. The discrepancies may be explained by the appearance of three-dimensional instabilities either in the core or in the boundary layers depending on the flow conditions [44]. These structures strongly affect the mean flow. Away from the rotating wall, WA2017m-RC prediction is again most close to the experimental data.

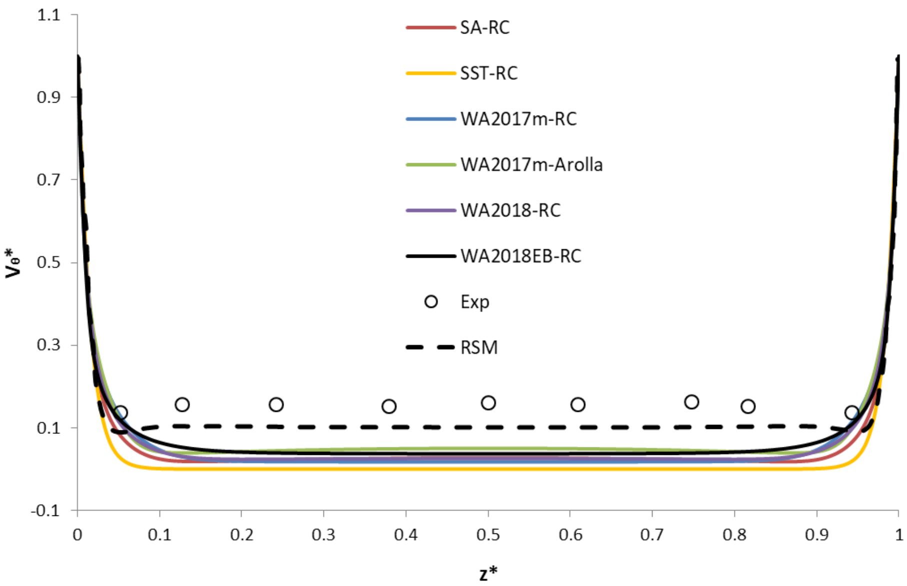

Figure 6.15 Axial distribution of the mean tangential velocity profile at *r = 0.556.**

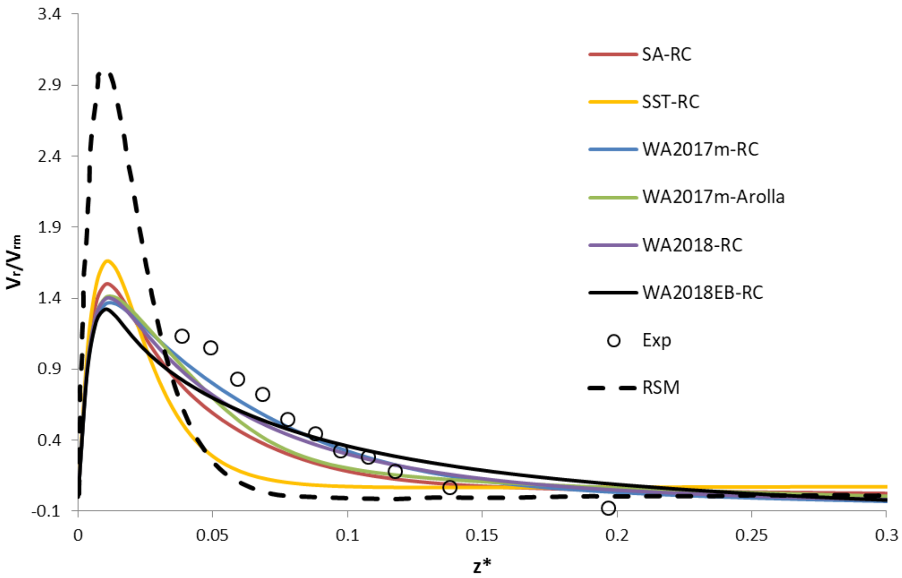

Figure 6.16 Axial distribution of the mean radial velocity profile at *r = 0.556.**

Axial Inflow

For the rotating cavity with axial inflow as sketched in Fig. 6.17, air enters the cavity axially through a central hole in the upstream disk and is deflected after impinging on the downstream disk; then, it exits through a small hole on the outer shroud. The flow is characterized by a toroidal vortex located close to the upstream disk and, depending on the rotational velocity, by the establishment of two symmetric boundary layers on the disks.

A 200 × 150 uniform grid was used for all calculations. Inner and outer radius are exactly the same as in the radial flow case with R_o = 190 mm and R_i = 19 mm. The flow conditions are characterized by the rotation number $Ro \equiv \Omega s/U_i$ and the Reynolds number $Re \equiv U_i s/\nu$, where s (= 50.73mm) is the disk spacing and U_i is the inlet velocity. In this study, flow condition of Ro = 2.0 and Re = 4000 is considered. The models employed in this simulation are the same as those in radial inflow case.

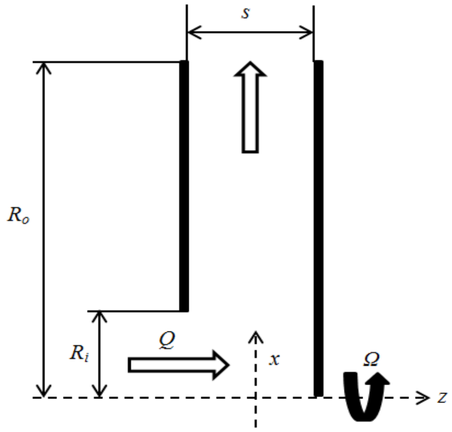

Figure 6.17 Sketch of rotating cavity with radial outflow and axial inflow.

Figure 6.18 shows the radial velocity profile in the boundary layer at two locations. Results predicted by various turbulence models are compared to the experimental data of Owen and Pincombe [42] as well as to the results of RSM [45]. At both positions, none of the models correctly predict the presence of a recirculation cell between the disks. At this relatively high rotation number, RC and Arolla corrections fails to improve the behavior of the RANS models.

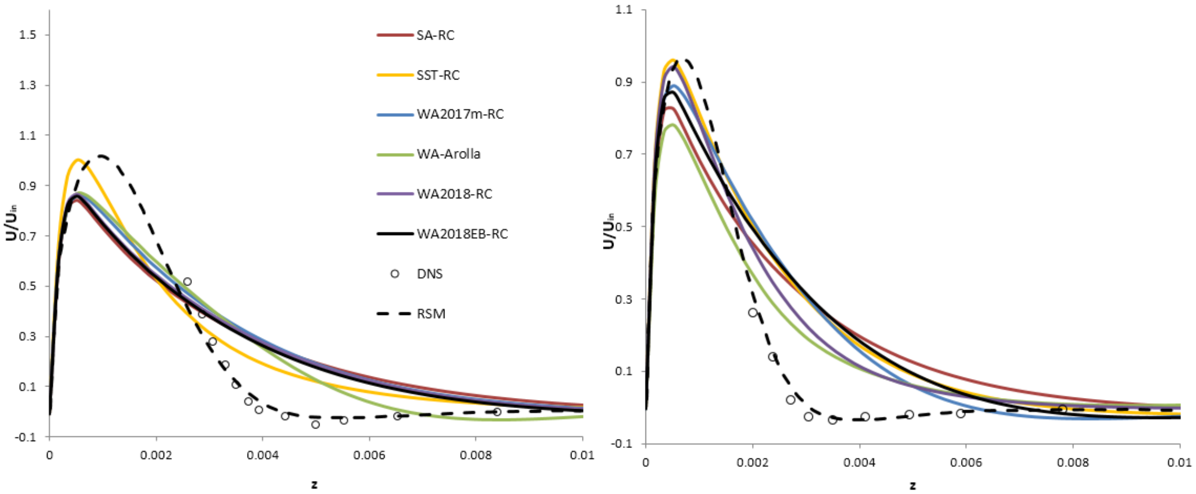

Figure 6.18 Radial velocity profile at x/R₀ = 0.633 and x/R₀ = 0.833.

6.1.6 2D Stationary and Rotating Serpentine Channel

Serpentine channels are found in a number of engineering applications including turbine blade cooling passages. These channels are subjected to strong curvature and rotational effects, and the resulting turbulent flow field is fairly complex. An understanding of the flow physics for flows with strong curvature and rotation is required in order to improve the design of turbine blade cooling passages. The coupled effect of centrifugal forces due to curvature and Coriolis forces due to rotation makes this case very challenging for the turbulence models. Recent DNS data from Laskowski & Durbin [46] is employed for assessing the rotation and curvature correction. The geometry of the serpentine channel is depicted in Fig. 6.19. Station 1 and 5 are at the same "x" location and represent the inflow into U-bend 1 and U-bend 2, respectively. Station 5 is also the exit of U-bend 1. Stations 2 and 6 represent the inflow planes into the bend region corresponding to $\theta = 0^{o}$. Station 3 and 7 are located at $\theta = 90^{o}$ for U-bends 1 and 2. Finally, stations 4 and 8 are located at the exit of the bend section, $\theta = 180^{o}$.The span-wise rotating origin is located at the center of Section 5. The geometry under investigation is $12\pi\delta \times 2\delta$ with a curvature ratio $R_c/\delta = 2$ based on the channel half-width δ. The simulation is carried out at Reynolds number $Re \equiv 2\delta U_b/\nu = 5600$ and rotation number $R_o \equiv 2\delta\Omega/U_b = 0.32$. The inlet and outlet are paired as cyclic to have the stream-wise periodic inflow boundary conditions. A constant pressure source term is added along the stream-wise direction to invoke the flow.

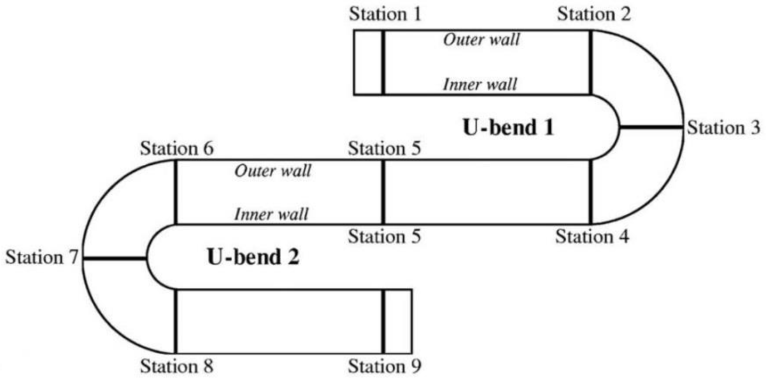

Figure 6.19 Definitions of geometry locations in serpentine channel [46].

In the stationary case, the qualitative trends are predicted well by all the models as shown in the Fig. 6.20. Except at the Station 2, 6 and Station 3, 7, SST-RC predicts a recirculation region near the outer wall, which is not seen in the DNS and other models. Overall, the WA2017m-RC model performs the best among all the models and matches with the DNS results reasonably well. Especially in the first two sections, WA2017m-RC almost duplicates the DNS results. But in the later sections, WA2017m-RC model can only predict the velocity profile trend while underestimates the peak value; while WA2017m-Arolla matches the DNS data quite well. The benefit of applying the RC correction is clearly seen in the first two sections but is not much in the later sections.

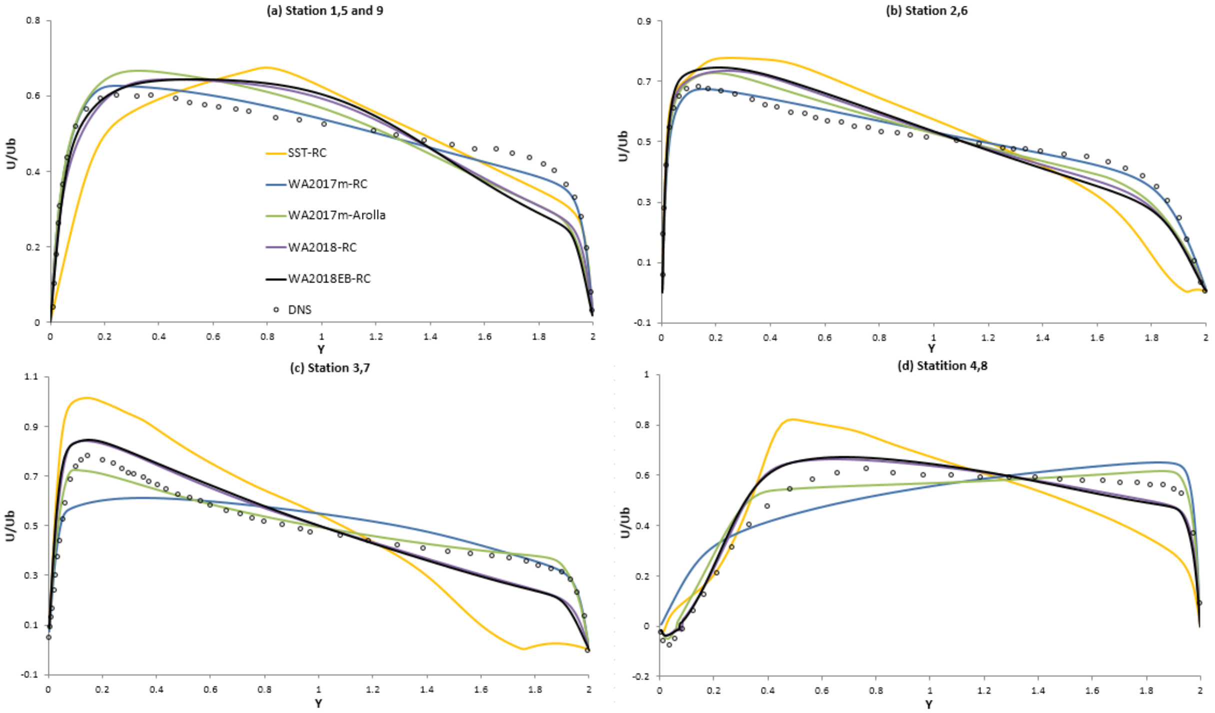

Figure 6.20 Mean velocity profile in stationary serpentine channel.

For the serpentine channel with span-wise rotation, the addition of orthogonal mode rotation results in a strong asymmetry between U-bend 1 and U-bend 2. It is informative to compare the flow field for the stationary and rotating cases at the same station locations for U-bend 1 and U-bend 2. Station 1 is both the entrance of U-bend 1 and the exit of U-bend 2. Thus the flow into U-bend 1 is strongly influenced by the rotation and curvature in U-bend 2. Likewise the flow entering U-bend 2 at station 5 is strongly influenced by the curvature of U-bend 1. This detail is not important in the stationary case but plays a significant role in understanding the rotating case. Flow separation is observed in both U-bend 1 and U-bend 2. RC correction based models over-predict the separation bubble size. Although, DNS data shows very low velocities, it did not quite reach separation in the DNS. The skin friction plot shown in Laskowski & Durbin [46] does suggest that this region is susceptible to separation. WA2017m-RC and WA2017m-Arolla models capture most of the velocity profile trend as shown in Fig. 6.21. While WA2018-RC and WA2018EB-RC both diverge in this case. The reason is still under investigation.

To summarize, the models are not capable of predicting the mean flow for the coupled curvature and rotation effect. Only a qualitative agreement is obtained by WA2017m-RC and WA2017m-Arolla models. Between these two, WA2017m-Arolla is more accurate especially along and after the U-bend 1. This could also be attributed to the fact that DNS is carried out at low Reynolds numbers. Data at high Reynolds numbers is essential to assess the models more rigorously.

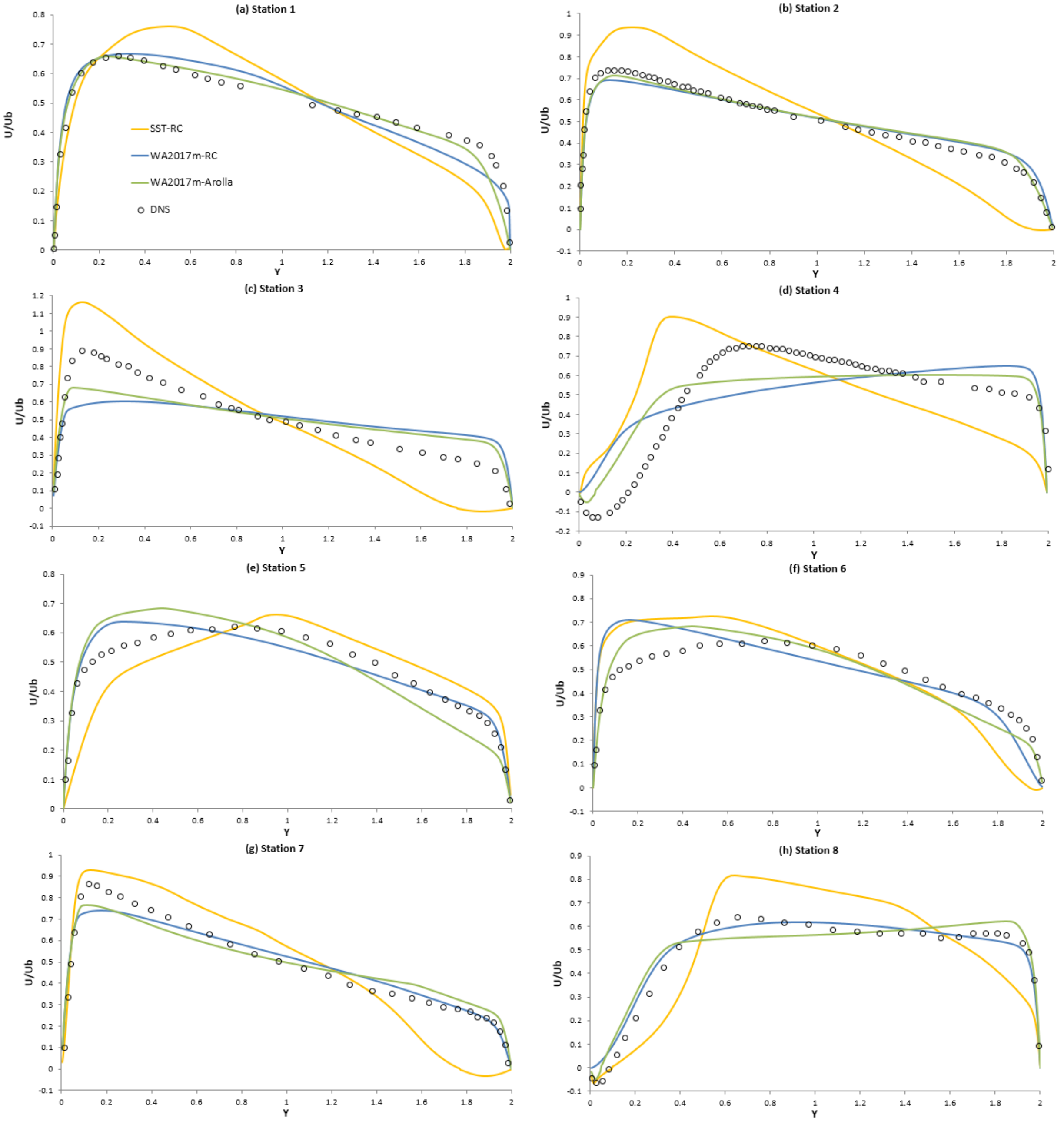

Figure 6.21 Mean velocity profiles in rotating serpentine channel at *Ro* = 0.32.

6.1.7 Rotor-Stator Cavity

The study of the flow in a rotor-stator cavity has significant relevance to many configurations encountered in turbomachinery. There have been many fundamental experimental and theoretical studies [47-49] of the flow in a closed rotor-stator system. In this study, we considered the rotor-stator cavity with a superimposed axial through flow which has been studied experimentally by Poncet et al. [50, 51]. These flows are encountered in many industrial devices such as cooling-air systems in gas turbine engines and have been the subject of intense research during the last several decades as they offer a relatively simple configuration to study the influence of rotation on turbulence.

The cavity sketched in the Fig. 6.22 is composed of two smooth parallel disks of outer radius R_o = 250 mm and inner radius R_i = 38 mm separated by an axial gap h. The rotor is simulated as a rotating wall at a constant rate Ω and the stator is simulated as a stationary wall. A centripetal or centrifugal volume flow rate Q of water can be supplied axially to the cavity through two openings j_h = 17 mm and j_s = 3 mm. Again, since there is no evident three-dimensional structure embedded in the turbulent flow, the numerical domain consists of a 5^{o} sector. All the calculations are conducted on a 300 × 100 mesh in the (r, z) frame. All the variables are set to zero at the walls except for the tangential velocity V_θ, which is set to Ωr on the rotor. At the inlet, a linear profile for the mean tangential velocity V_θ and a parabolic profile for the axial velocity V_z are imposed together with a given low turbulence level of 1%. In the outflow section, the pressure is permanently fixed, whereas all other independent quantities are set to zero gradients if the fluid leaves the cavity.

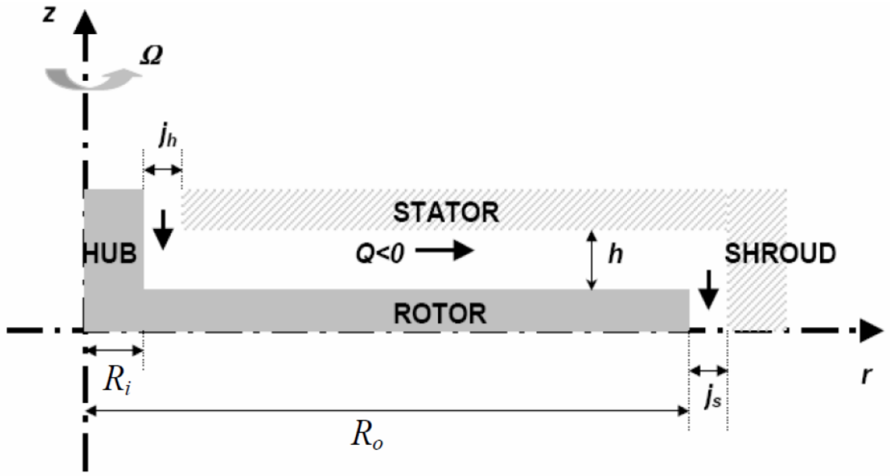

Figure 6.22 Sketch of the rotor-stator cavity with an axial through flow [43].

Different values of the physical parameters are considered which are summarized in Table 6.1. Note that a positive value of the flow rate coefficient C_w corresponds to a centripetal through flow while a negative value of the flow rate coefficient C_w corresponds to a centrifugal through flow. The dimensionless quantities are defined as follows:

$$L = \frac{R_o - R_i}{h} \qquad Re = \frac{\Omega R_o^2}{\nu} \qquad C_w = \frac{Q}{\nu R_o} \tag{99}$$

Table 6.1 Values of the flow parameters for the three cases.

Case	Aspect ratio L	Radius ratio s	Reynolds number Re	Flow rate coefficient C_w
1	23.56	0.152	4.15×10^6	0
2	23.56	0.152	1.04×10^6	9881
3	70.67	0.152	1.04×10^6	-5159

Rotor-Stator with no Through Flow

The first test case is the rotor-stator with no through flow. Simulation results are compared to experimental data [50] and RSM [43]. The flow field is characterized by two boundary layers on each disk, separated by a central inviscid core region. The core is characterized by a zero radial velocity, which ensures that there is no viscous shear stress and by a constant tangential one. The dimensionless quantities are defined as follows:

$$r^* = \frac{r}{R_o} \qquad z^* = \frac{z}{h} \qquad V_r^* = \frac{V_r}{\Omega r} \qquad V_\theta^* = \frac{V_\theta}{\Omega r} \tag{100}$$

An overall good agreement is obtained between the experimental data and the models' predictions for the mean velocity field at the location of $r^* = 0.56$ as shown in the Fig. 6.23. In the core region, all the models predict very similar profile. For the radial velocity profile, WA2017m-Arolla and WA2017m-RC give better agreement near the stator, while the SST-RC and WA2018-RC show good agreement near the rotor. There is negligible difference among the experimental data and the results from all the turbulence models for tangential velocity.

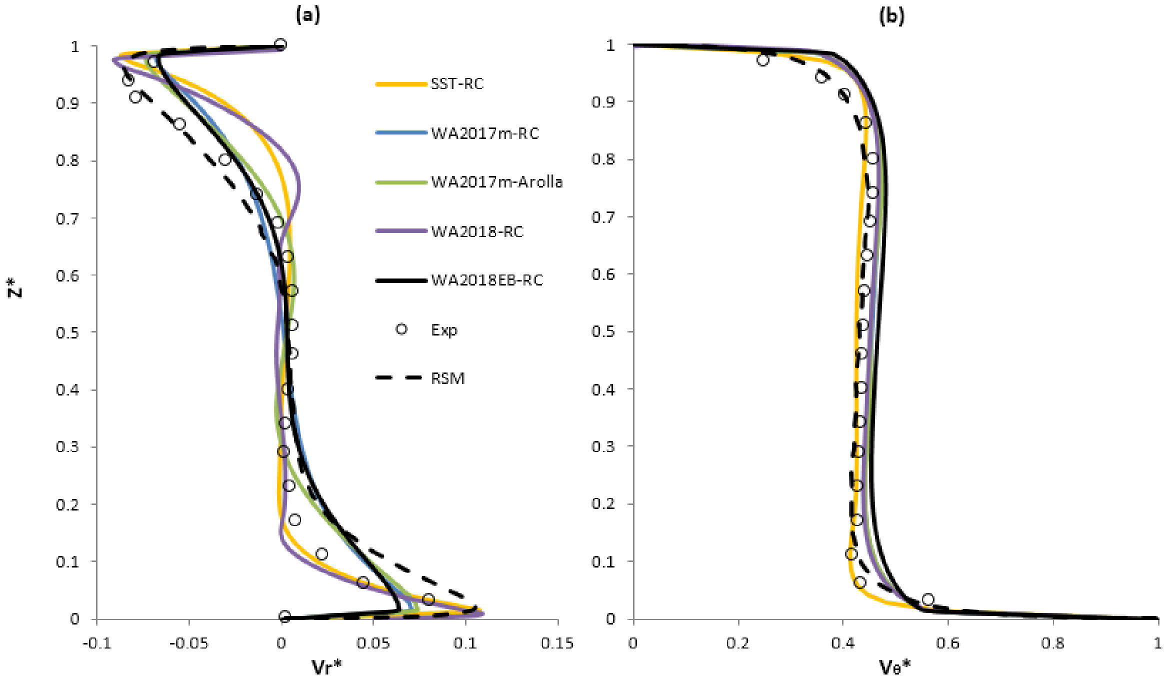

Figure 6.23 Axial profile of the (a) mean radial and (b) tangential velocity components at *r = 0.56.**

Rotor-Stator with Centripetal Through Flow

In this second case, an axial inflow is supplied to the cavity from j_s. The imposed inflow is strong enough to suppress the outflow along the rotor due to the centrifugal force. Hence, the radial velocity is negative at all z^*. None of the model accurately calculates the boundary layer shape seen from the radial velocity profile displayed in Fig. 6.24 (a). Away from the wall, WA2017m-RC is the closest match with the DNS data among all the models. One interesting phenomenon is that the central core region observed in the first test case can rotate faster than the rotor under certain conditions of rotation and imposed flow rate. For the flow condition considered here, the inviscid core is still present at $r^* = 0.56$ but rotates at a higher angular velocity than the rotor which is captured by all the models. However, the SST-RC model predicts a large tangential velocity as shown in Fig. 6.24 (b). This discrepancy may be attributed to different pre-rotation levels imposed at the inlet between the experiment and the simulations. Its value is fixed to half the maximum disk speed in the turbulence models, whereas it slightly varies between 0.5 and 0.55 in the experiments depending on C_w [52].

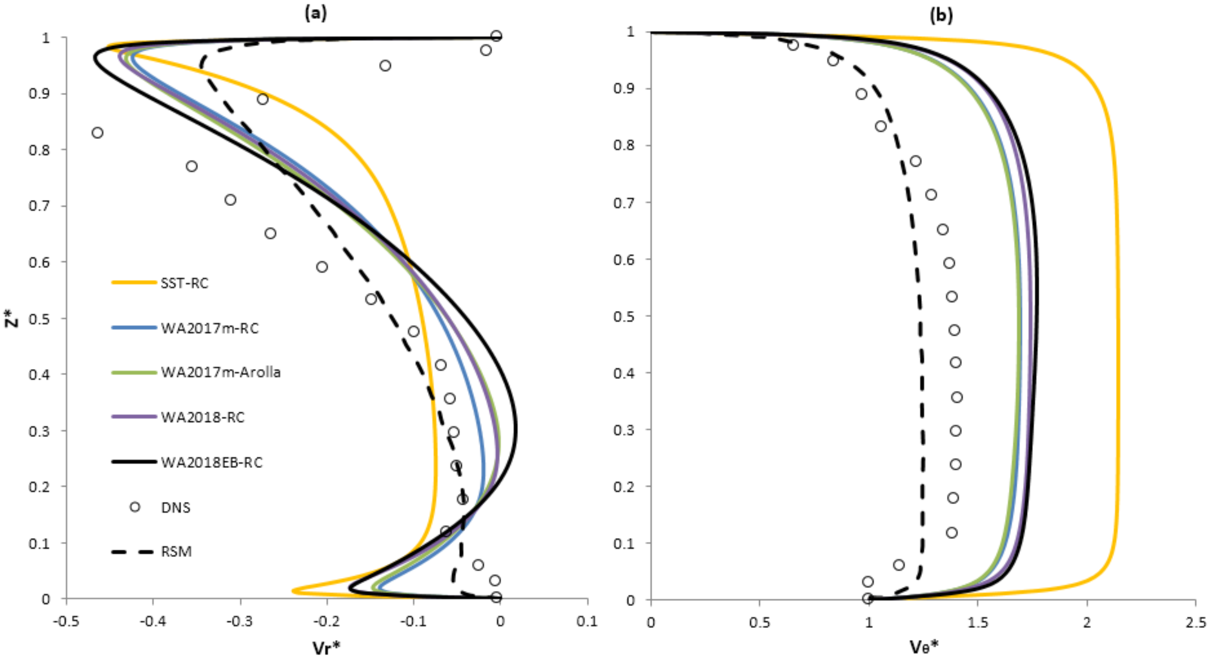

Figure 6.24 Axial profile of the (a) mean radial and (b) tangential velocity components at $r^* = 0.56$.

Rotor-Stator with Centrifugal Through Flow

The last case is the rotor-stator with centrifugal through flow. Figure 6.25 displays the radial and tangential velocity profile at different radial positions. The radial velocity distribution becomes asymmetric at these positions. Even if the flow is outward along the stator, the radial velocity is greater along the rotor due to the combined effect of the centrifugal force. There is little variance among various versions of WA models with RC and Arolla corrections. For the radial profile, the SST-RC and WA based models behave differently at early position $r^* = 0.44$, and results from WA based models are closer to the RSM results. At later positions $r^* = 0.68$ and $r^* = 0.92$, all the models are close to each other and match with the RSM results. For the tangential velocity, the SST-RC model performs slightly better than the WA based models.

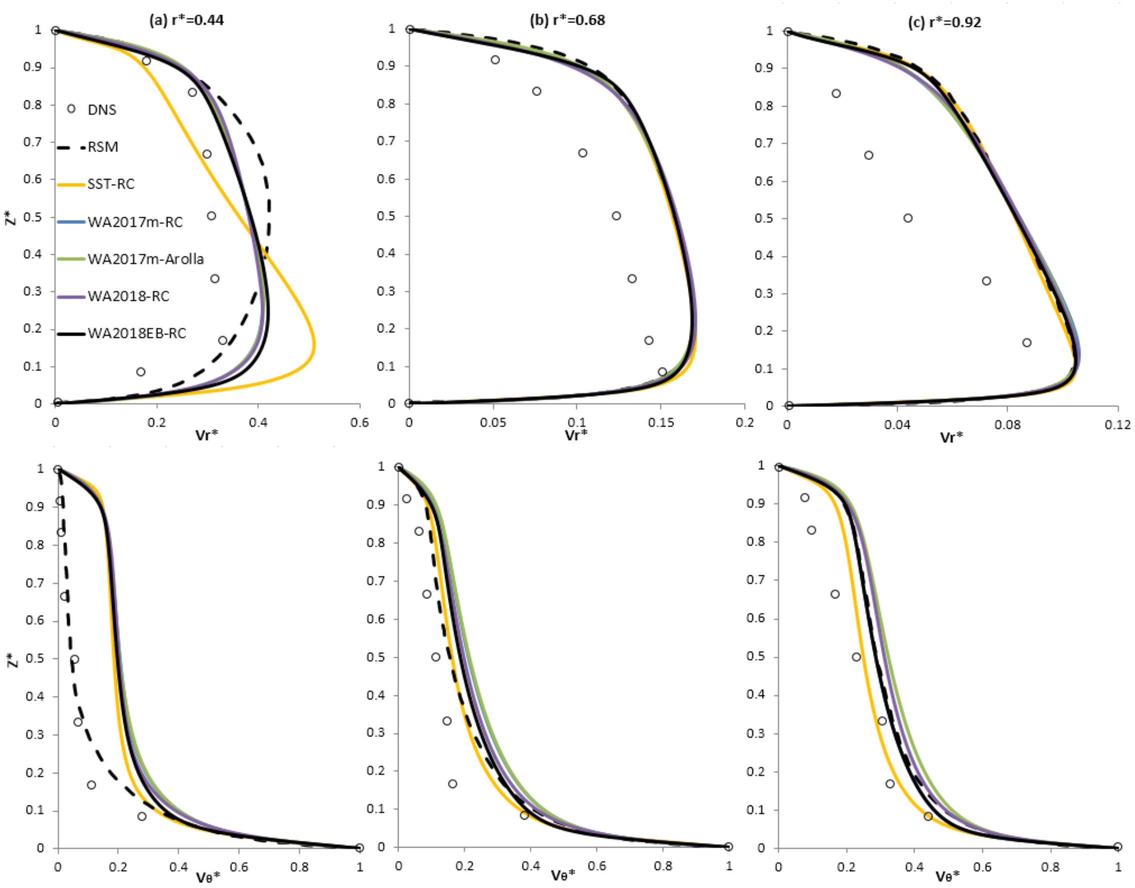

Figure 6.25 Axial profile of the mean radial and tangential velocity components at three positions.

6.1.8 Hydrocyclone

The cyclone separator is perhaps the most widely used separation device to be found in industry. It owes its popularity to the low manufacturing and maintenance costs due to its simple design. There are no moving parts in the device itself, which can be constructed from a wide range of materials. Combined with ideal pressure drop and a range of throughputs and efficiencies, these advantages have made the cyclone the most attractive solution to separation in both solid-gas and liquid-solid systems. Cyclones can be distinguished from other separation devices by noting that the centrifugal forces caused by the swirling motion of the flow in a cyclone results in separation. The experimental cyclone configuration is depicted in Fig. 6.26 which is a typical high-efficiency cyclone designed by Stairmand [53]; it has a diameter $D = 0.205$ m. The volume of the cyclone is 0.0203 m^3. A relatively fine grid is used with approximately 560,000 cells in all calculations.

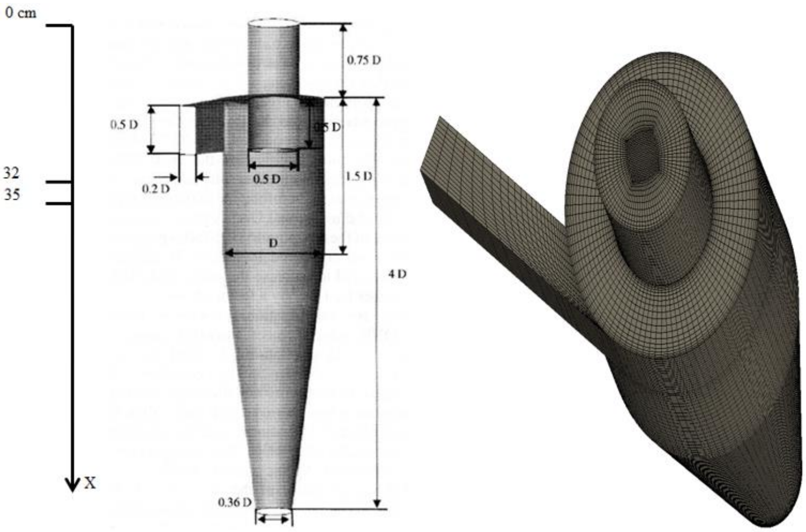

Figure 6.26 Geometry [53] and mesh of the Stairmand cyclone.

Flow through the hydrocyclone is characterized by strongly swirling motion as shown in Fig. 6.27. The path lines are calculated by RSM in Fluent 14.5. Swirl induced suppression of the turbulence at the core of the hydrocyclone cannot be predicted by the scalar eddy viscosity closure, which motivates the use of rotation and curvature correction for this case. The RC corrected SST and various WA models as well as WA2017m-Arolla are employed to conduct the steady state simulations.

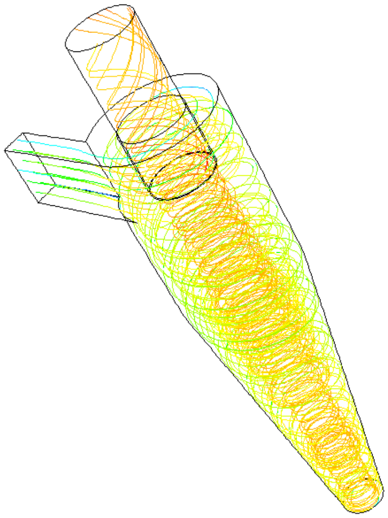

Figure 6.27 Path lines colored by velocity showing the strongly swirling flow in hydrocyclone.

Predicted radial and axial velocity at the axial stations x = 0.32 m and 0.35 m are compared with the experimental data [54] and RSM as shown in Fig. 6.28. The original scalar viscosity models (SST, WA2017m) are not able to predict the downward flow in the core region. When RC and Arolla corrections are added, the flow direction is correctly predicted in the first location, which is very critical in the design of the hydrocyclones since it determines the separation efficiency of these devices. In general, the agreement between the models and experimental data is not good. SST-RC, WA2017m-RC and WA2017m-Arolla models satisfactorily calculate the shape of the axial velocity profile, but for the radial velocity they can only estimate the profile around the core region and fail to capture the velocity drop when leaving the core region. Even though the RC and Arolla corrections enable the SST and WA2017m models to predict the downward flow at the core, the models do not match the experimental data to a large degree especially at later locations. There are several more locations where the simulation results were obtained and compared with experiment, but since the agreement was very poor, the results are not presented here. Obviously among all the models employed, the RSM is the only turbulence model that provides reasonably good prediction for this complex case.

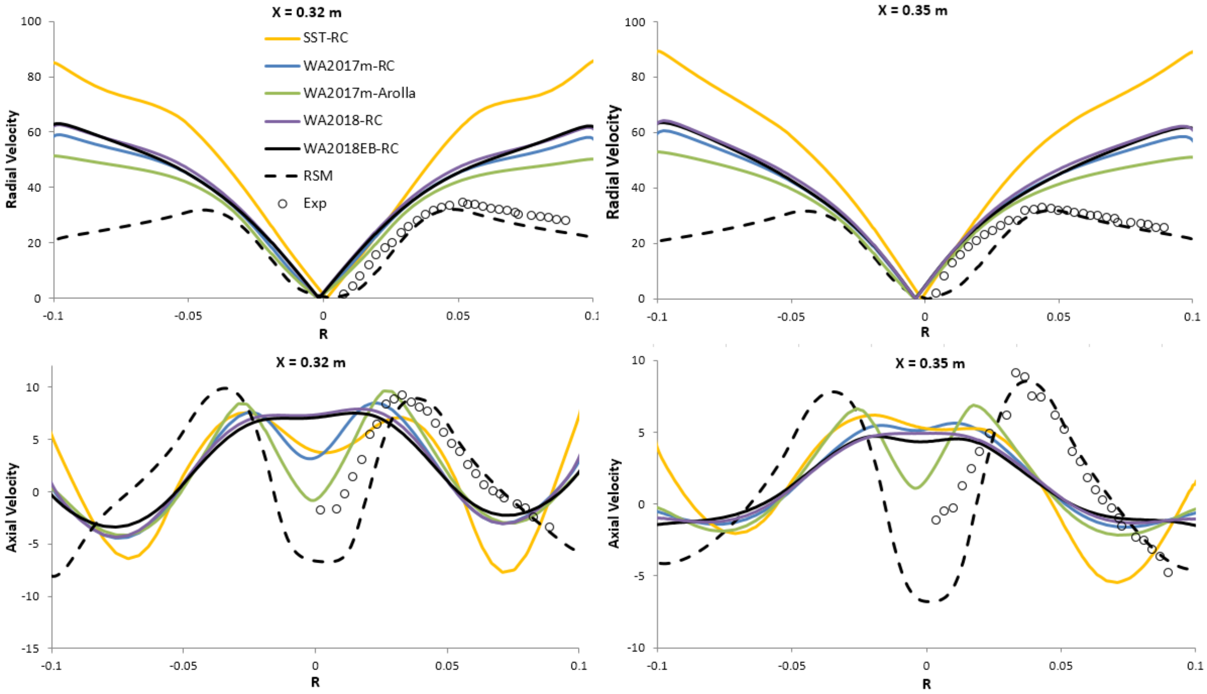

Figure 6.28 Radial profile of axial and radial velocity at two positions.

6.2 Unbounded Flows

Unbounded flows also known as the free shear flows are inhomogeneous flows with mean velocity gradients that develop in the absence of boundaries. Free shear flows in the real world are most often turbulent. Even if they start as laminar flows, they tend to become turbulent much more rapidly than wall bounded flows. This is due to the fact that the three-dimensional vorticity necessary for transition to turbulence can develop much more rapidly in the absence of wall that inhibits the growth of velocity components normal to the wall.

All the test cases presented in section 6.1 are for wall bounded flows and the model coefficients of all the turbulence models were calibrated for wall bounded flows. Even though it is not expected that the rotation and curvature corrections developed for turbulence models for wall bounded flows would be able to capture all the important features of unbounded shear flows; they are nevertheless tested for computing two test cases of a circular jet in subsonic crossflow and a supersonic jet in subsonic crossflow.

6.2.1 Circular Jet in Subsonic Cross Flow

The flow field of a jet of fluid interacting with a crossflowing fluid is defined as a jet in crossflow. Some examples of jets in crossflow are fuel injectors, smokestacks, film cooling on turbine blades and dilution holes in gas turbine combustors.

Muppidi and Mahesh [55] conducted the DNS of a round turbulent jet in crossflow and provided some insight on why the typical RANS models fail to predict this flow accurately. The jet flow interacts with the crossflow and undergoes a significant curvature which is the motivation to examine how the rotation and curvature correction to RANS models would improve their performance in predicting such flows. A mean flow field solution of the time-averaged behavior of a transverse jet is provided in Fig. 6.29, which shows results from DNS of Muppidi and Mahesh [55]. The contours of mean velocity show that the jet fluid bends towards the free stream crossflow direction and the width grows as it moves downstream. It is worth noting that the jet width is larger towards the leeward side than on the windward side of the centerline of the jet. Moreover, the cross section of the jet evolves from its circular shape to form a counter-rotating vortex pair (CVP). The local mean vorticity is maximum at the CVP center, which lies below the centerline.

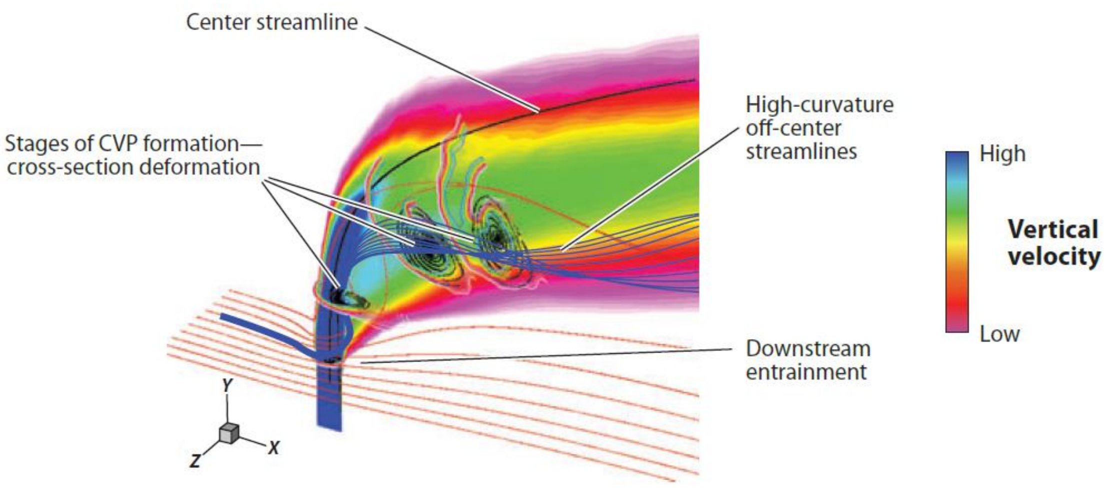

Figure 6.29 The mean flow field of an incompressible transverse jet [55].

We follow the same computational setup as in DNS of Muppidi and Mahesh [55]. Figure 6.30 shows a schematic diagram of the problem, where a jet issues in perpendicular direction from a round pipe (diameter d) into the crossflow. The crossflow is in the x-direction and the jet is in the y-direction. The origin is located at the center of the jet exit as shown in the figure. The velocity ratio is defined as $r = \overline{u}_j/u_\infty$, where $\overline{u}_j$ is the mean jet velocity obtained by averaging u_j over the pipe cross-section and u_∞ is the crossflow free stream velocity. Simulations are performed at the same flow conditions as in the experiment of Su and Mungal [56]. The velocity ratio (r) is 5.7 and the Reynolds number of the flow based on the bulk jet velocity and jet-exit diameter, is 5000. In the experiment, the jet exits out of a round pipe ($\sim 70d$ long) into the crossflow. Fully developed pipe flow conditions are reached at the jet exit (Su and Mungal). The experiment considered two scenarios: one where the jet exit was flushed with the wall and the other where the pipe protruded into the crossflow. The DNS [55] and present simulations are confined to the case of the jet exit flushed with the wall, as shown in the Fig. 6.30.

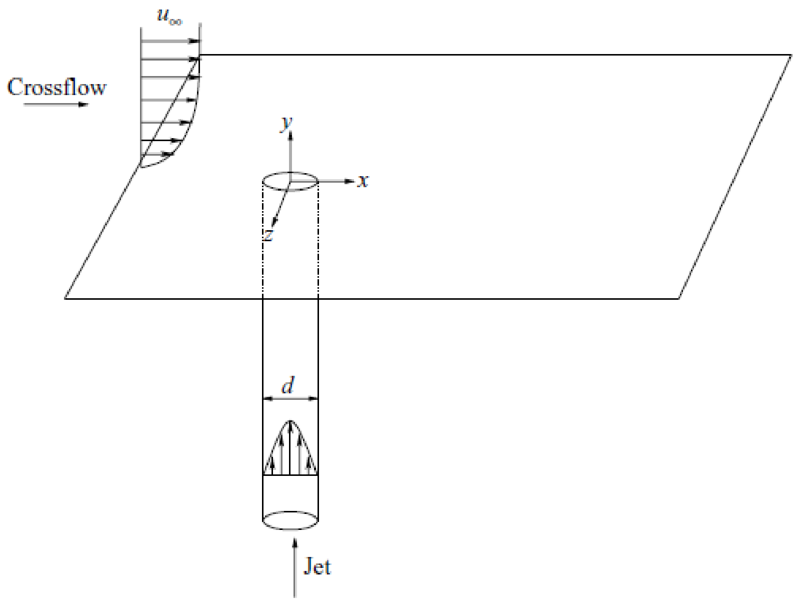

Figure 6.30 Schematic of the round turbulent jet in cross flow [55].

The computation domain extends $36d \times 64d \times 64d$ in the axial, wall-normal and span-wise directions (x, y and z) respectively as shown in the Fig. 6.31 (a). Fully developed turbulent flow field is injected from both crossflow inlet and jet inlet. The length of pipe is $2d$ and the crossflow inflow plane is located $4d$ upstream of the jet exit. Su and Mungal [56] have reported that the jet bulk velocity ($\overline{u}_j$) in their experiment is 16.9 m/s and the free stream crossflow velocity (u_∞) is 2.95 m/s, which gives a velocity ratio ($r = \overline{u}_j/u_\infty$) of 5.7. The velocity ratio in the simulation is also 5.7. The Reynolds number based on the bulk jet velocity and jet exit diameter is 5000 which matches with the experiment. Note that in the simulation it is assumed that both the jet fluid and the free stream crossflow fluid have the same density. However, in the experiment, the jet fluid (nitrogen) is seeded with acetone vapor which gives the jet fluid a 10% higher density. Since it is an incompressible case, the density difference has no effect on the final results.

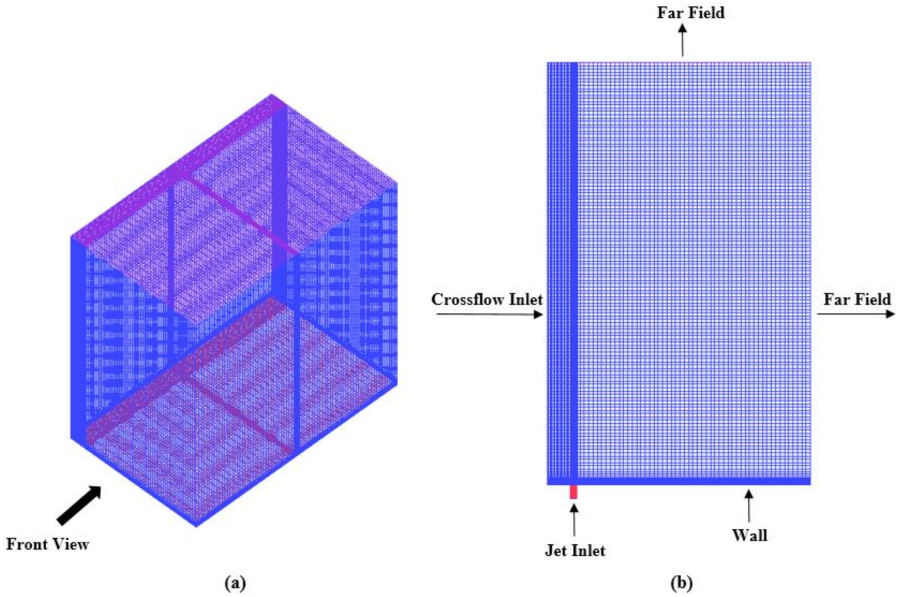

Figure 6.31 (a) Computational domain and (b) front view of the mesh with boundary types.

Figure 6.32 compares profile of vertical velocity U_y between the simulation and experiment. The circle symbols are the results from the Su and Mungal's experiment [56], doted lines are from DNS results [55], dash lines are Reynolds Stress Model (RSM) results and colored lines are results obtained using various models with rotation and curvature corrections. Close to the jet exit ($y = 0.1rd$), the jet shows characteristics similar to that of turbulent flow in a pipe, velocity profile appears to be symmetric about $x = 0$. One difference from a turbulent pipe flow profile is a small negative velocity U_y upstream of the jet (peak negative velocity is observed at $x \sim -0.1rd$). The crossflow fluid regards the jet as an obstacle, resulting in a high-pressure region upstream of the jet. This pressure gradient forces crossflow fluid towards the jet exit (the crossflow fluid even enters the pipe at sufficiently small velocity ratio), giving rise to the negative U_y as observed. This behavior is also successfully captured by all the RANS models and RSM, but they underestimate the peak velocity and predict a flat profile at the center of the pipe. On the downstream of the jet except WA2018EB-RC, the rest of models computes a rather large region of negative velocity region compared to the upstream, which is not seen from the experiment and DNS data.

Moving away from the jet exit, the velocity profiles lose symmetry. According to the experiment and DNS results, at the farthest station (*y* = 1.0*rd*), velocity profile appears to be composed of two distinct jets, one with a higher velocity (centered at *x* = 0.1*rd*) followed by another with lower velocity (centered at *x* = 0.38*rd*). It is because the jet fluid on the side of the jet is deposited on the symmetry plane downstream of the jet, and this jet fluid possesses a vertical velocity and results in a "two-jet" profile as observed. However, at earlier position (*y* = 0.5*rd*), all the models have already predicted the "second jet" at *x* = 0.28*rd*, so the overall velocity profile is underestimated for the "first jet." Furthermore, this leads to the result that all models have a complete mismatch with the experiment and DNS data at the farthest station (*y* = 1.0*rd*).

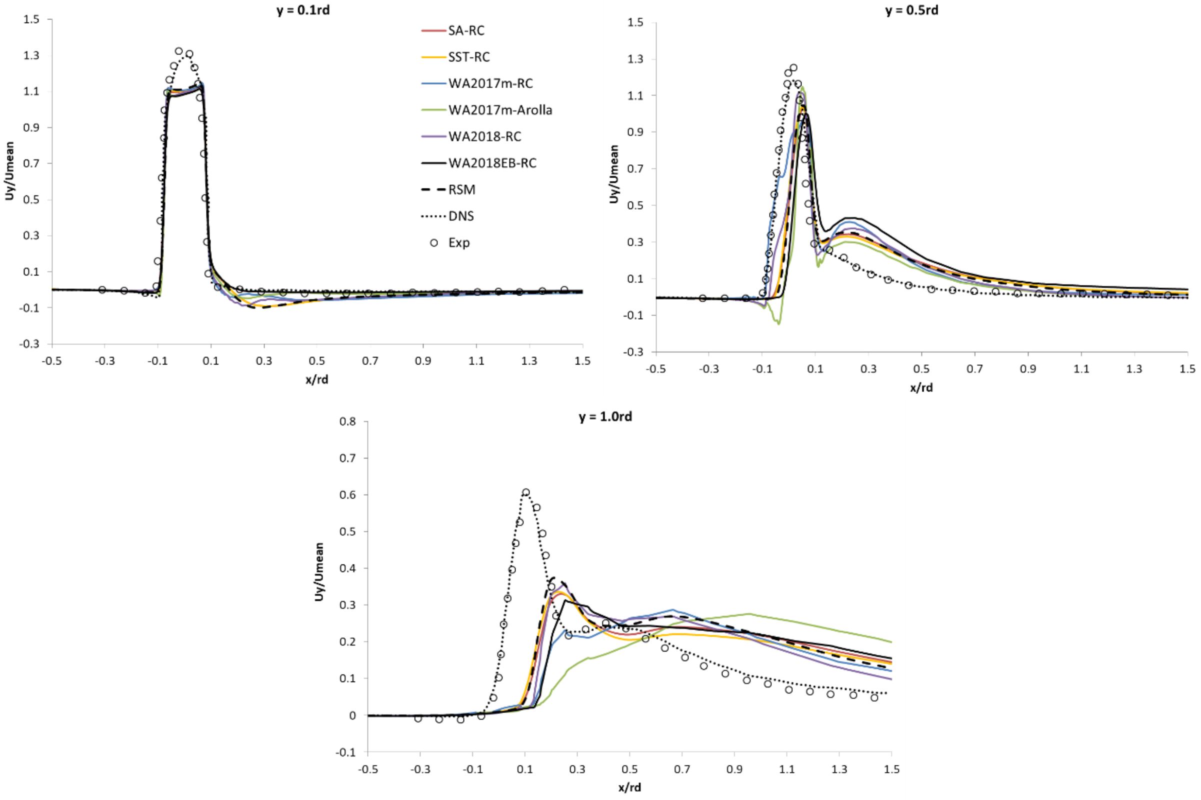

Figure 6.32 Vertical velocity profiles at three locations.

It has been mentioned by Muppidi and Mahesh [55] that this flow field is far from being in turbulent equilibrium, in particular near the jet exit and in the near field. Also, the flow field is three-dimensional and non-isotropic. Even with rotation and curvature corrections, the RANS models are not able to accurately compute the velocity profiles. Reynolds Stress Model (RSM) is expected to account for anisotropy in the flow but in this case it also fails. In most RSM, the transport of turbulent kinetic energy by pressure (π_{ii}) is either ignored or modeled. In simple wall bounded flows, π_{ii} is identically zero near the walls and fairly small across the computational domain. However, in a jet in crossflow, π_{ii} is not negligible. Another source of uncertainty in RANS modeling of jet in crossflow comes from the computation grid and the domain. Since the profiles involve steep gradients at the jet edges, rather high resolution mesh is required to guarantee an accurate solution in this region. In our study, a refined mesh is applied in these regions, but still may not be fine enough.

6.2.2 Glenn Jet: Supersonic Jet in Subsonic Cross Flow

After examining a subsonic jet in crossflow, it is interesting to see how the turbulence models perform in case of interaction of a supersonic jet in the subsonic crossflow. The Glenn jet experiment (Wernet et al. [57]), conducted at the NASA Glenn Research Center, was designed to obtain data for a hot supersonic jet in subsonic crossflow. The experiment was conducted at the highest possible pressures and temperatures attainable in the test facility, with a stagnation pressure and temperature of 2.8×10^6 Pa and 750 K, respectively. The nozzle was placed in a wind tunnel with cold free stream air at Mach 0.3. The jet air was heated using a natural gas combustor and exhausted through the conical nozzle at an angle of 25 degrees relative to the freestream. The nozzle exit design Mach number was 3.0, but due to the under-expansion, Mach numbers exceeding 4.0 were seen downstream.

The simulation follows the same setup as in the experiment. The computational domain includes the entire wind tunnel. Particular attention is paid to ensure sufficient resolution along the nozzle lip and the mixing region. The side part comprises 9 blocks and the nozzle part comprises 36 blocks. The whole computation domain involves a total 7×10^6 grid points. Figure 6.33 shows the grid for the Glenn jet and a zoomed-in region of nozzle. The jet inlet and outlet are treated as pressure inlet and outlet, and free stream inlet and side part are treated as pressure far field.

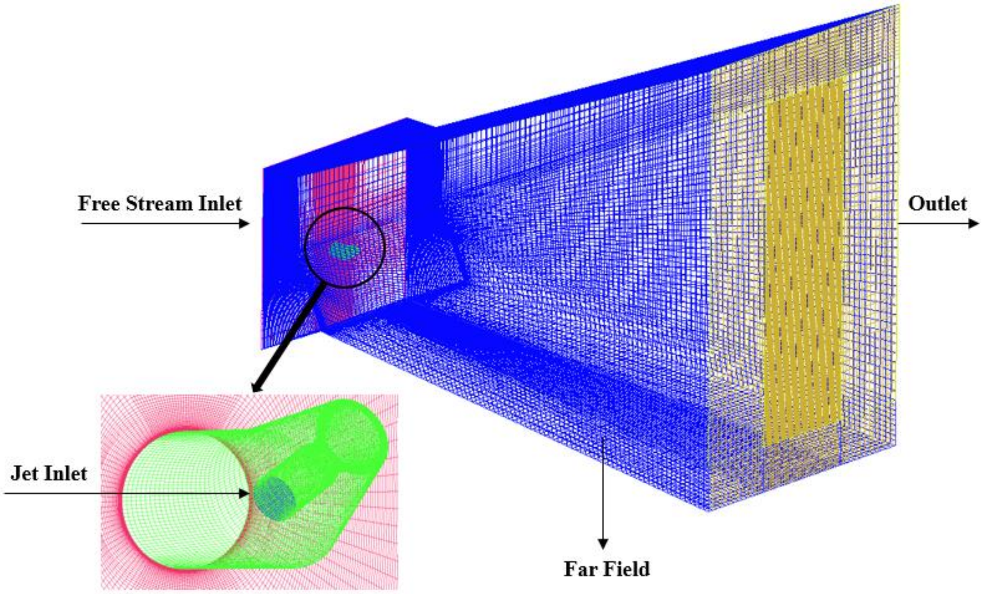

Figure 6.33 Computational domain of the Glenn jet.

Comparisons are made for the Glenn jet with crossflow. Downstream of the jet, four locations perpendicular to the freestream, normalized by the jet exit diameter are of interest as indicated in Fig. 6.34. The four locations are at X/D = 6, X/D = 10.5, X/D = 14 and X/D = 18. To make the comparisons easier to see, "①" is referred to the upside of the jet downstream and "②" is referred to the downside of the jet.

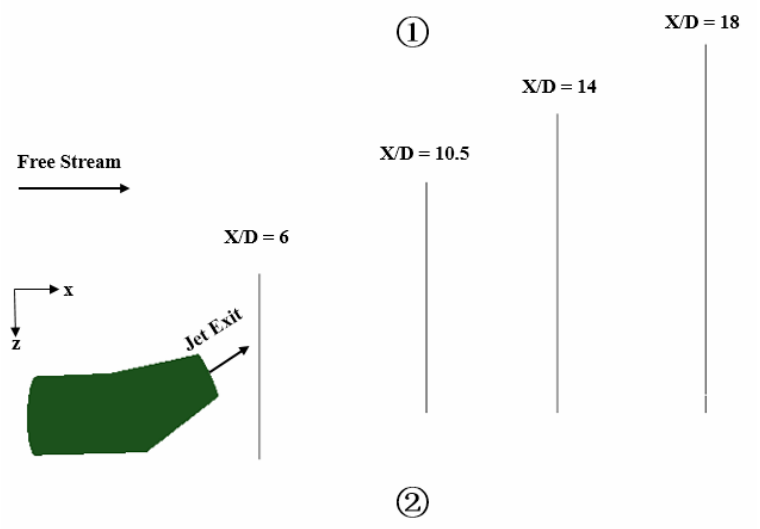

Figure 6.34 Sketch of four jet locations downstream.

Figure 6.35 shows the velocity magnitude normalized by the velocity of jet exit center at those four downstream locations, and compared with PIV data. At the first location X/D = 6, the velocity profile remains almost symmetrical and at the center region of the jet it shows a flat trend. These behaviors are successfully captured by all the three models (SA-RC, SST-RC and WA2017m-RC) in this case. But overall the simulation results predict a wider profile compared to the experimental data. More interestingly, all three models predict a "second stage" on both side of the flat region which is not seen in the experimental data. Moving farther downstream, the velocity profile lose the symmetry. At the second location X/D = 10.5, all the three models results show a downward trend in the center which have mismatch with the experiment data. The agreement between the simulation and experiment is better on the "①" side than the "②" side. According to the experimental data, the mixing of jet fluid and freestream is enhanced on the "①" side while suppressed on the "②" side. This is due to the 25 degree crossflow interaction with the jet. Even with RC correction, the models are not able to predict it accurately. At the third location X/D = 14, WA2017m-RC model exhibits a "two-jet" like profile as in the previous case of subsonic jet in crossflow in section 6.2.1 which is not predicted by the other two models (SA-RC and SST-RC) and experimental data. At the final location X/D = 18, the velocity magnitude calculated by SA-RC and WA2017m-RC is too high because turbulent mixing in the shear layer is suppressed for too long. A potential reason for this behavior, when compared with the subsonic jet with crossflow, is that the current experiment is performed at much higher turbulent Mach numbers than in the previous case. The compressibility effect is dominant in this problem which is expected because of the high Mach numbers in the jet shear layer.

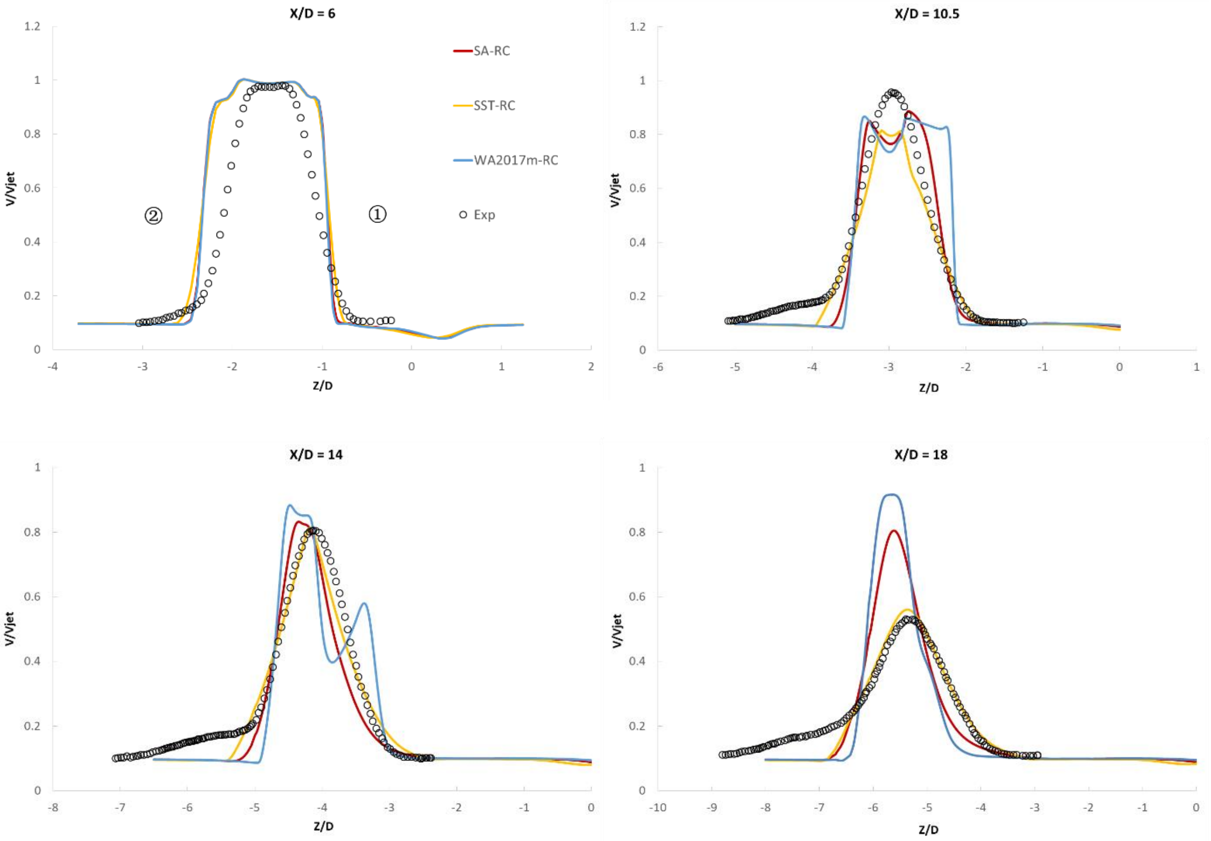

Figure 6.35 Velocity profiles at four jet downstream locations.

The current turbulence models have been designed and developed for low-speed and isothermal flows. For higher Mach number flows, the effect of compressibility on the dissipation rate of the turbulent kinetic energy need to be addressed. For free shear flows, this is exhibited as the decrease in growth rate in the mixing layer with increasing Mach number. Standard turbulence models do not account for this Mach number dependence, and thus a compressibility correction is needed for this case. Also mentioned by Abdol-Hamid et al. [58] that standard turbulence models fail to capture the increase in growth rate of the mixing layer due to temperature effects observed by Seiner and Thomas [59, 60] in their experiment. A new correction was developed to deal with the temperature effect. But those corrections are not within the scope of this thesis. RC correction seems to have little effect on the model behavior.

6.3 Summary of Models Performance

This section summarizes all the WA based models' performance for each test case as shown in Table 6.2. The points from "4" to "1" are given based on their agreement compared to experiment or DNS data. "4" represents the best while "1" represents the worst. If the models perform equally, then they are given the same point. The summation of points indicates the overall behavior of each individual model. WA2017m-RCM is only validated in the 2D curved duct case and fails when system rotation is enforced, so it is not included in the summary. Note that for rotating backward-facing step all the models fail to match with the DNS data, so all of them are given "1" point. Due to the same reason, the two unbounded flow cases are not included in the summary. As we can see, WA2017m-RC scores the highest "37" points and WA2017m-Arolla is the second best scoring "33" points. WA2018-RC and WA2018EB-RC obtain "21" and "22" points respectively. It can be concluded that WA2017m-RC is the most accurate model among all the validation cases in this study; and it is also safe to say that WA2017m-RC should give reasonable prediction in other cases with system rotation and streamline curvature.

Table 6.2 Summary of models behavior in each case.

Test Case	WA2017m-RC	WA2017m-Arolla	WA2018-RC	WA2018EB-RC
Curved Duct	3	2	1	4
U-duct	4	3	1	2
2D Rotating Channel	4	1	2	3
Rotating Backward-facing Step	1	1	1	1
Rotating Cavity - Radial Inlet	4	3	2	1
Rotating Cavity - Axial Inlet	2	4	3	1
Stationary Serpentine Channel	3	4	1	2
Rotating Serpentine Channel	3	4	NA	NA
Rotor Stator - Nothrough Flow	3	4	1	2
Rotor Stator - Centripetal Flow	4	2	3	1
Rotor Stator - Centrifugal Flow	2	2	4	4
Hydrocyclone	3	4	1	2
Sum	37	33	21	22

Chapter 7: Detached Eddy Simulation (DES)

7.1 Introduction

Due to high computational cost, the Large Eddy Simulation (LES) although being more accurate than RANS simulation is currently not used routinely for complex industrial applications. RANS simulations are widely used in industry in conjunction with a turbulence model which introduces inaccuracies especially in wall bounded flows with separation. To address the high simulation cost of LES and low accuracy associated with RANS simulations, hybrid RANS/LES models have been developed in past couple of decades. These are often referred to as the Detached Eddy Simulation (DES) models. In the hybrid model, near wall region of a boundary layer is simulated by RANS while the flow field away from the wall region is simulated by LES. Thus DES takes advantage of the efficiency of RANS and the accuracy of LES to achieve more accurate and efficient calculation of the turbulent flow field. DES type of hybrid modeling was first proposed by Spalart [61].

In 2017, Han et al. [62] successfully developed a DES model based on Wray-Agarwal (WA) turbulence model and showed better agreement between the experimental data and the DES results for several benchmark test cases compared to the RANS simulations with WA and other widely used turbulence models namely the Spalart-Allmaras (SA) and SST k-ω models. In previous chapter, Rotation and Curvature correction (RC) was applied to various versions of WA model to account for the frame rotation and streamline curvature. To author's knowledge, in literature DES has never been applied to flows with RC correction. In this chapter, a new DES model is developed based on the Wray-Agarwal model with RC correction and is designated as WA2017m-RC-DES.

The new model is validated against experiment data and DNS results for test cases from Chapter 6.

7.2 WA2017m-RC-DES Model

The transport equation of WA2017m-RC-DES model is shown in Eq. (101). The term f_{r1} is the Spalart-Shur rotation and curvature function [17], which is described in Chapter 4. It is multiplied by the production term C_1RS.

$$\frac{\partial R}{\partial t}+\frac{\partial u_jR}{\partial x_j}=\frac{\partial}{\partial x_j}\left[(\sigma_R R+\nu)\frac{\partial R}{\partial x_j}\right]+f_{r1}C_1RS+f_1C_{2k\omega}\frac{R}{F_{DES}^2S}\frac{\partial R}{\partial x_j}\frac{\partial S}{\partial x_j}-(1-f_1)C_{2k\varepsilon}\frac{E_R}{F_{DES}^2} \tag{101}$$

Characteristic length scale ratio F_{DES} in Eq. (101) is defined similar to that in the SST k-ω DES model [63], in which a new constant C_{DES} is introduced. When F_{DES} is equal to 1, the model returns to RANS model, otherwise it behave likes the LES model.

$$\begin{gathered} F_{DES}=\max\left(\frac{l_{RANS}}{l_{LES}},1\right) \\ l_{RANS}=\sqrt{\frac{R}{S}} \\ l_{LES}=C_{DES}max\left(\Delta_x,\Delta_y,\Delta_z\right) \end{gathered} \tag{102}$$

The constant C_{DES} is calibrated by the decaying isotropic turbulence (DIT) test case and the final value is fixed at 0.41 [62]. The switch function and other coefficients constants are kept the same as in WA2017m model.

7.3 Validation Cases

7.3.1 Curved Duct

This case was modeled as 2D in the previous RANS simulation by WA2017m-RC model. However, the DES requires full 3D modeling and the use of transient solver in OpenFOAM. Note that there is only one layer in the third direction, and "front" and "back" side of the mesh in the third direction are treated as periodic boundaries. All the DES simulations reported in this chapter are performed following this approach.

The DES model is very sensitive to the mesh density; it switches between the RANS region and the LES region according to Eq. (102). The mesh independent study was conducted for this case using meshes of different densities as summarized in Table 7.1. In general, the finer grid covers larger LES region in DES.

Table 7.1 Densities of three meshes employed.

Grid Type	Size
Coarse	$257 \times 97 \times 2$
Medium	$513 \times 193 \times 2$
Fine	$1025 \times 385 \times 2$

Figure 7.1 shows the computed and experimental pressure coefficients along the convex wall of the duct. The results from three different density meshes differ a lot in the upstream and downstream regions of the curved duct. From Fig. 7.1, it can be noted that the medium size mesh matches with the experiment data best and also gives result in agreement with that obtained with WA2017m-RC model. Comparisons of the calculated and experimental skin friction coefficients

are shown in Fig. 7.2. Again, the mesh size shows significant influence on the results. However, in this figure, the largest difference occurs in the middle of the curved part of the duct.

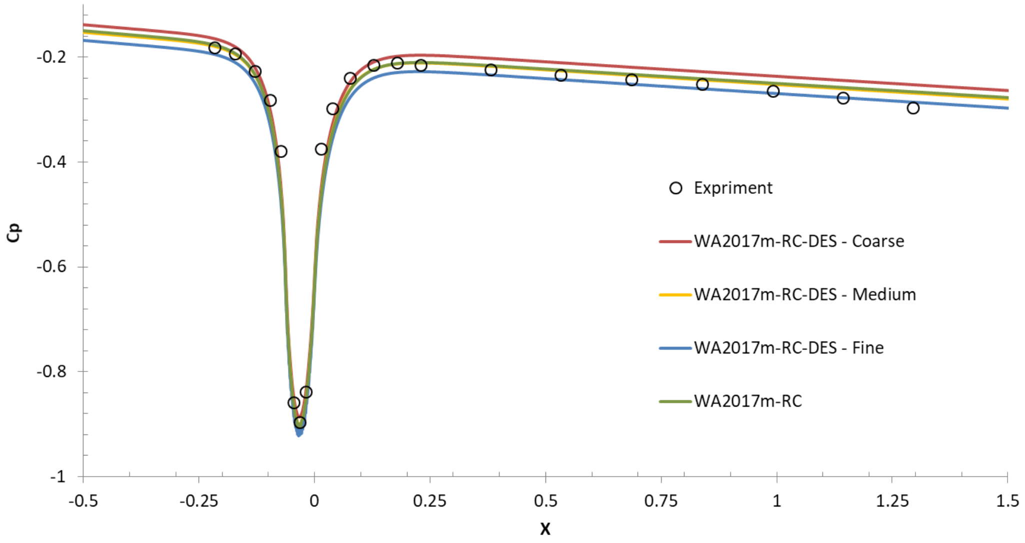

Figure 7.1 Comparison of pressure coefficient along the convex wall of the curved duct.

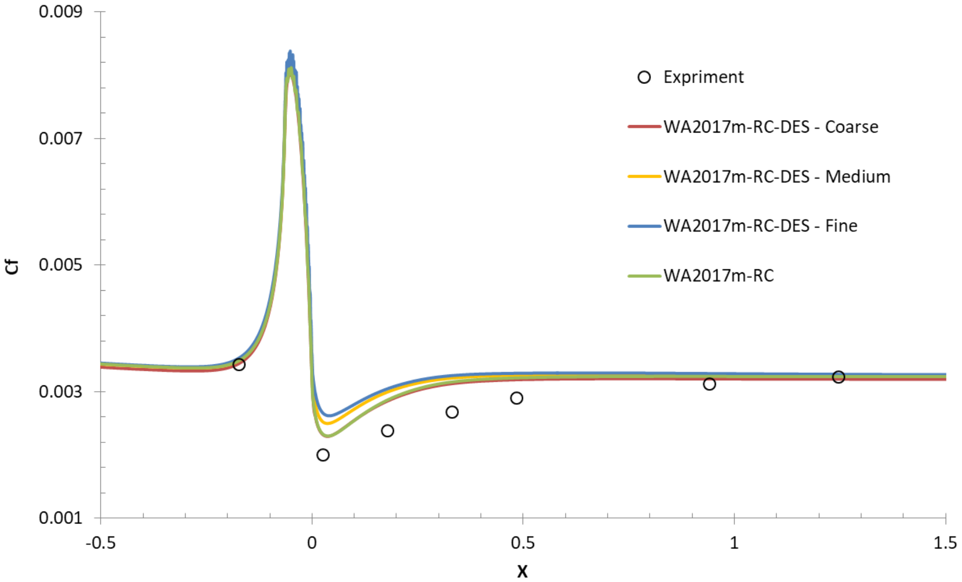

Figure 7.2 Comparison of skin friction coefficient along the convex wall of the curved duct.

Figure 7.3 shows the comparison of velocity profiles at five locations downstream (x = 0.030 m, 0.183 m, 0.335 m, 0.635 m, and 1.250 m). The velocity is less sensitive to the mesh size, and the locations of interest are in the downstream region; therefore the DES results from three types of meshes have little difference. For clarity, only one curve of WA2017m-RC-DES is plotted in the figure. WA2017m-RC-DES model shows close agreement with the experiment data, especially at the first location (x = 0.030 m), where other models (SA-RC, SST-RC and WA2017m-RC) do not match with the experimental data. In the near wall region, WA2017m-RC-DES also performs quite well compared to the other RANS models.

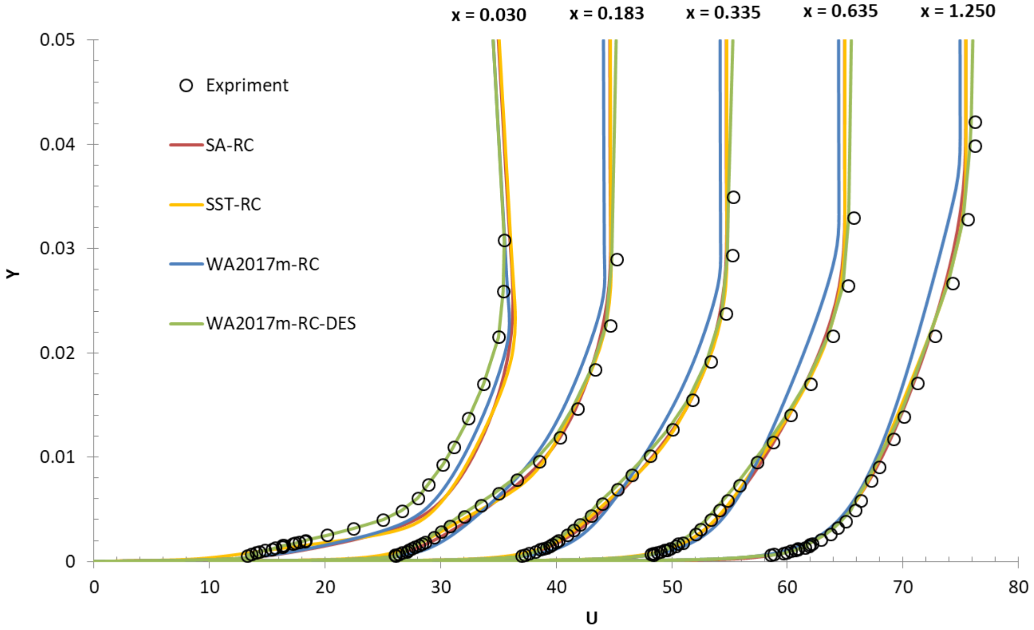

Figure 7.3 Comparison of velocity profile at downstream locations in the curved duct.

7.3.2 U-turn Duct

Large improvements have been obtained by adding RC to eddy viscosity models [4, 5]. The results of WA2017m-RC-DES model are compared with experimental data, the Reynolds Stress Model (RSM) [35] and also with other RANS models with RC. The flow conditions correspond to the experiment of Monson et al. [34]. The Reynolds number of the flow is Re = 10^6 based on the mean flow velocity and channel height. The solution was obtained on a 378 × 102 × 2 grid which is shown in Fig. 7.4. The simulation was conducted in OpenFOAM using the second order accurate PIMPLE algorithm. The results of computations are presented in Figs. 7.5-7.6.

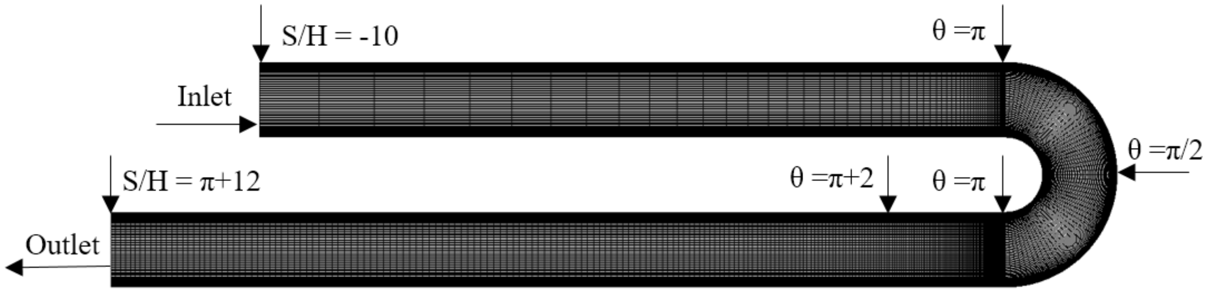

Figure 7.4 Structured mesh inside the U- duct shown in 2D.

Figure 7.5 shows the results of pressure coefficient C_p and skin friction coefficient C_f on the outer and inner wall of the duct respectively. Overall, the RANS models with RC did a better job in predicting the C_p and C_f curves than the DES model. On the inner wall, WA2017m-RC-DES model more accurately captures the profile for both C_p and C_f as shown in the Fig. 7.5 (b) and 7.5 (d). Even though there is no experimental data between θ ~ 0 and θ ~ π, WA2017m-RC-DES matches with the RSM results quite well. The separation occurs near $\theta = \pi$ on the inner wall; there is clear evidence that DES model is more reliable than RANS models if there is flow separation. On the outer wall, WA2017m-RC-DES is not able to predict minimum value of C_p and the maximum value of C_f, both values are underestimated by WA2017m-RC-DES model.

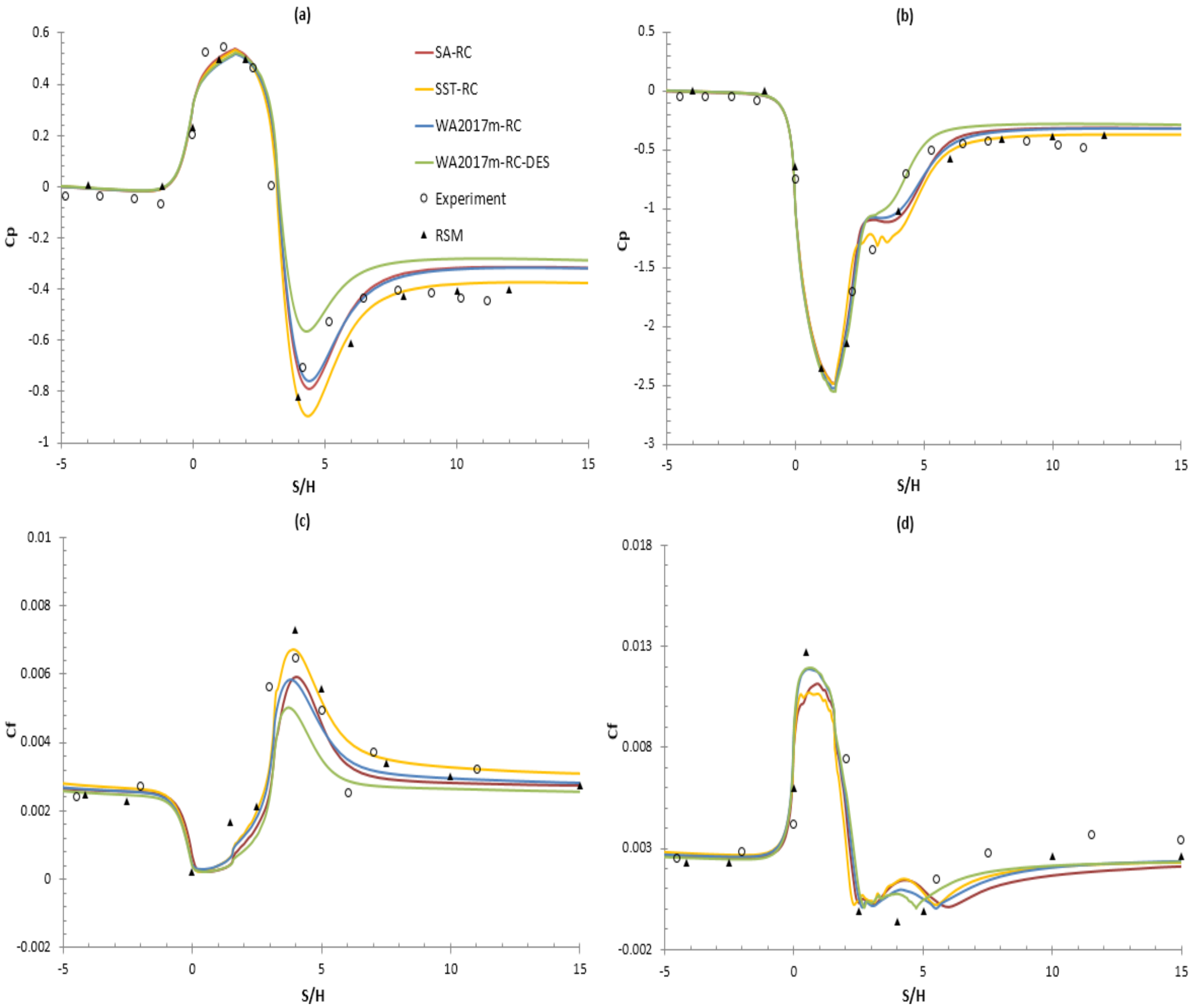

Figure 7.5 Results for (a) C_p along the outer wall, (b) C_p along the inner wall, (c) C_f along the outer wall and (d) C_f along the outer wall.

The velocity profiles are shown in Fig. 7.6. At sections θ = 0 and θ = π/2 of the U-duct, the results obtained from all the models have slight differences but overall are in reasonable agreement with the experimental data. After flow separation at θ = π section, the results deviate significantly from each other, and none of the models accurately determines the velocity profile. From the bottom right plot in Fig. 7.6, where the flow is at θ = π+2, it can be seen that all models overestimate the length of the recirculation region and predict a very slow recovery after reattachment. Although WA2017m-RC-DES model gives results closest to the experiment data, there is no significant improvement in velocity profiles by applying the DES model.

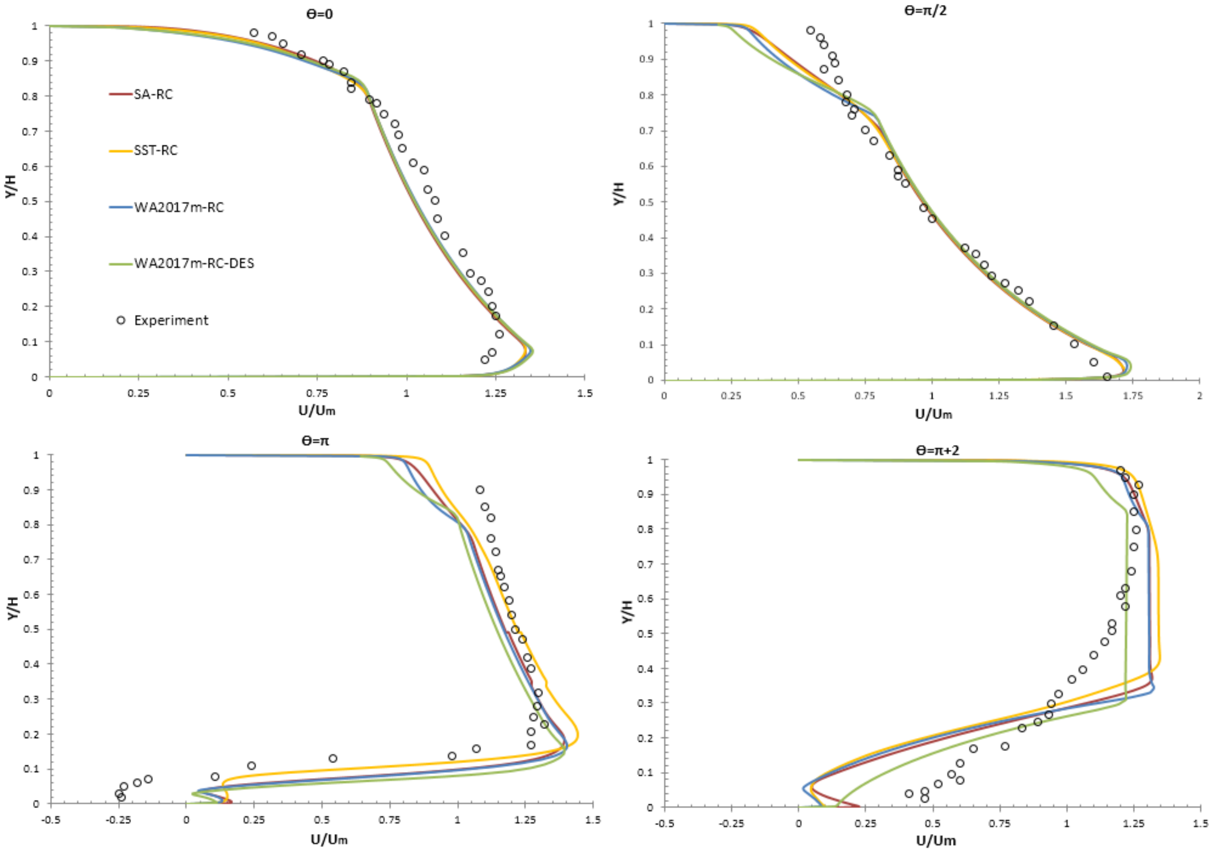

Figure 7.6 Velocity profiles at different sections of the U-duct.

7.3.3 Rotating Channel

In current study, SRFPimpleFoam solver in OpenFOAM is used to perform the simulation. The grid size for DES is 400 × 200 × 2 in *x*, *y* and *z* directions, which is sufficient to ensure a grid independent numerical solution. DES result is compared with RANS models SA-RC, WA2017m-RC and SST-RC as shown in Fig. 7.7. At low *Ro*, all the models except SST-RC almost predict the same profile, but at high *Ro* (e.g. $Ro = 0.5$) only WA2017m-RC-DES result best matches with the DNS data on both the suction side and pressure side of the channel compared to the other three RANS models.

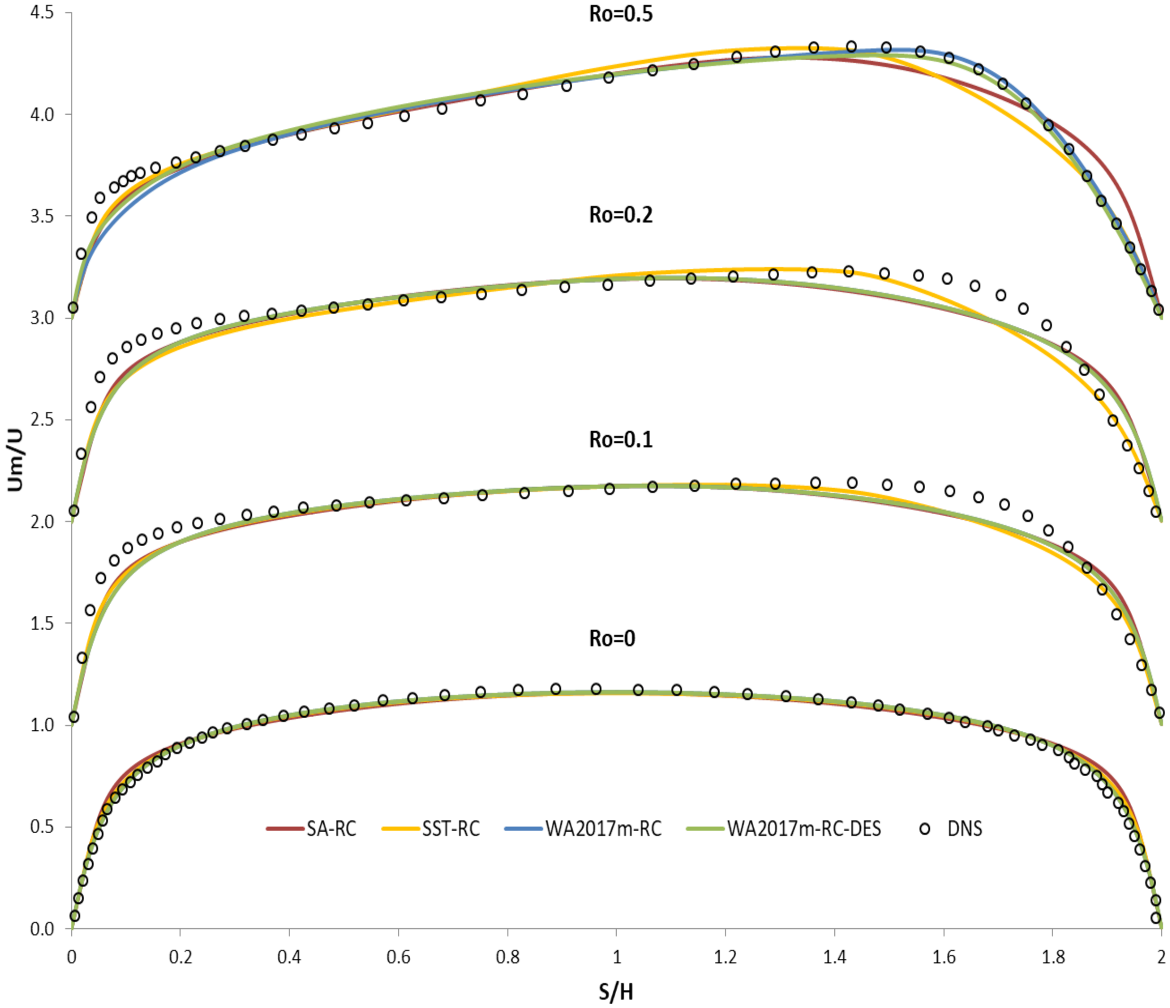

Figure 7.7 Velocity distribution in the rotating channel at different rotation numbers.

7.3.4 Rotating Backward-facing Step

Figure 7.8 shows the mean velocity profile at *x/h* = 0, 1, 2, 4, 7 and 24 for *Ro* = 0.05 and 0.2 from the computations using the SST-RC, WA2017m-RC and WA-2017m-RC-DES models. The SST-RC and WA2017m-RC models completely fail in computing the reattachment location and predict a very slow recovery. At low rotation number (*Ro* = 0.05), as shown in Fig. 7.8 (a), WA2017m-RC-DES successfully captures the flow separation on the bottom wall, and accurately calculates the velocity profile, which is not obtained with RANS models. Furthermore, in the recovery region at *x/h* = 7, WA2017m-RC-DES result is in reasonable agreement with the DNS data. At moderately high rotation number (*Ro* = 0.2) in Fig. 7.8 (b), DNS data shows a separation bubble on the upper wall, opposite to the step, which is due to the stabilizing effect of rotation on that wall. The turbulence is suppressed on this surface and hence the flow is susceptible to separation. The WA2017m-RC-DES model again successfully captures the separation at the right location on both sides of the walls and in the recovery region it matches the DNS data perfectly. At location *x/h* = 7, even though the velocity profile doesn't ideally match with the DNS data, the overall trend is close. In general, the WA2017m-RC-DES model not only accurately predicts the velocity profile but also the separation and reattachment points which the RANS models are unable to do.

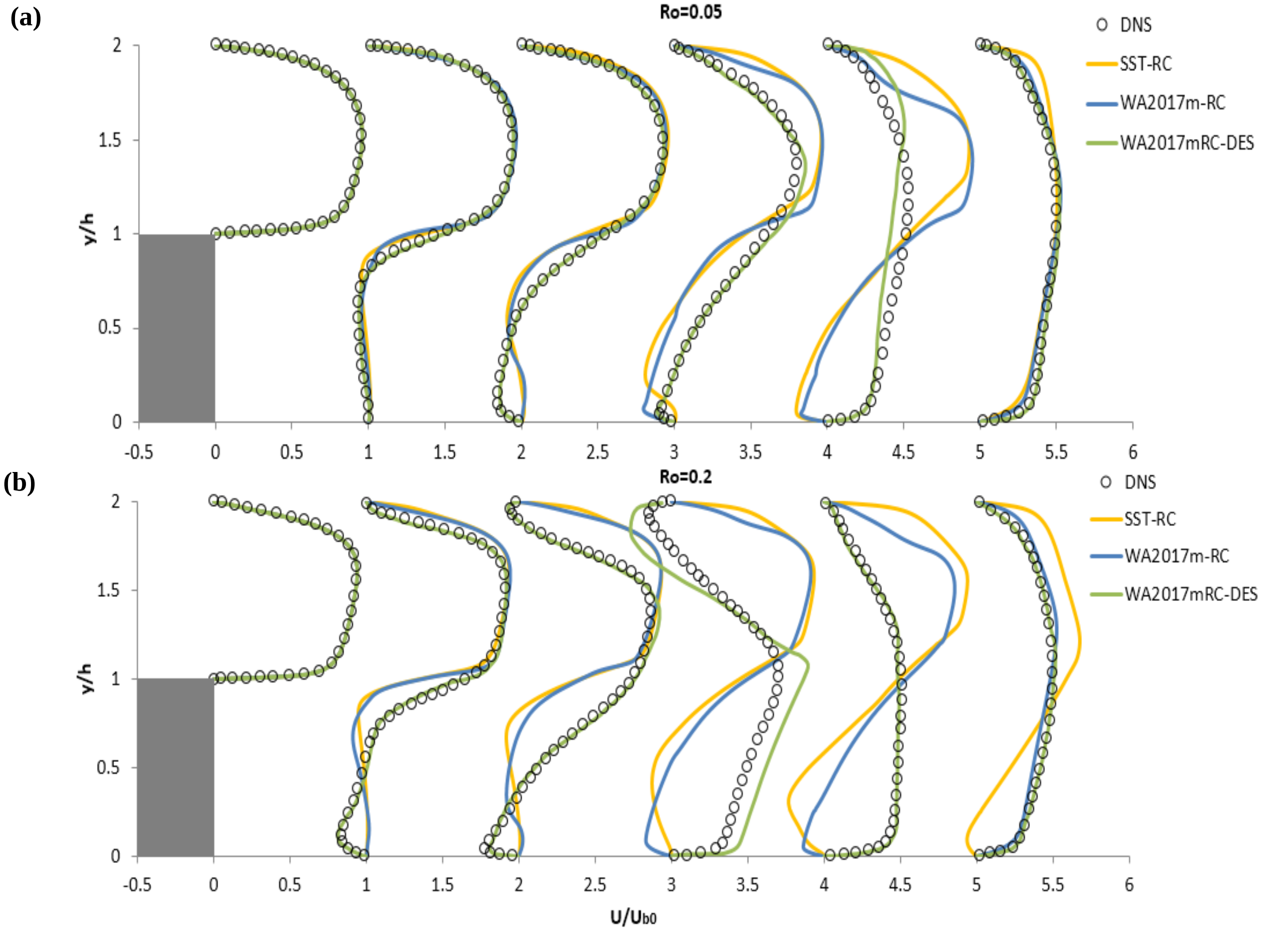

Figure 7.8 Comparison of mean velocity profile at (a) *Ro* = 0, (b) *Ro* = 0.05, and (c) *Ro* = 0.2 at multiple locations x/h = 0, 1, 2, 4, 7 and 24 on the backward facing step.

7.3.5 Stationary and Rotating Serpentine Channel

The grid size for DES is 1670 × 169 × 2 in *x*, *y* and *z* directions. Special refinement of the mesh is adopted after the U-turn part. In the stationary case, the qualitative trends are predicted well by all the models as shown in the Fig. 7.9. Except at the Station 2, 6 and Station 3, 7, SST-RC predicts a recirculation region near the outer wall, which is not seen in the DNS and other models. At the first two stations, WA2017m-RC almost duplicates the DNS results while WA2017m-RC-DES model performs slightly worse than WA2017m-RC model. However, at the latter stations, WA2017m-RC model can only predict the velocity profile trend while underestimates the peak value. WA2017m-RC-DES accurately calculates the peak value and the overall profile matches with the DNS data quite well. Especially at the station 4, 8 shown in Fig. 7.9 (d), WA2017m-RC-DES is the only model that is capable of predicting the reverse flow. The flow separation is a key feature of this case; therefore WA2017m-RC-DES model can be regarded as a significant improvement.

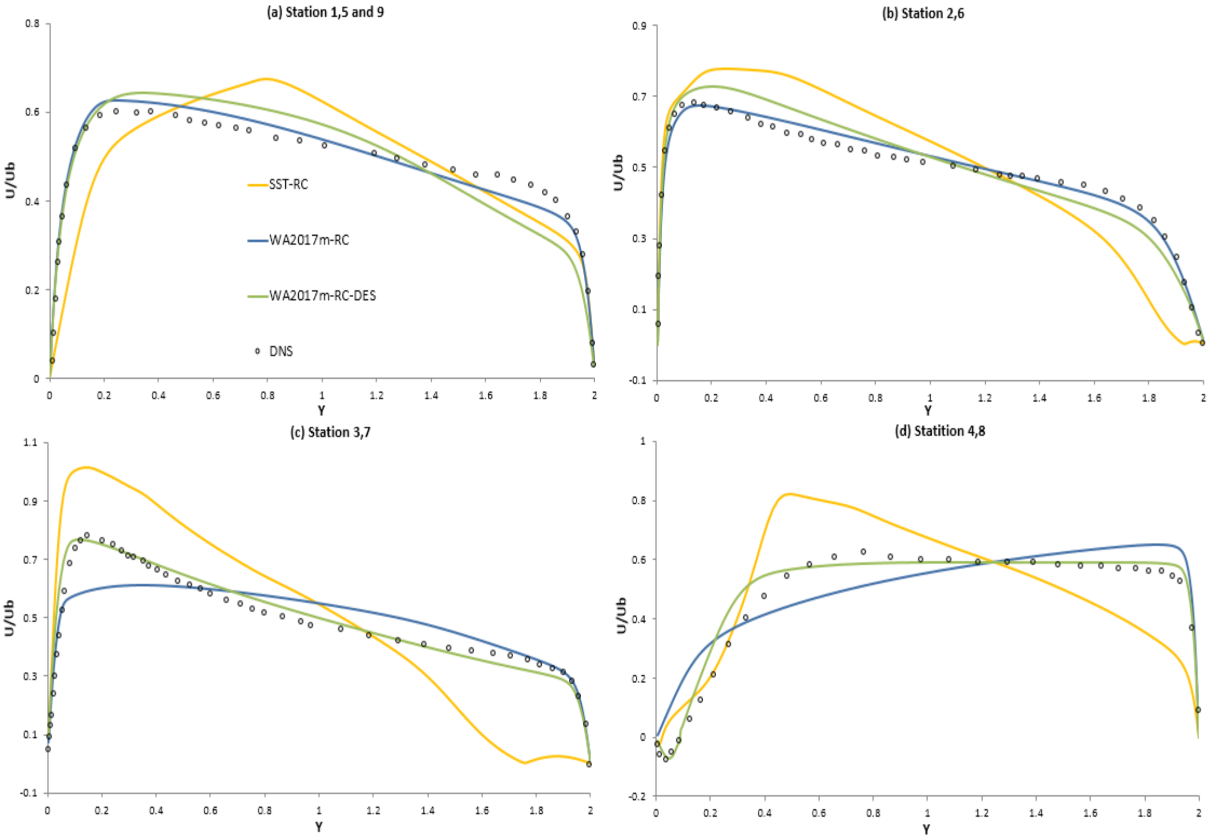

Figure 7.9 Mean velocity profile in stationary serpentine channel.

For the serpentine channel with span-wise rotation, the addition of orthogonal mode rotation results in a strong asymmetry between U-bend 1 and U-bend 2. At station 4, WA2017m-RC-DES model captures the flow separation but the separation bubble size is largely underestimated. The situation becomes better at station 8; the separation bubble size is accurately calculated as well as the overall velocity profile. Again, RANS models with RC correction are not capable of predicting the mean flow for the coupled curvature and rotation effect in a serpentine channel. Only a qualitative agreement is obtained by WA2017m-RC model. On the other hand, WA2017m-RC-DES exhibits a stronger ability to predict the mean flow field in better agreement with DNS data.

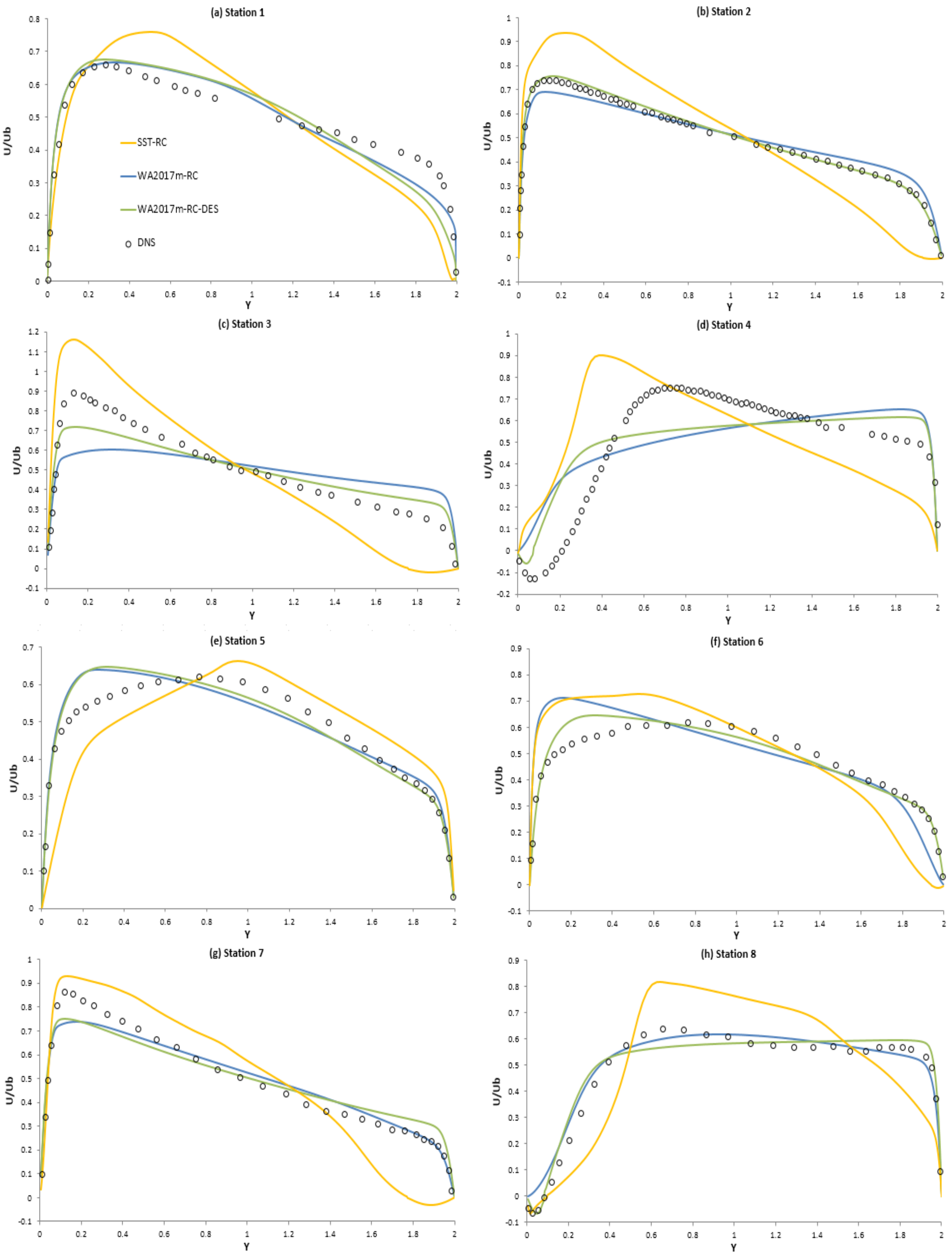

Figure 7.10 Mean velocity profiles in rotating serpentine channel at *Ro* = 0.32.

Chapter 8: Summary and Future Work

8.1 Summary

This thesis provides an introduction to the evolution of the one-equation eddy viscosity Wray-Agarwal turbulence model. It is developed from the first version designated WA2017 to WA2017m which is designed to overcome the problem of kink at the centerline of the velocity profile for flow in a planar channel and then to a wall distance free version WA2018. Finally WA2018EB version is developed by coupling an elliptic relaxation model with WA2018 model. The system rotation and streamline curvature are widely encountered in industrial applications. The effect of rotation and curvature are discussed respectively using two simple geometries. In flows with curvature, turbulent intensity is reduced along the convex curvature while it is enhanced along the concave curvature. In case of flows with rotation, turbulent intensity is increased on the unstable side while it is decreased on the stable side. The inability to account for system rotation and streamline curvature in k-ε turbulence model is discussed through the equilibrium analysis of the model. This deficiency is resolved by addition of the dependence of rotation in the turbulence model via two approaches, the “Modified Coefficients Approach” and the “Bifurcation Approach”. By applying the uncertainty quantification to WA2017m-RC model, the closure coefficients in RC correction were improved and the optimal closure coefficients were determined for WA2017m-RC model which are $c_{r1} = 1.0$, $c_{r2} = 0.5$ and $c_{r3} = 0.6$. From simulations of flow in the curved duct, U-turn duct and rotating channel, it was found that the rotation and curvature corrections to the turbulence models certainly improved the performance of the original SA, SST and WA2017m models. For other test cases which were more complex, models with RC and Arolla corrections provided better and more reasonable predictions than the original models. Overall, by analyzing the results for various test cases, WA2017m-RC model was found to be the best model among all the models, namely SA-RC, SST-RC, WA2017m-RC, WA2017m-RCM, WA2017m-Arolla, WA2018-RC and WA2018EB-RC.

A hybrid RANS/LES model based on WA2017m-RC RANS model was also developed which is designated as WA2017m-RC-DES. In DES approach, by analyzing the results of various test cases, namely the curved duct, U-duct, rotating channel, rotating backward-facing step and rotating serpentine channel, it was found that the RC correction enables the DES model to more accurately capture the effect of system rotation and streamline curvature compared to the RANS models with rotation and curvature corrections. Although DES results are dependent upon mesh size but by properly choosing a dense enough mesh, DES with RC correction can provide better accuracy compared to RANS models when compared to the DNS or experimental data. This thesis presents the DES calculations with RC correction in various turbulence models for the first time in the literature. Further research is needed to improve the DES models for flows with rotation and curvature. Nevertheless the test cases and results shown in this thesis can serve as a good starting point for future research.

8.2 Future Work

As mentioned in the summary section, WA2017m-Arolla model performs reasonably well overall. Therefore, it is worth investigating further by applying the Arolla correction to WA2018 and WA2018EB models.

To overcome the high grid-dependency of DES model, a new improved delayed detached eddy simulation (IDDES) model was developed by Gritskevich et al. [64]. In 2018, Han et al. [65]

developed the WA-IDDES model and showed good agreement with the experimental data for many test cases. It may be worthwhile to apply the rotation and curvature corrections to WA-IDDES model.

References

[1] LEAP CFD Team, “How Does the Reynolds Number Affect My CFD Model?” Mar 20, 2013, https://www.computationalfluiddynamics.com.au/reynolds-number-cfd/

[2] Spalart, P. R., “Detached-Eddy Simulation,” Annual Review of Fluid Mechanics, Vol. 41, 2009, pp. 181-202.

[3] Strelets, M., “Detached Eddy Simulation of Massively Separated Flows,” AIAA Paper 2001-0879, 39th Aerospace sciences meeting and exhibit, 2001.

[4] Spalart, P. R., and Allmaras, S. R., “A One Equation Turbulence Model for Aerodynamic Flows,” AIAA Paper 1992-0439, 1992.

[5] Menter, F. R., “Two-Equation Eddy-Viscosity Turbulence Models for Engineering Applications,” AIAA Journal, Vol. 32, No. 8, 1994, pp. 1598-1605.

[6] Han, X., Wray, T. J., and Agarwal, R. K., “Application of a New DES Model Based on Wray-Agarwal Turbulence Model for Simulation of Wall-Bounded Flows with Separation,” AIAA Paper 2017-3966, AIAA Aviation Forum, Denver, 5-9 June 2017.

[7] Menter, F. R., “Two-Equation Eddy-Viscosity Turbulence Models for Engineering Applications,” AIAA Journal, Vol. 32, No. 8, 1994, pp. 1598-1605.

[8] Zhang, X., and Agarwal, R. K., “Development of Various Rotation and Curvature Corrections for Eddy-Viscosity Turbulence Models,” AIAA Paper 2018-0591, AIAA SciTech Forum, Kissimmee, FL, 8-12 January 2018.

[9] Han, X., Rahman, M. and Agarwal, R. K., “Development and Application of Wall-Distance-Free Wray-Agarwal Turbulence Model (WA2018),” AIAA Paper 2018-0593, AIAA SciTech Forum, Kissimmee, FL, 8-12 January 2018.

[10] “NASA Langley Research Center Turbulence Modeling Resource,” http://turbmodels.larc.nasa.gov [retrieved October 2017]

[11] Durbin, P. A., Mansour, N. N., and Yang, Z., “Eddy Viscosity Transport Model for Turbulent Flow,” Physics of Fluids, Vol. 6(2), 1994, pp. 1007-1015.

[12] Rahman, M. M., Siikonen, T., and Agarwal R. K., “Improved Low Re-number One–Equation Turbulence Model,” AIAA Journal, Vol. 49, 2011, pp. 735-747.

[13] Rahman, M. M., Wallin, S., and Siikonen, T., “Exploring k and ω with R–Equation Model Using Elliptic Relaxation Function,” Flow, Turbulence and Combustion, Vol. 89, 2012, pp. 121–148.

[14] Elkhoury, M., “On the Eddy Viscosity Transport Models with Elliptic Relaxation,” Journal of Turbulence, Vol. 18(3), pp. 2017, pp. 240-259.

[15] Durbin, P. A., “Review: Adapting Scalar Turbulence Closure Models for Rotation and Curvature,” Journal of Fluids Engineering, Vol. 133, No. 6, 2011.
doi: 10.2514/3.13046

[16] Spalart, P. R., and Shur, M. L., “On the Sensitization of Turbulence Models to Rotation and Curvature,” Aerospace Science and Technology, Vol. 1, No. 5, 1997, pp. 297-302.

[17] Shur, M. L., “Turbulence Modeling in Rotating and Curved Channels: Assessing the Spalart-Shur Correction,” AIAA Journal, Vol. 38, No. 5, 2000, pp. 784-792.

[18] Reif, B. A. P., Durbin, P. A., and Ooi, A., “Modeling Rotational Effects in Eddy-Viscosity Closures,” International Journal of Heat and Fluid Flow, Vol. 20, No. 6, 1999, pp. 563-573.

[19] Arolla, S. K., “Modeling and Eddy Simulation of Rotating and Curved Turbulent Flows,” Ph.D. Dissertation, Aerospace Engineering, Iowa State Univ., Ames, IA, 2013.

[20] Chien, K. Y., “Predictions of Channel and Boundary-Layer Flows with a Low-Reynolds-Number Turbulence Model,” AIAA Journal, Vol. 20, No. 1, 1982, pp. 33-38.

[21] Launder, B. E., C. H. Priddin, and B. I. Sharma, “The Calculation of Turbulent Boundary Layers on Spinning and Curved Surfaces,” Journal of Fluids Engineering, Vol. 99, No. 1, 1977, pp. 231-239.

[22] Wallin, S. and Johansson, A. V., “Modelling Streamline Curvature Effects in Explicit Algebraic Reynolds Stress Turbulence Models,” International Journal of Heat and Fluid Flow, Vol. 23, No. 5, 2002, pp. 721-730.

[23] Durbin, P. A., “Some Recent Developments in Turbulence Closure Modeling,” Annual Review of Fluid Mechanics, Vol. 50, 2017, pp. 77-103.

[24] Speziale, C. G., “Analytical Methods for the Development of Reynolds-Stress Closures in Turbulence,” Annual review of fluid mechanics, Vol. 23, No. 1, 1991, pp. 07-157.

[25] Speziale, C. G., and MacGiolla Mhuiris, N., “On the Prediction of Equilibrium States in Homogeneous Turbulence,” J. Fluid Mech., Vol. 209, 1989, pp. 591–615.

[26] Speziale, C.G., Sarkar, S. and Gatski, T.B., “Modeling the Pressure-Strain Correlation of Turbulence: an Invariant Dynamical Systems Approach,” Journal of Fluid Mechanics, Vol. 227, 1991, pp. 245-272.

[27] Salhi, A., Cambon, C., and Speziale, C. G., “Linear Stability Analysis of Plane Quadratic Flows in a Rotating Frame with Applications to Modeling,” Physics of Fluids, Vol. 9. No.8, 1997, pp. 2300-2309.

[28] Hellsten, A., “Some Improvements in Menter’s k-ω SST Turbulence Model,” AIAA Paper 1998-2554, 1998.

[29] Zhang, Q., and Yang, Y., “A New Simpler Rotation/Curvature Correction Method for Spalart–Allmaras Turbulence Model,” Chinese Journal of Aeronautics, Vol. 26, 2013, pp. 326-333.

[30] Schaefer, J., Hosder, S., and West, T., “Uncertainty Quantification of Turbulence Model Closure Coefficients for Transonic Wall-Bounded Flows,” AIAA Journal, Vol. 55, No.1, 2016, pp. 195-213

[31] Stephanopoulos, K., Witte, I., and Wray, T. J., “Uncertainty Quantification of Turbulence Model Coefficients in OpenFOAM and Fluent for Mildly Separated Flows,” AIAA Paper 2016-4401, 46th AIAA Fluid Dynamics Conference, Washington, D.C., 2016.

[32] Smits, A. J., Young, S. T. B., and Bradshaw, P., “The Effect of Short Regions of High Surface Curvature on Turbulent Boundary Layers,” Journal of Fluid Mechanics, Vol. 94, Part 2, 1979, pp. 209-242.

[33] Rumsey, C., “2DCC: 2D Convex Curvature Boundary Layer Validation Case,” NASA Langley Research Center Turbulence Modeling Resource, URL: http://turbmodels.larc.nasa.gov [retrieved October 2015].

[34] Monson, D. J., Seegmiller, H. L., Mc Connaughey, P. K., and Chen, Y. S., “Comparison of Experiment with Calculations Using Curvature-Corrected Zero and Two Equation Turbulence Models for a Two-Dimensional U-Duct,” AIAA Paper 1990-1484, 1990.

[35] Fu, S., Rung, T., and Thiele, F., “Realizability of Non-Linear Stress-Strain Relationships for Reynolds-Stress Closures,” Proceedings of 11th Symposium on Turbulent Shear Flows, Vol.2, INPG, Grenoble, France, 1997, pp. 13.1-13.6

[36] Halleen, R. M., and Johnston, J. P., “The Influence of Rotation on Flow in a Long Rectangular Channel—An Experimental Study,” Dept. of Mechanical Engineering Rept. MD-18, Stanford Univ., Stanford, CA, May 1967.

[37] Johnston, J. P., Halleen, R. M., and Lezius, K., “Effects of Spanwise Rotation on the Structure of Two-Dimensional Fully Developed Turbulent Channel Flow,” Journal of Fluid Mechanics, Vol. 56, Part 3, Dec. 1972, pp. 533–557.

[38] Kristoffersen, R., and Anderson, H. I., “Direct Simulation of Low-Reynolds-Number Turbulent Flow in a Rotating Channel,” Journal of Fluid Mechanics, Vol. 256, November 1993, pp.163-197.

[39] Lamballais, E., Lesieur, M., and Metais, O., “Effects of Spanwise Rotation on the Stretching in Transitional and Turbulent Channel Flow,” International Journal Heat and Fluid Flow, Vol. 17, No. 3, 1996, pp. 324–332.

[40] Barri, M., and Andersson, H. I., "Turbulent Flow over a Backward-Facing Step. Part 1. Effects of Anti-Cyclonic System Rotation," Journal of Fluid Mechanics, Vol. 665, 2010, pp. 382-417.

[41] Breiter, M. C., and Pohlhausen, K., “Laminar Flow between Two Parallel Rotating Disks,” Technical Report No. 275562, ARL, USAF, 1962.

[42] Owen, J. M., and Pincombe, J. R., “Velocity Measurements Inside a Rotating Cylindrical Cavity with a Radial Outflow of Fluid,” Journal of Fluid Mechanics, Vol. 99, No. 1, 1980, pp. 111–127.

[43] Poncet, S., Soghe, R. D., and Facchini, B., “RANS Modeling of Flow in Rotating Cavity System,” V European Conference on Computational Fluid Dynamics (ECCOMAS CFD 2010), Lisbonne, Portugal, Jun 2010.

[44] Del Arco, E. C., Maubert, P., and Randriamampianina, A., “Spatio-Temporal Behaviour in a Rotating Annulus with a Source-Sink Flow,” Journal of Fluid Mechanics, Vol. 328, 1996, pp. 271–296.

[45] Iaccarino G., Ooi, A., and Reif B. A. P., “RANS Simulations of Rotating Flows,” Annual Research Briefs, Center for Turbulence Research, Stanford, CA, 1999.

[46] Laskowski G. M., and Durbin P. A., “Direct Numerical Simulations of Turbulent Flow Through a Stationary and Rotating Infinite Serpentine Passage,” Physics of Fluids, Vol. 19, No. 1, 2007.

[47] Daily, J. W., and Nece, R. E., “Chamber Dimension Effects on Induced Flow and Frictional Resistance of Enclosed Rotating Disks,” ASME Journal of Basic Engineering. Vol. 82, No. 1, 1960, pp. 217-230.

[48] Owen, J. M., and Rogers, R. H., “Flow and Heat Transfer in Rotating- Disc Systems. Volume I - Rotor-Stator Systems,” NASA STI/Recon Technical Report A 90, 1989.

[49] Itoh, M., Yamada, Y., Imao, S., and Gonda, M., “Experiments on Turbulent Flow Due to an Enclosed Rotating Disk,” Experimental Thermal and Fluid Science, Vol. 5, No. 3. 1992, pp. 359-368.

[50] Poncet, S., Schiestel, R. and Chauve, M. P., “Centrifugal Flow in a Rotor-Stator Cavity,” Journal of Fluids Engineering, Vol. 127, No. 4, 2005, pp. 787-794.

[51] Schiestel, R. and Elena, L., “Modeling of Anisotropic Turbulence in Rapid Rotation,” Aerospace Science and Technology, Vol. 7, 1997, pp. 441–451.

[52] Poncet, S., Chauve, M. P., and Schiestel, R., “Batchelor versus Stewartson Flow Structures in a Rotor-Stator Cavity with Throughflow,” Physics of Fluids, Vol. 17, No. 7, 2005.

[53] Stairmand, C. J., “The Design and Performance of Cyclone Separators,” Transactions of the Institution of Chemical Engineers, Vol. 29, 1951, pp. 356-383.

[54] Boysan, F., Ewan, B. C. R., and Swithenbank, J., “Experimental and Theoretical Studies of Cyclone Separator Aerodynamics,” IChemeE Symposium Series, Vol. 69, 1983, pp. 305-320.

[55] Muppidi, S. and Mahesh, K., “Direct Numerical Simulation of Round Turbulent Jets in Crossflow,” Journal of Fluid Mechanics, Vol. 574, 2007, pp. 59-84.

[56] Su, L. K. and Mungal, M. G., "Simultaneous Measurements of Scalar and Velocity Field Evolution in Turbulent Crossflowing Jets," Journal of Fluid Mechanics, Vol. 513, 2004, pp. 1-45.

[57] Wernet, M., Wolter, J., Locke, R., Wroblewski, A., Childs, R., and Nelson, A., "PIV Measurements of the CEV Hot Abort Motor Plume for CFD Validation," AIAA Paper 2010-1031, 48th AIAA Aerospace Sciences Meeting Including the New Horizons Forum and Aerospace Exposition, January 2010, pp. 1031.

[58] Abdol-Hamid, K. S., Massey, S. J., and Elmiligui, A., "Temperature Corrected Turbulence Model for High Temperature Flow," Journal of Fluids Engineering, Vol. 126, 2004, pp. 844.

[59] Seiner, J. M., Ponton, M. K., Jansen, B. J., and Lagen, N. T., 1992, "The Effects of Temperature on Supersonic Jet Noise Emission," DGLR/AIAA 14th Aeroacoustics Conference, Aachen, Germany, AIAA Paper No. 92-02-046, May 1992.

[60] Thomas, R. H., Kinzie, K. W., and Pao, S. Paul, 2001, "Computational Analysis of a Pylon-Chevron Core Nozzle Interaction," AIAA Paper 2001-2185, May 2001.

[61] Spalart, P. R., "Comments on the Feasibility of LES for Wings and on the Hybrid RANS/LES Approach," Advances in DNS/LES, 1st AFOSR Int. Conf. on DNS/LES, 1997.

[62] Han, X., Wray, T. J., and Agarwal, R. K., "Application of a New DES Model Based on Wray-Agarwal Turbulence Model for Simulation of Wall-Bounded Flows with Separation," AIAA Paper 2017-3966, AIAA Aviation Forum, Denver, 5-9 June 2017.

[63] Spalart, P. R., Deck, S., Shur, M. L., Squires K. D., Strelets, M. K. and Travin, A., "A New Version of Detached-Eddy Simulation, Resistant to Ambiguous Grid Densities," Theor. Comput. Fluid Dyn., Vol. 20, 2006, pp. 181-195.

[64] Gritskevich, M. S., Garbaruk, A. V., Schütze, J. and Menter, F. R., "Development of DDES and IDDES Formulations for the k-ω Shear Stress Transport Model," Flow, Turbulence and Combustion, Vol. 88, No, 3, 2012, pp. 431-449.

[65] Han, X., and Agarwal, R. K., "Application of a New IDDES Model Based on Wray-Agarwal Turbulence Model for Simulation of Wall-Bounded Flows with Separation," AIAA Paper 2018-1086, 2018 AIAA Aerospace Sciences Meeting, 2018, pp. 1086.

Vita

Xiao Zhang

Degrees	Ph.D. in Mechanical Engineering, Washington University in St. Louis, August 2018
	M.S. in Mechanical Engineering, Washington University in St. Louis, August 2015
	B.S. in Thermal and Power Engineering, Chongqing University, June 2013
Publications	Zhang, X., and Agarwal, R. K., “Development of Various Rotation and Curvature Corrections for Eddy-Viscosity Turbulence Models,” AIAA Paper 2018-0591, AIAA SciTech Forum, Kissimmee, FL, 8-12 January 2018.
	Zhang, X., Wray, T. and Agarwal, R. K., “Application of a New Simple Rotation and Curvature Correction to the Wray-Agarwal Turbulence Model,” 46th AIAA Fluid Dynamics Conference, 2016, pp. 3475.
	Zhang, X., “Process simulation and maximization of energy output in chemical-looping combustion using ASPEN plus,” International Journal of Energy and Environment, Vol. 6, No. 2, 2015, pp. 201.
	Zhang, X., “Validation of chemical-looping with oxygen uncoupling (CLOU) using Cu-based oxygen carrier and comparative study of Cu, Mn and Co based oxygen carriers using ASPEN plus,” International Journal of Energy and Environment, Vol. 6, No. 3, 2015, pp. 247-254.

August 2018